Mon. Not. R. Astron. Soc. **342,** 759–801 (2003)

Breaking the 'redshift deadlock' – II. The redshift distribution for the submillimetre population of galaxies

Itziar Aretxaga,[1⋆] David H. Hughes,[1] Edward L. Chapin,[1] Enrique Gaztañaga,[1,2] James S. Dunlop[3] and Rob J. Ivison[4]

[1] *Instituto Nacional de Astrofísica, Óptica y Electrónica (INAOE), Aptdo. Postal 51 y 216, 72000 Puebla, Mexico*
[2] *IEEC/CSIC, Edifici Nexus-201, c/ Gran Capitán 2-4, 08034 Barcelona, Spain*
[3] *Institute for Astronomy, University of Edinburgh, Blackford Hill, Edinburgh EH9 3HJ*
[4] *Astronomy Technology Centre, Royal Observatory, Blackford Hill, Edinburgh EH9 3HJ*

Accepted 2003 February 19. Received 2003 February 19; in original form 2002 April 30

ABSTRACT

Ground-based submillimetre and millimetre wavelength blank-field surveys have identified more than 100 sources, the majority of which are believed to be dusty optically obscured starburst galaxies. Colours derived from various combinations of far-infrared, submillimetre, millimetre and radio fluxes provide the only currently available means to determine the redshift distribution of this new galaxy population.

In this paper we apply our Monte Carlo photometric redshift technique, introduced recently by Hughes et al. in Paper I, to the multiwavelength data available for 77 galaxies selected at 850 μm and 1.25 mm. We calculate a probability distribution for the redshift of each galaxy, which includes a detailed treatment of the observational errors and uncertainties in the evolutionary model. The cumulative redshift distribution of the submillimetre galaxy population that we present in this paper, based on 50 galaxies found in wide-area SCUBA surveys, is asymmetric, and broader than those published elsewhere, with a significant high-z tail for some of the evolutionary models considered. Approximately 40 to 90 per cent of the submillimetre population is expected to have redshifts in the interval $2 \leqslant z \leqslant 4$. Whilst this result is completely consistent with earlier estimates for the submillimetre galaxy population, we also show that the colours of many ($\lesssim$50 per cent) individual submillimetre sources, detected only at 850 μm with non-detections at other wavelengths, are consistent with those of starburst galaxies that lie at extreme redshifts, $z > 4$. Spectroscopic confirmation of the redshifts, through the detection of rest-frame far-infrared–millimetre wavelength molecular transition lines, will ultimately calibrate the accuracy of this technique. We use the redshift probability distribution of HDF850.1 to illustrate the ability of the method to guide the choice of possible frequency tunings on the broad-band spectroscopic receivers that equip the large-aperture single-dish millimetre and centimetre wavelength telescopes.

Key words: stars: formation – galaxies: evolution – cosmology: miscellaneous – infrared: galaxies – submillimetre.

1 INTRODUCTION

The lack of robust redshift information is one of the outstanding problems in understanding the nature of the presumed high-redshift galaxies identified in blank-field submillimetre (sub-mm) and millimetre wavelength surveys.

In Paper I of this series (Hughes et al. 2002) we described Monte Carlo simulations of 250–500 μm surveys from the Balloon-borne Large Aperture Submillimetre Telescope (BLAST) (Devlin et al. 2001) and the SPIRE instrument on the *Herschel* satellite, as well as longer-wavelength ground-based 850-μm surveys with SCUBA. These simulations included a detailed treatment of the observational and evolutionary model-dependent errors. The sub-mm colours of galaxies derived from these mock surveys demonstrated that it will be possible to derive photometric redshifts, with a conservative rms accuracy of $\Delta z \sim \pm 0.5$, for thousands of optically obscured galaxies. Thus we can look forward to breaking the redshift deadlock, which, at the moment, prevents a reliable estimate of the

⋆E-mail: itziar@inaoep.mx

evolutionary history of a population that contributes a significant fraction ($\gtrsim$50 per cent for $S_{850\,\mu m} > 2$ mJy) to the sub-mm background (Hughes et al. 1998; Smail et al. 2002).

In this second paper we apply the same Monte Carlo photometric redshift technique to the existing far-infrared (FIR)–radio multiwavelength data for 77 sources first identified in blank-field 850-μm (SCUBA) and 1.2-mm (MAMBO) surveys. We calculate the redshift probability distributions of the individual sub-mm and mm galaxies, taking into account observational and model-dependent uncertainties, and thus provide a measurement of the cumulative redshift distribution for the blank-field sub-mm galaxy population. This redshift distribution is completely insensitive to ambiguities in the identification of the optical counterparts.

The structure of this paper is as follows: Section 2 gives a brief description of the Monte Carlo simulations, the method to derive photometric redshifts from the radio–sub-mm–FIR colours of galaxies drawn from the mock catalogues, and the caveats and advantages of this technique over other redshift indicators. Section 3 presents individual redshift probability distributions for blank-field sub-mm galaxies. In addition, we include a brief discussion of the photometric redshifts for radio- and FIR-selected galaxies subsequently detected at 850 μm. Furthermore, we determine the accuracy of our method through the comparison of the photometric redshifts for those eight sub-mm sources that have published rest-frame optical spectroscopic redshifts. Finally in Section 3 we present the cumulative redshift distribution of the blank-field sub-mm population. Section 4 discusses the likelihood of a radio detection of previously detected blank-field sub-mm sources, based only on the known dispersion of the 850-μm/1.4-GHz colour in starburst galaxies, radio-quiet active galactic nuclei (AGN) and ultraluminous infrared galaxies (ULIRGs), which are believed to be representative of the high-z sub-mm galaxy population. Section 5 describes how the determination of redshift probability distributions for individual sub-mm galaxies is motivating the efforts to provide spectroscopic confirmation of the redshifts at millimetre and centimetre wavelengths. Ultimately, these spectroscopic redshifts will accurately calibrate the photometric redshifts derived from rest-frame FIR–radio wavelength data. Appendix A contains the complete catalogue of spectral energy distributions (SEDs) and redshift distributions derived in this paper.

2 PHOTOMETRIC REDSHIFT ESTIMATION TECHNIQUE

The Monte Carlo simulations described in this paper produce the redshift probability distribution for an individual galaxy. The advantage of this technique, compared to the popular maximum-likelihood methods, is that it provides more information than a simple estimate of the first and second moments of the redshift distributions. A detailed description of the technique can be found in Paper I; we only offer a summary here. Hereafter we will refer to a galaxy detected in a SCUBA or MAMBO survey as a *sub-mm* galaxy, and a sub-mm galaxy generated in the Monte Carlo simulations as a *mock* galaxy.

We choose an evolutionary model for the 60-μm luminosity function that fits the observed 850-μm number counts. Under this model, and assuming a sub-mm survey of $\sim$10 deg^2, we generate a catalogue of 60-μm luminosities and redshifts. Randomly selected template SEDs are drawn from a library of local starbursts, ULIRGs and AGN, to provide FIR–radio fluxes, and hence colours, for this mock catalogue. The fluxes of the mock galaxies include both photometric and calibration errors, consistent with the quality of the observational data for the sub-mm galaxy detected in a particular survey. We reject from the catalogue those mock galaxies that do not respect the detection thresholds and upper limits of the particular sub-mm galaxy under analysis. In this paper the redshift probability distribution of a sub-mm galaxy is calculated as the normalized distribution of the redshifts of the mock galaxies in the reduced catalogue, weighted by the likelihood of identifying the colours and fluxes of each mock galaxy with those of the sub-mm galaxy in question. Thus, we also take into account as much prior information on the sub-mm galaxy population (and their uncertainties) as possible. For example, we consider uncertainties in the sub-mm galaxy number counts, their favoured evolutionary models, the luminosity function of dusty galaxies, lensing by a foreground magnifying cluster, etc. In the case that the sub-mm galaxy is identified as a lensed source, then the mock catalogue is also amplified by the appropriate factor, allowing intrinsically fainter objects to be introduced into the reduced catalogue, using the same observational measurement errors.

We adopt a flat, Λ-dominated cosmological model ($H_0 = 67$ km s^{-1} Mpc^{-1}, $\Omega_M = 0.3$, $\Omega_\Lambda = 0.7$). To quantify the sensitivity of the individual redshift distributions on the assumed evolutionary history of the sub-mm galaxy population, we consider six different models that are able to reproduce the observed 850-μm number counts within the uncertainties. We will refer to them by the following codes:

le1: Luminosity evolution of the 60-μm luminosity function $\Phi[L, z = 0]$ (Saunders et al. 1990) as $(1 + z)^{3.2}$ for $0 < z < 2.2$. Constant evolution is imposed between $z = 2.2$ and 10. No galaxies beyond $z = 10$, $\Phi[L, z > 10] = 0$.

le1L13: Same evolutionary description as in le1, but imposing a luminosity cut-off above 10^{13} L$_\odot$.

le2: Luminosity evolution of $\Phi[L, 0]$ as $(1 + z)^3$ for $0 < z < 2.3$. Constant evolution is imposed between $z = 2.3$ and 6. $\Phi[L, z > 6] = 0$.

le2L13: Same evolutionary description as in le2, but imposing a luminosity cut-off above 10^{13} L$_\odot$.

lde1: Luminosity evolution of $\Phi[L, 0]$ as $(1 + z)^{1.9}$ and density evolution as $(1 + z)^{2.5}$ for $0 < z < 3.5$. Luminosity and density evolution as $(1 + z)^{-3.0}$ for $3.5 \leqslant z \leqslant 7$.

lde2: Luminosity evolution of $\Phi[L, 0]$ as $(1 + z)^{3.5}$ and density evolution as $(1 + z)^3$ for $0 < z < 2.0$. No further luminosity evolution, and density evolution as $(1 + z)^{-2}$ for $2 \leqslant z \leqslant 6$.

The models used in this analysis provide a wide range of the many possible evolutionary scenarios that reproduce the sub-mm to mm number counts. These models will allow us to test the robustness of the photometric redshifts that we will derive in the next section.

An extended library of SEDs (compared to Paper I) is used in the Monte Carlo simulations. The library contains 20 starbursts, ULIRGs and AGN that either have been extensively mapped at FIR–radio wavelengths, or are sufficiently distant that single-beam photometric observations measure the total flux: M82, NGC 3227, NGC 2992, NGC 4151, NGC 7469, NGC 7771, NGC 1614, I Zw 1, Mrk 231, Arp 220, Mrk 273, NGC 6240, UGC 5101, IRAS 10214+4724, IRAS 05189−2524, IRAS 08572+3915, IRAS 15250+3609, IRAS 12112+0305, IRAS 14348−1447 and Cloverleaf. This selection has the important consequence of reducing any dispersion in the SEDs due to aperture effects. A continuum SED that includes synchrotron and free–free emission in the radio–mm regime, and thermal emission from dust grains in the mm–FIR regime, is fitted to the observational data (Chapin et al., in preparation). The luminosities and temperatures of the dust that dominates the rest-frame FIR emission

are evenly distributed in the ranges $9.0 \lesssim \log L_{\rm FIR}/{\rm L}_{\odot} \lesssim 12.3$ and $25 < T/{\rm K} < 65$.

Half of the galaxies in the SED library used in the derivation of photometric redshifts in this paper are in common with those considered by Yun & Carilli (2002, hereafter YC02). The temperature range covered by our sample of galaxies (25–65 K, median 41 K) is broader than that of YC02 due to the increased fraction of cooler sources, and is, for the same reason, colder than those of well-studied ULIRGs (46–77 K, median 60 K, Klaas et al. 2001). Despite the similar temperatures of our sample to late-type galaxies selected at 60 μm (25–55 K, median 35 K), drawn from the SLUGS catalogue of Dunne et al. (2000), the shapes of the SEDs in our library differ significantly from those of the local galaxies in the SLUGS. This illustrates an important point: it is the shapes of the SEDs, and not the derived dust temperatures, that influence the estimated photometric redshifts. Given the limited FIR–sub-mm data, there is a degeneracy between the dust temperatures, grain emissivity index (β), source size (Ω) and optical depth (τ_{ν}). This makes it possible to fit a single observed SED with a broad range of temperature, by tuning the choice of β, Ω and τ_{ν} (e.g. Hughes et al. 1993).

It remains unclear whether the lower-luminosity, local galaxies in the SLUGS are closely related to the blank-field SCUBA population, which have rest-frame FIR luminosities $>10^{12}$ $L_{\odot}$, assuming the sub-mm galaxies lie at $z > 1$. The claim that cold SEDs match the number counts in hydrodynamical cosmological simulations (e.g. Fardal et al. 2002) should not be a basis for favouring cold SEDs, since a different evolutionary model with warmer SEDs can fit the counts equally well.

The strongest caveat in any photometric redshift analysis is the validity of the assumption that the SED templates of local starbursts, ULIRGs and AGN are good analogues of the high-redshift sub-mm galaxy population. It is not until future rest-frame FIR–sub-mm observations from sensitive balloon-borne or satellite experiments (Paper I) accurately measure the variety of SEDs present in the sub-mm galaxy population, and spectroscopic redshifts for these are available, that it will be possible to improve the error estimates presented in this paper.

The technique adopted in this paper differs philosophically from those developed in other photometric redshift studies. Our redshift estimates do not rely on the match of the observed data to a single template SED, and our errors are not drawn from the departure of other local SEDs from the adopted standard template, which has become the common practice (Carilli & Yun 1999, 2000, hereafter CY99, CY00; Gear et al. 2000; YC02). Instead, we allow the test galaxies to be matched against the whole variety of template SEDs that can be detected at any given redshift. This point should be emphasized, since, although we assign our template SEDs at random, not all SED shapes (scaled to the same FIR luminosity) are detected with equal probability at any given redshift and wavelength. The redshift distributions derived in this paper are often asymmetric, and broader than those inferred from the single SED template analysis. Despite the efforts of some authors to include realistic error bars in their single-template estimates, we consider these to have been underestimated: an error bar derived from 68 per cent of the galaxies in a template catalogue is not equivalent to the 68 per cent dispersion in the fluxes that the whole catalogue can create, since some of the outliers contribute very significantly to the departures from the mean.

Our redshift estimation method also has the advantage of including a common-sense evaluation of whether a source at a given redshift is simultaneously consistent with the observed colours and fluxes. The probability of generating a certain luminosity at a certain redshift (i.e. flux) is introduced by the luminosity function and the evolutionary model adopted. As shown below, when sub-mm galaxies with detections at more than two wavelengths are considered, the results are quite insensitive to the differences in the evolutionary models adopted to generate the mock catalogue. The consideration of reasonable evolutionary models, however, allow plausible colour-based redshift solutions to be excluded.

3 MONTE CARLO BASED PHOTOMETRIC REDSHIFTS

The available data set for the sub-mm population of galaxies is usually restricted to a low signal-to-noise ratio (S/N) detection at 850 μm and an upper limit at 450 μm (from SCUBA surveys), or a 1.2-mm detection (from MAMBO surveys or an IRAM PdB follow-up observation), with, perhaps, radio observations at 1.4, 5 or 8.6 GHz. Although a number of the SCUBA surveys have been conducted in fields previously observed by the *Infrared Space Observatory* (*ISO*) with the ISOPHOT camera at 170 and 90 μm, e.g. HDF (Hughes et al. 1998; Borys et al. 2002), ELAIS N2 and the Lockman Hole (Scott et al. 2002; Fox et al. 2002), the *ISO* measurements are generally too insensitive to provide any additional constraint on the photometric redshifts.

The method described in Section 2 produces mock catalogues that replicate the sensitivities and calibration accuracies of the original surveys in which each sub-mm galaxy was detected. The colours and fluxes of the mock galaxies provide diagnostic diagrams to illustrate the derivation of the most probable redshift: colour–colour–redshift (C–C–z) diagrams, when more than three-band detections are available; colour–flux–redshift (C–f–z) diagrams, when just two bands are available; and flux–redshift (f–z) diagrams, when just one band detection is available. From these diagrams we derive the corresponding redshift probability distribution (P–z) for each sub-mm galaxy. The distributions for a selection of sub-mm galaxies considered in this paper are shown in Appendix A.

3.1 Specific examples: LH850.1 and BCR11

LH850.1 is the brightest 850-μm source identified in the wide-area UK 8-mJy SCUBA survey of the Lockman Hole (Scott et al. 2002), and has one of the most complete FIR–radio SEDs (Lutz et al. 2001). BCR11, named after source 11 in the sub-mm catalogue of Barger, Cowie & Richards (2000), is a low S/N, but none the less representative, 850-μm source detected in a follow-up SCUBA photometry survey of the micro-Jansky 1.4-GHz radio sources in the *Hubble Deep Field* (Richards 2000).

Even though BCR11 was not first identified in a blank-field sub-mm survey, and hence is not included in the combined redshift distribution of the sub-mm selected galaxy population, it provides a useful source to discuss. The sub-mm photometry observations of BCR11 at the position of a known radio source (Richards 2000) guarantees that we have the correct association of a radio and sub-mm source, and hence the correct SED to analyse. BCR11 allows us to confidently derive the photometric redshift and accuracy that we can expect from only the 850 μm/1.4 GHz colour, which is commonly used to measure redshifts of blank-field sub-mm galaxies with follow-up radio observations (CY99, CY00).

Figs 1, 2 and 3, respectively, show the C–C–z and P–z distributions for the multiwavelength data of LH850.1, and the comparison of the observed SED and template SEDs (redshifted to the mode of

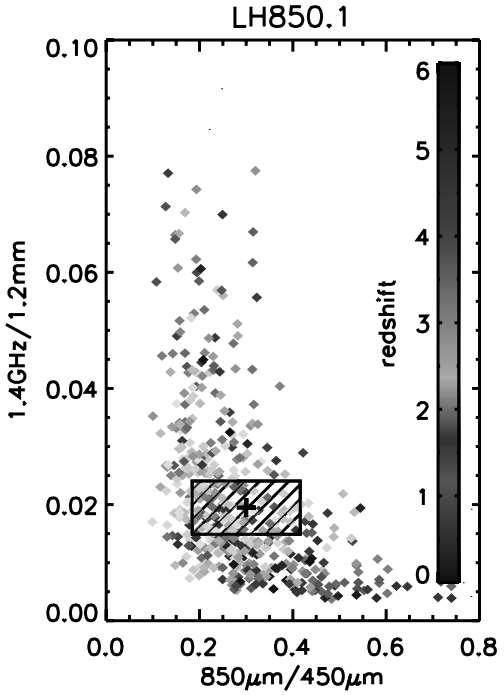

Figure 1. Colour–colour–redshift (*C*–*C*–*z*) plot for LH850.1 (Lutz et al. 2001; Scott et al. 2002). The flux ratios of the mock galaxies, generated under the evolutionary model le2 (Section 2), are represented as diamonds, and their redshifts are coded in colour according to the scale shown to the right of the panel (colours can be seen in the electronic version of the paper). The cross represents the measured colours of LH850.1, and the dashed box shows the 1σ uncertainty in each colour. This figure is available in colour in the online version of the journal on *Synergy*.

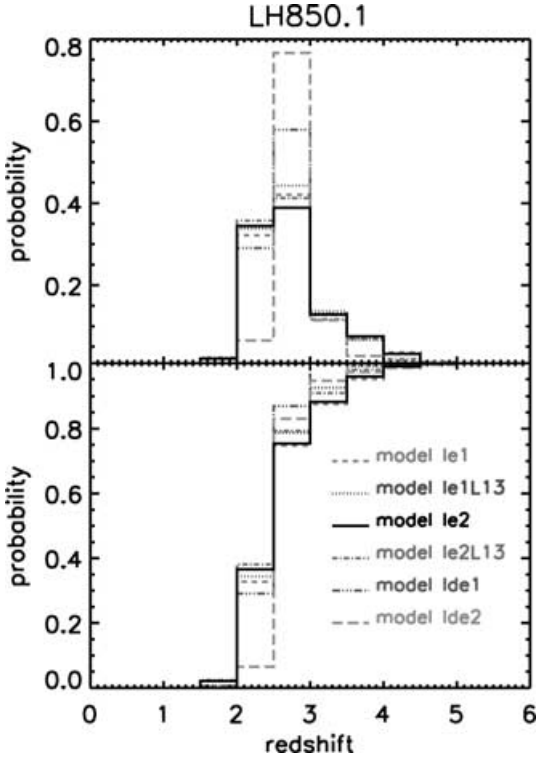

Figure 2. Discrete and cumulative redshift probability distributions of LH850.1. The six estimates, plotted with lines of different style, correspond to the six evolutionary models introduced in Section 2. This figure is available in colour in the online version of the journal on *Synergy*.

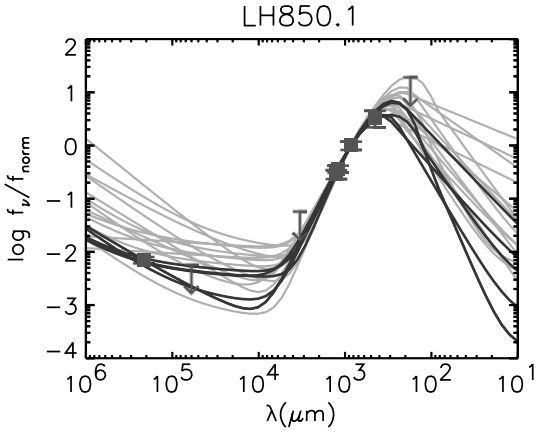

Figure 3. The observed SED of LH850.1 normalized to the flux density at 850 μm is shown as squares and arrows. The arrows indicate 3σ upper limits. The squares denote detection at a level $\geqslant 3\sigma$, with 1σ error bars. The template SEDs (lines) are redshifted to $z = 2.6$, the mode of the redshift probability distribution of most models considered (see Table 1). The template SEDs *at this redshift* compatible within 3σ error bars with the SED of LH850.1 are displayed as darker lines (blue in the electronic version). This figure is available in colour in the online version of the journal on *Synergy*.

the *P*–*z* distribution). Figs 4, 5 and 6 show the same distributions for BCR11. In both examples (Figs 2 and 5) the peak of the redshift probability distribution depends little on the details of the evolutionary model used to compute the mock catalogues. In both cases, the models that invoke pure luminosity evolution (le1, le1L13, le2, le2L13) have more extended wings, since they provide a significant population of sources at redshifts beyond 3 that can reproduce the colours of the observed galaxies. On the other hand, the combined luminosity and density evolution models (led1, led2) have a very strong decline in the density of sources at redshifts beyond 2 and 3.5, and thus the corresponding redshift distributions are much more concentrated to values between 2 and 3. Model led1 is the most extreme of these two evolutionary models, since the very strong negative luminosity and density evolution does not allow any source beyond redshift $z = 3.5$ to be detected at any reasonable depth. The concentration effect is more dramatic on BCR11, where the colour constraints are the weakest, and the wings of the redshift distribution are strongly dependent on the prior information on the galaxy population that has been used. The sharpness of this distribution is thus due to the prior, and not to the colour constraints. In contrast, the sharpness of the distribution of LH850.1 is intrinsic to the well-determined colours of the source, and is almost independent of the prior.

The comparison of LH850.1 and BCR11 demonstrates the improved redshift accuracy that, in general, one can expect for those sources with the greatest combination of deep multiwavelength data. In the case of BCR11, it also illustrates the difficulty of constraining individual redshifts with observations at 1.4 GHz and 850 μm only. The redshift probability distributions of both sources have very similar modes ($z = 2.6$–2.8), yet for the less constraining evolutionary models (le1, le2, le1L13, le2L13) there remains 40–50 per cent and 25–35 per cent probabilities that BCR11 has a redshift >3 and >4 respectively. The corresponding probabilities for LH850.1 are 25–30 per cent and 5 per cent respectively. For models with a strong

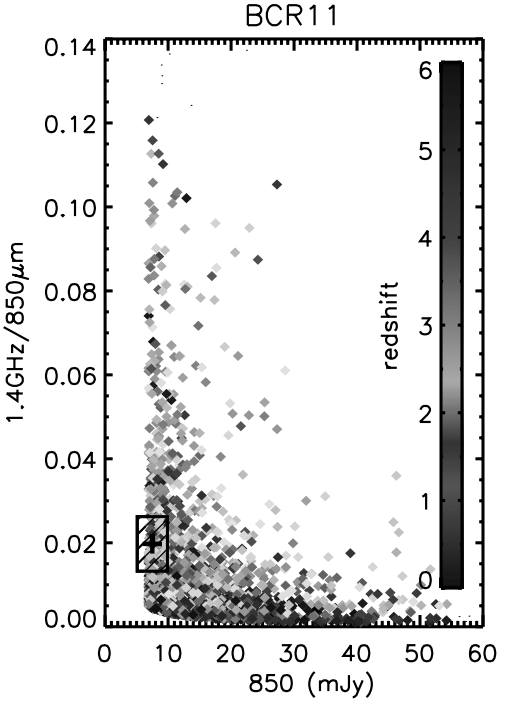

Figure 4. Colour–flux–redshift (*C*–*f*–*z*) plot for BCR11 (Barger et al. 2000). The description of the symbols is as in Fig. 1. This figure is available in colour in the online version of the journal on *Synergy*.

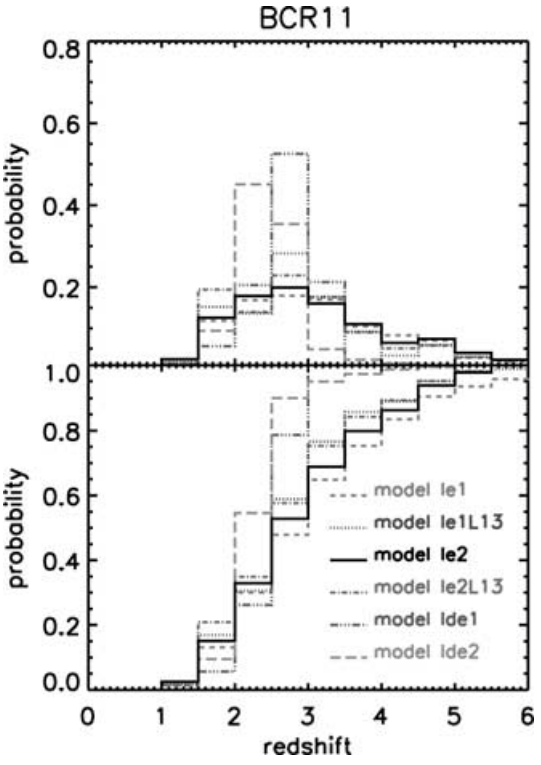

Figure 5. Redshift probability distributions for BCR11. The description of the plot is as in Fig. 2. This figure is available in colour in the online version of the journal on *Synergy*.

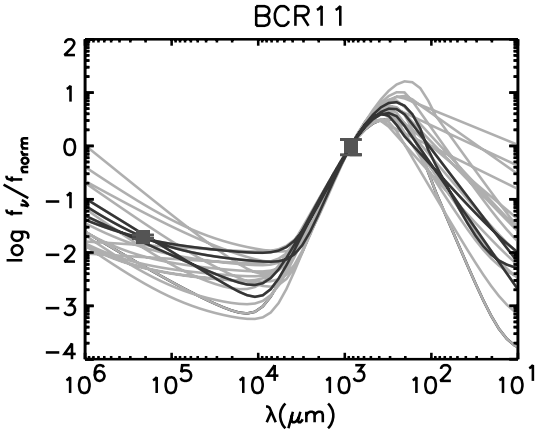

Figure 6. Comparison of the observed SED of BCR11 with those of template galaxies, redshifted to $z = 2.7$ (Table 2). The description of the plot is as in Fig. 3. Note that the selection of SEDs to represent BCR11 is different from that in LH850.1. This figure is available in colour in the online version of the journal on *Synergy*.

decline in the number of sources with redshift (led1, led2), the high-z tails are not produced. The sharpness of the derived redshift distributions is due to the lack of bright sources at high redshift, and not due to the colours of the galaxy.

Fig. 7 shows the manner in which the redshift distribution derived for LH850.1 (using model le2) degrades as different observational constraints are successively taken into account. When the 450-μm, 850-μm, 1.2-mm and 1.4-GHz detections are included in the analysis, the addition of upper limits to the SED makes no difference to the derived redshift distribution. It is also apparent that the distribution does not change significantly whilst the detection at 450 μm is used in the analysis, in combination with at least one additional band in the mm–sub-mm and radio regime. However, as soon as the 450-μm data are excluded, a high-redshift tail appears. This is due to the large intrinsic scatter in the 1.4-GHz/850-μm ratio amongst the template SEDs, which, in the absence of the 450-μm data, allows galaxies over a wide range of redshifts to satisfy the colour constraints. The elimination of the radio data from the analysis allows more low-redshift sources to be possible counterparts of the detected source, and hence this flattens the resulting redshift distribution.

The improvement in constraint on the photometric redshift is extremely important if it is to be used to determine the tuning of any broad-band mm–cm spectrograph, in an attempt to detect redshifted molecular CO lines. This is discussed further in Section 5. Higher-frequency radio observations at ∼5–15 GHz and deep 450-μm observations, including sensitive upper limits, are essential ground-based data that can provide the additional diagnostic power to constrain redshifts (e.g. LH850.1).

3.2 Individual redshift distributions

Before we calculate the cumulative redshift distribution for the 850-μm sources detected in the wide-area (>200 arcmin^2) blank-field SCUBA surveys, which include the Lockman Hole and ELAIS N2 regions (Scott et al. 2002; Fox et al. 2002), and the CUDSS fields (Lilly et al. 1999; Eales et al. 2000; Webb et al. 2003), it is instructive to discuss some of the typical redshift distributions that can be derived from data of different quality (i.e. sensitivity and wavelength coverage) for individual sources.

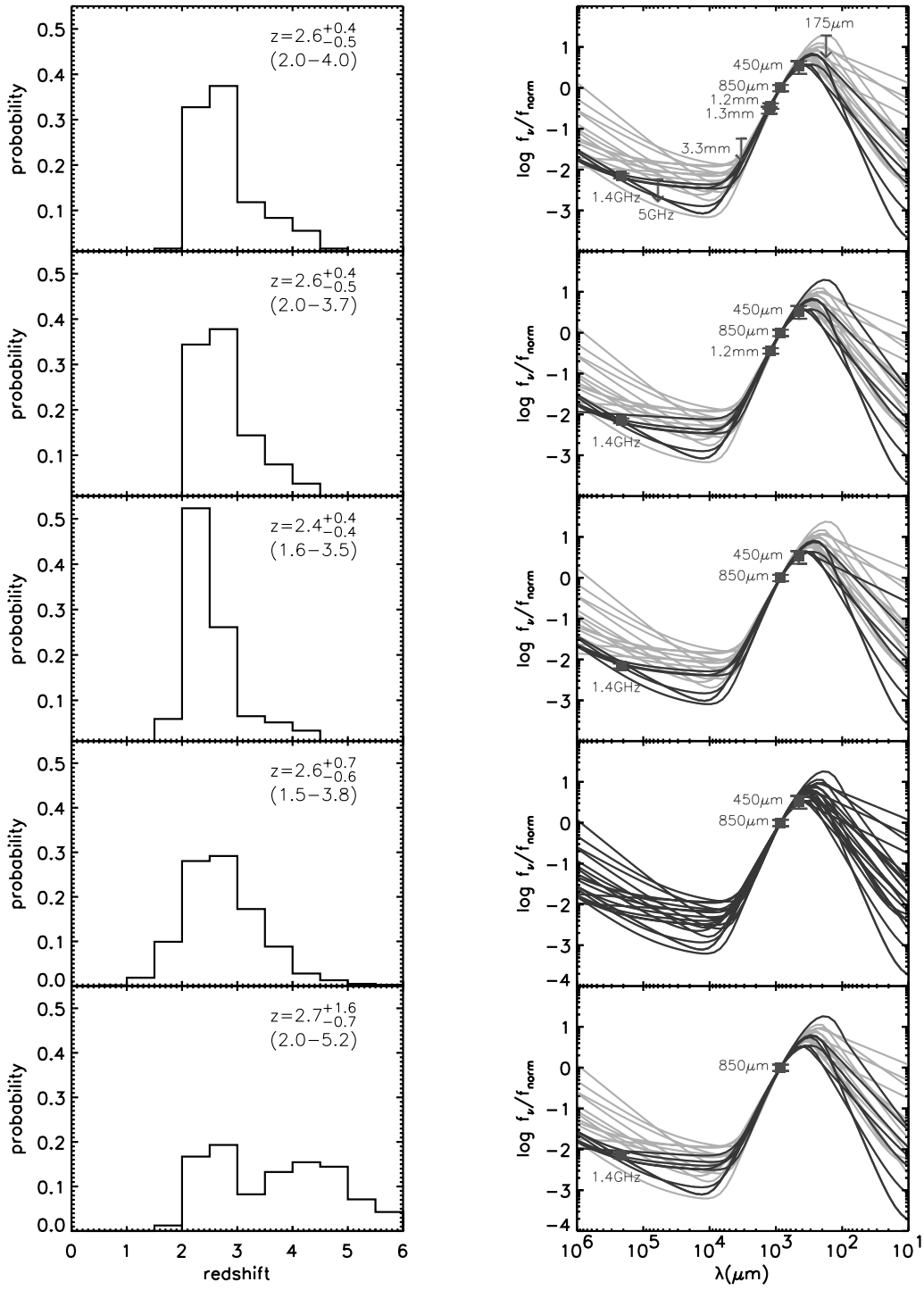

Figure 7. Redshift distributions and compatible template SEDs for LH850.1, when different photometry bands are taken into account. All estimates are based on a Monte Carlo produced with the same evolutionary model (le2). The SED models represented in the right-hand panels have been redshifted to the mode of distributions represented in the left. Symbol and line codes are as in Fig. 3. This figure is available in colour in the online version of the journal on *Synergy*.

Therefore, we compare the redshift distributions of wide-area blank-field sub-mm sources with those detected in various lensing-cluster surveys (Smail, Ivison & Blain 1997, 1999; Bertoldi et al. 2000; Chapman et al. 2002a). We also consider radio, FIR and UV-selected objects with follow-up sub-mm data (Barger et al. 2000; Scott et al. 2000; Chapman et al. 2000), and two bright sub-mm sources with extensive multiwavelength observations, HDF850.1 (Hughes et al. 1998; Downes et al. 1999; Dunlop et al. 2002) and the extremely red object HR10 (Dey et al. 1999).

Tables 1, 2 and 3 summarize the photometric redshifts of all the above sources: the modes of their redshift distributions, 68 per cent and 90 per cent confidence intervals derived from the six models studied in this paper, and other relevant information. Appendix A contains the *C–C–z*, *C–f–z*, *P–z* diagrams and SEDs of the

Table 1. Sources detected in three or more passbands at a $\geqslant 3\sigma$ level. Column 1 gives the name of the source; column 2 gives the references for the SED data; columns 3–8 give the mode of the photometric redshift distributions and 68 per cent confidence intervals for different evolutionary models, and, in parentheses below, the corresponding 90 per cent confidence intervals; and column 9 gives notes for each object. The references are coded as follows: (1) Lutz et al. (2001); (2) Scott et al. (2002); (3) Ivison et al. (2002); (4) Downes et al. (1999); (5) Dunlop et al. (2003); (6) Eales et al. (2000); (7) Smail et al. (1999); (8) Frayer et al. (2000); (9) Ivison et al. (1998); (10) Ivison et al. (2000); (11) Dey et al. (1999); (12) Chapman et al. (2002b); (13) Cowie, Barger & Kneib (2002). The *A* in the notes denotes the amplification factor reported in the literature for the lensed sources.

Object	Ref.	$z_{\rm phot}^{\rm le1}$	$z_{\rm phot}^{\rm le1L13}$	$z_{\rm phot}^{\rm le2}$	$z_{\rm phot}^{\rm le2L13}$	$z_{\rm phot}^{\rm lde1}$	$z_{\rm phot}^{\rm lde2}$	Notes
LH850.1	1, 2, 3	$2.6\pm^{0.4}_{0.6}$	$2.6\pm^{0.4}_{0.5}$	$2.6\pm^{0.4}_{0.5}$	$2.6\pm^{0.4}_{0.5}$	2.7 ± 0.3	$2.7\pm^{0.3}_{0.2}$	
		(2.0–4.1)	(2.0–3.8)	(2.0–3.7)	(2.0–3.9)	(2.0–3.1)	(2.3–3.5)	
LH850.3	2, 3	2.7 ± 0.2	2.7 ± 0.2	$3.0\pm^{0.0}_{0.5}$	$2.5\pm^{0.0}_{1.3}$	$2.9\pm^{0.6}_{1.2}$	$3.0\pm^{0.0}_{0.5}$	
		(2.1–3.0)	(1.8–3.0)	(2.1–3.0)	(1.0–3.0)	(1.0–3.5)	(2.1–3.0)	
LH850.8	2, 3	$3.8\pm^{1.2}_{1.4}$	$3.8\pm^{1.3}_{1.2}$	$3.7\pm^{1.5}_{0.7}$	$3.8\pm^{1.2}_{0.8}$	$3.5\pm^{0.0}_{0.6}$	$3.0\pm^{0.0}_{0.9}$	
		(2.0–6.5)	(1.6–6.0)	(2.3–6.0)	(2.0–5.3)	(2.6–3.5)	(2.0–4.3)	
LH850.12	2, 3	$0.6\pm^{0.3}_{0.1}$	$0.6\pm^{0.3}_{0.1}$	$0.2\pm^{0.8}_{0.2}$	$0.2\pm^{0.6}_{0.2}$	0.7 ± 0.2	1.0 ± 0.5	radio-loud QSO[(3)],
		(0.1–1.0)	(0.1–1.0)	(0.0–1.3)	(0.0–1.2)	(0.5–1.0)	(0.8–1.5)	$z_{\rm phot}$ is unreliable
N2850.1	2, 3	2.9 ± 0.6	$2.8\pm^{0.7}_{0.4}$	$2.8\pm^{0.7}_{0.5}$	$2.8\pm^{0.3}_{0.8}$	$2.9\pm^{0.3}_{0.4}$	$2.7\pm^{0.3}_{0.4}$	
		(2.0–4.1)	(2.0–3.7)	(2.0–4.1)	(2.0–5.3)	(2.4–3.5)	(2.0–3.5)	
N2850.2	2, 3	$2.3\pm^{0.6}_{0.3}$	$2.3\pm^{0.5}_{0.3}$	$2.3\pm^{0.6}_{0.3}$	$2.3\pm^{0.5}_{0.3}$	2.3 ± 0.3	$2.6\pm^{0.4}_{0.1}$	
		(1.5–3.4)	(1.5–3.2)	(1.5–3.5)	(1.5–3.0)	(2.0–3.4)	(2.1–3.0)	
N2850.4	2, 3	$2.8\pm^{1.7}_{0.3}$	2.7 ± 0.7	$2.9\pm^{1.2}_{0.9}$	$2.8\pm^{0.9}_{0.8}$	$2.8\pm^{0.5}_{0.3}$	$2.7\pm^{0.3}_{0.7}$	
		(1.3–4.5)	(2.0–4.5)	(1.2–4.5)	(1.6–4.5)	(2.2–3.5)	(1.5–3.4)	
HDF850.1	4, 5	$4.2\pm^{0.5}_{0.7}$	4.1 ± 0.6	4.1 ± 0.6	$4.0\pm^{0.7}_{0.5}$	$3.5\pm^{0.0}_{0.6}$	$4.0\pm^{0.5}_{0.6}$	$A = 3$
		(3.3–5.5)	(3.1–5.0)	(3.0–5.1)	(3.0–5.0)	(2.7–3.5)	(3.2–5.0)	
CUDSS14.1	6	$3.8\pm^{0.2}_{0.7}$	$3.8\pm^{0.8}_{0.7}$	$3.8\pm^{0.7}_{0.8}$	3.7 ± 0.8	2.9 ± 0.4	$2.8\pm^{1.1}_{0.8}$	
		(2.5–5.2)	(2.5–5.5)	(2.0–4.9)	(2.2–5.0)	(2.1–3.5)	(2.0–4.8)	
SMMJ 00266+1708	7, 8	$2.7\pm^{2.2}_{0.2}$	$2.7\pm^{2.0}_{0.2}$	$2.7\pm^{1.6}_{0.7}$	$2.8\pm^{2.2}_{0.2}$	$2.8\pm^{0.5}_{0.3}$	$2.9\pm^{0.5}_{0.4}$	$A = 1.6$
		(2.1–5.5)	(2.2–5.5)	(2.0–5.4)	(1.0–5.3)	(2.2–3.5)	(2.5–5.3)	
SMMJ 02399−0136	8, 9	$3.5\pm^{0.0}_{1.0}$	$3.1\pm^{0.8}_{0.6}$	3.9 ± 0.9	$3.1\pm^{0.7}_{0.6}$	$3.5\pm^{0.0}_{0.8}$	$3.8\pm^{1.7}_{0.8}$	$z_{\rm spec} = 2.8$, $A = 2.4$,
		(2.3–5.0)	(2.0–4.5)	(2.5–5.0)	(2.5–4.6)	(2.2–3.5)	(2.4–5.0)	AGN, 3.4 cm too low?
		2.8 ± 0.7	2.9 ± 0.6	$2.8\pm^{1.3}_{0.3}$	$2.8\pm^{0.7}_{0.5}$	$2.8\pm^{0.4}_{0.3}$	$2.8\pm^{0.8}_{0.3}$	disregarding the 3.4 cm
		(2.0–4.5)	(2.0–4.4)	(2.0–5.0)	(2.0–4.3)	(2.0–3.5)	(2.0–4.4)	upper limit
SMMJ 09429+4658	7, 13	$2.8\pm^{1.7}_{0.3}$	2.8 ± 0.6	$2.8\pm^{1.5}_{0.3}$	$2.8\pm^{0.7}_{0.4}$	$3.0\pm^{0.5}_{0.1}$	$2.7\pm^{0.3}_{0.6}$	$A = 1.5$
		(2.0–5.6)	(1.9–4.0)	(2.0–4.9)	(1.9–4.0)	(2.3–3.5)	(2.0–4.3)	
SMMJ 14009+0252	10	$4.4\pm^{0.7}_{0.9}$	$4.1\pm^{0.8}_{0.6}$	$4.4\pm^{0.7}_{0.9}$	4.1 ± 0.8	$3.5\pm^{0.0}_{0.9}$	$4.1\pm^{0.4}_{1.2}$	$A = 1.5$
		(2.7–5.5)	(3.0–5.1)	(3.1–5.0)	(2.5–5.2)	(2.1–3.5)	(2.0–5.0)	AGN contribution?
SMMJ 14011+0252	8	$2.8\pm^{0.5}_{0.8}$	$2.8\pm^{0.5}_{0.8}$	$2.7\pm^{0.6}_{0.7}$	$2.7\pm^{0.6}_{0.7}$	$2.7\pm^{0.6}_{0.2}$	$2.7\pm^{0.3}_{0.4}$	$z_{\rm spec} = 2.57$, $A = 3$
		(2.0–4.5)	(2.0–4.5)	(2.0–4.4)	(2.0–4.5)	(2.3–3.5)	(2.0–3.5)	
HR10	11	$1.5\pm^{1.0}_{0.0}$	$1.5\pm^{0.5}_{0.0}$	$1.5\pm^{0.8}_{0.0}$	$1.5\pm^{0.7}_{0.0}$	$1.5\pm^{1.0}_{0.0}$	$1.5\pm^{0.7}_{0.0}$	$z_{\rm spec} = 1.44$
		(1.5–3.1)	(1.5–2.5)	(1.5–2.9)	(1.5–2.6)	(1.5–3.1)	(1.5–2.4)	
N1-40	12	1.2 ± 0.2	$0.7\pm^{0.6}_{0.1}$	$0.6\pm^{0.6}_{0.1}$	0.6 ± 0.2	0.7 ± 0.2	$1.0\pm^{0.5}_{0.0}$	$z_{\rm spec} = 0.45$
		(0.6–1.5)	(0.5–1.5)	(0.5–1.5)	(0.3–1.0)	(0.5–1.0)	(0.5–1.5)	
N1-64	12	$1.2\pm^{0.3}_{0.8}$	1.2 ± 0.3	$1.2\pm^{0.8}_{0.3}$	$1.2\pm^{0.3}_{0.6}$	$1.2\pm^{0.3}_{0.6}$	$1.2\pm^{0.6}_{0.2}$	$z_{\rm spec} = 0.91$
		(0.5–1.8)	(0.5–1.5)	(0.5–2.1)	(0.5–1.8)	(–)	(0.7–2.0)	

galaxies listed in Tables 1 and 2, and also a selection of those listed in Table 3 for model le2, which is one of the less constraining models considered and serves as an illustration of the points made here.

When we have the most complete multiwavelength data set (rest-frame radio–sub-mm–FIR, including upper limits), then photometric redshifts can be constrained to a 68 per cent confidence band of width $\Delta z \sim \pm 0.5$ (Table 1 and Fig. A1). Those sub-mm galaxies for which just two detections, and perhaps some shallow upper limits, are available, do much worse, with accuracies at a 68 per cent confidence level of width $\Delta z \gtrsim \pm 1$ (Table 2 and Fig. A2). A merit of the Monte Carlo photometric redshift method is that it can determine redshift probability distributions even in the case that the galaxies have just been detected in one band (Table 3 and Fig. A3), the result being very flat redshift distributions that are highly dependent on the assumed evolutionary model. This is especially important because half of the sub-mm sources in the blank-field surveys belong to this category, although it is worth noting that several of these previously reported sub-mm sources have now been found to be spurious (Ivison et al. 2002).

Often, the well-constrained distributions are asymmetric, skewed towards lower redshifts with a high-redshift tail (e.g. LH850.1, N2850.2, HR10, ... in Figs 2 and A1). This is a natural consequence of the ability of the data (particularly with a deep 450-μm detection or upper limit, <30 mJy) to strongly reject the possibility of sub-mm galaxies lying at $z \lesssim 2$, whilst the same observational

Table 2. Sources detected in two passbands at $\geqslant 3\sigma$ level. The columns are identical to those described in Table 1. The reference codes are as follows: (1) Scott et al. (2002); (2) Ivison et al. (2002) (3) Barger et al. (2000); (4) Eales et al. (2000); (5) Webb et al. (2003); (6) Smail et al. (1999); (7) Chapman et al. (2002a); (8) Bertoldi et al. (2000); (9) Dannerbauer et al. (2002); (10) Chapman et al. (2002b).

Object	Ref.	$z^{\rm le1}_{\rm phot}$	$z^{\rm le1L13}_{\rm phot}$	$z^{\rm le2}_{\rm phot}$	$z^{\rm le2L13}_{\rm phot}$	$z^{\rm lde1}_{\rm phot}$	$z^{\rm lde2}_{\rm phot}$	Notes
LH850.6	1, 2	$2.7\pm^{2.0}_{0.7}$	$2.7\pm^{2.0}_{0.7}$	$2.7\pm^{1.8}_{0.7}$	$2.7\pm^{1.8}_{0.7}$	$2.7\pm^{0.6}_{0.2}$	$2.8\pm^{0.2}_{0.6}$	
		(2.0–6.4)	(2.0–6.2)	(2.0–5.4)	(2.0–5.4)	(2.3–3.5)	(2.0–4.4)	
LH850.7	1, 2	$3.6\pm^{1.9}_{0.8}$	$3.5\pm^{0.5}_{1.8}$	$3.6\pm^{0.4}_{1.9}$	$3.5\pm^{0.5}_{1.9}$	$3.5\pm^{0.0}_{1.0}$	$2.5\pm^{0.2}_{0.5}$	
		(1.6–5.5)	(1.5–5.1)	(1.5–5.3)	(1.5–5.3)	(1.7–3.5)	(1.5–3.8)	
LH850.14	1, 2	$2.5\pm^{1.9}_{0.4}$	$2.4\pm^{2.0}_{0.4}$	$2.4\pm^{1.9}_{0.4}$	$2.3\pm^{2.0}_{0.3}$	$2.7\pm^{0.3}_{0.5}$	$3.0\pm^{0.0}_{0.7}$	
		(1.5–6.3)	(1.5–5.5)	(2.0–5.4)	(2.0–5.4)	(2.0–3.4)	(2.0–3.5)	
LH850.16	1, 2	$3.6\pm^{1.0}_{1.6}$	$3.5\pm^{1.0}_{1.5}$	$3.3\pm^{1.1}_{1.3}$	$3.6\pm^{0.8}_{1.5}$	$2.8\pm^{0.5}_{0.3}$	$3.5\pm^{0.0}_{0.8}$	
		(1.5–6.0)	(1.5–6.1)	(2.0–5.5)	(2.0–5.4)	(2.0–3.5)	(1.5–3.5)	
LH850.18	1, 2	3.2 ± 1.1	$3.4\pm^{1.0}_{1.4}$	$3.0\pm^{1.1}_{1.0}$	$3.2\pm^{1.0}_{1.2}$	$3.2\pm^{0.3}_{0.7}$	$3.0\pm^{0.0}_{0.7}$	
		(1.5–5.8)	(1.5–5.6)	(1.5–4.9)	(1.8–4.9)	(2.0–3.5)	(2.0–3.3)	
N2850.7	1, 2	$2.8\pm^{1.5}_{0.8}$	$2.8\pm^{1.2}_{0.6}$	3.0 ± 1.0	3.0 ± 0.9	$3.0\pm^{0.3}_{0.5}$	2.5 ± 0.5	
		(1.9–5.5)	(2.0–5.3)	(1.5–4.9)	(1.7–5.0)	(2.5–3.5)	(2.0–4.3)	
N2850.13	1, 2	$2.7\pm^{0.8}_{1.0}$	$3.0\pm^{0.5}_{1.5}$	$2.7\pm^{0.8}_{1.0}$	$2.8\pm^{0.7}_{1.2}$	$2.8\pm^{0.5}_{0.3}$	$2.5\pm^{0.3}_{0.5}$	
		(1.5–5.0)	(1.5–5.0)	(1.5–4.6)	(1.5–4.8)	(2.0–3.5)	(2.0–3.5)	
BCR7	3	$2.7\pm^{0.8}_{1.1}$	$2.7\pm^{0.8}_{1.0}$	$2.2\pm^{1.1}_{0.7}$	$2.7\pm^{0.6}_{1.2}$	$2.8\pm^{0.5}_{0.3}$	2.4 ± 0.4	
		(1.5–4.8)	(1.5–4.7)	(1.5–4.8)	(1.5–4.7)	(1.9–3.5)	(1.5–3.2)	
BCR11	3	2.6 ± 0.9	2.7 ± 0.8	$2.7\pm^{0.8}_{0.9}$	$2.6\pm^{0.7}_{1.1}$	$2.7\pm^{0.6}_{0.2}$	2.4 ± 0.4	
		(1.5–4.7)	(1.5–4.7)	(1.5–4.6)	(1.5–4.7)	(2.1–3.5)	(1.5–3.0)	
BCR13	3	$2.3\pm^{1.9}_{0.3}$	$2.3\pm^{2.0}_{0.3}$	$2.3\pm^{1.7}_{0.3}$	$2.3\pm^{1.7}_{0.3}$	$2.8\pm^{0.7}_{0.3}$	$2.9\pm^{0.1}_{0.6}$	
		(1.5–5.5)	(1.5–5.6)	(1.5–4.7)	(1.5–4.7)	(2.2–3.5)	(2.0–3.3)	
BCR33	3	2.9 ± 1.0	3.0 ± 1.0	3.0 ± 1.0	3.0 ± 1.0	$3.0\pm^{0.5}_{0.3}$	$3.0\pm^{0.0}_{0.7}$	
		(1.5–5.2)	(1.5–5.3)	(1.5–4.6)	(1.5–4.5)	(2.0–3.5)	(2.0–3.0)	
BCR49	3	$2.3\pm^{1.1}_{0.5}$	2.4 ± 0.5	$2.4\pm^{1.1}_{0.6}$	$2.5\pm^{1.0}_{0.5}$	$2.7\pm^{0.3}_{0.7}$	$2.8\pm^{0.2}_{0.6}$	
		(1.6–4.5)	(1.5–4.2)	(1.0–4.0)	(1.0–3.7)	(1.7–3.5)	(1.6–3.0)	
CUDSS14.3	4	3.1 ± 0.9	3.1 ± 0.9	$3.2\pm^{0.8}_{1.0}$	3.1 ± 0.9	$3.5\pm^{0.0}_{0.8}$	$3.0\pm^{0.0}_{0.8}$	
		(1.7–5.0)	(1.5–4.8)	(2.0–5.0)	(1.7–5.0)	(2.2–3.5)	(2.2–4.1)	
CUDSS14.9	4	$2.6\pm^{0.8}_{0.6}$	$2.6\pm^{0.9}_{0.6}$	$2.5\pm^{0.5}_{1.0}$	$2.6\pm^{0.4}_{1.1}$	$2.7\pm^{0.8}_{0.2}$	$2.8\pm^{0.2}_{0.6}$	
		(1.5–4.1)	(1.5–4.0)	(1.5–4.5)	(1.5–4.0)	(2.0–3.4)	(1.9–3.5)	
CUDSS14.18	4	$0.7\pm^{0.8}_{0.4}$	$0.7\pm^{0.8}_{0.4}$	$0.7\pm^{0.8}_{0.4}$	$0.7\pm^{1.1}_{0.2}$	0.7 ± 0.7	$1.2\pm^{0.5}_{0.7}$	$z_{\rm spec} = 0.66$
		(0.0–1.8)	(0.0–1.8)	(0.0–1.8)	(0.0–2.0)	(0.0–1.9)	(0.2–2.0)	
CUDSS3.1	5	$2.1\pm^{0.4}_{0.6}$	$1.8\pm^{0.7}_{0.3}$	$1.7\pm^{0.7}_{0.2}$	$1.8\pm^{0.5}_{0.3}$	1.9 ± 0.4	$1.8\pm^{0.4}_{0.3}$	
		(1.0–2.5)	(0.7–2.5)	(1.5–2.5)	(0.9–2.5)	(1.5–2.6)	(1.2–2.5)	
CUDSS3.8	5	$2.1\pm^{0.9}_{0.2}$	2.0 ± 0.5	$2.0\pm^{0.8}_{0.5}$	2.0 ± 0.5	$2.6\pm^{0.4}_{0.2}$	1.9 ± 0.4	high 1.4 GHz, AGN?
		(1.4–3.0)	(1.4–3.0)	(1.0–3.0)	(1.2–3.0)	(2.0–3.0)	(1.2–2.5)	
CUDSS3.9	5	$1.0\pm^{0.2}_{0.5}$	$1.0\pm^{0.4}_{0.0}$	$1.1\pm^{0.7}_{0.1}$	$0.7\pm^{0.3}_{0.5}$	$1.0\pm^{0.4}_{0.0}$	$1.3\pm^{0.5}_{0.3}$	
		(0.5–1.5)	(1.0–2-0)	(0.5–2.0)	(0.0–1.4)	(1.0–1.5)	(0.6–2.0)	
CUDSS3.10	5	2.6 ± 0.8	2.6 ± 0.9	2.5 ± 1.0	2.5 ± 0.9	$2.7\pm^{0.8}_{0.2}$	$2.5\pm^{0.0}_{0.9}$	
		(1.4–4.5)	(1.3–4.5)	(1.5–4.5)	(1.0–4.2)	(1.9–3.5)	(1.0–2.5)	
CUDSS3.15	5	2.2 ± 0.7	2.3 ± 0.7	$2.2\pm^{0.9}_{0.7}$	2.3 ± 0.7	2.5 ± 0.5	$2.5\pm^{0.0}_{0.7}$	
		(1.0–3.7)	(1.5–4.0)	(1.5–4.0)	(1.0–3.7)	(1.9–3.5)	(1.2–2.5)	
SMMJ 02399−0134	6	2.2 ± 0.7	2.3 ± 0.8	2.3 ± 0.8	2.3 ± 0.8	$2.6\pm^{0.7}_{0.5}$	$2.5\pm^{0.0}_{0.8}$	$A = 2.5$, $z_{\rm spec} = 1.06$
		(1.0–3.6)	(1.4–4.0)	(1.0–3.8)	(1.0–3.7)	(1.7–3.5)	(1.2–2.5)	
SMMJ 10236+0412	7	2.3 ± 0.8	2.3 ± 0.8	2.3 ± 0.8	2.3 ± 0.8	$2.7\pm^{0.3}_{0.7}$	$2.8\pm^{0.2}_{0.5}$	$A = 3.2$
		(1.3–4.0)	(1.3–4.0)	(1.5–4.0)	(1.3–4.0)	(2.0–3.5)	(1.7–3.0)	
SMMJ 10237+0410	7	$2.0\pm^{1.1}_{0.5}$	$2.0\pm^{1.2}_{0.5}$	$2.1\pm^{1.0}_{0.6}$	$2.0\pm^{1.1}_{0.5}$	2.6 ± 0.6	2.4 ± 0.4	$A = 3.7$
		(1.0–3.5)	(1.0–3.7)	(1.0–3.6)	(1.0–3.6)	(1.7–3.5)	(1.6–3.0)	
SMMJ 16403+4644	7	2.2 ± 0.8	2.2 ± 0.8	$2.1\pm^{0.4}_{1.1}$	2.2 ± 0.7	$2.4\pm^{0.6}_{0.8}$	2.5 ± 0.4	$A = 3.0$
		(0.5–3.1)	(0.8–3.5)	(1.0–3.5)	(0.5–3.5)	(1.2–3.5)	(1.6–3.0)	
SMMJ 16403+46440	7	2.8 ± 0.7	2.8 ± 0.7	2.7 ± 0.8	2.8 ± 0.7	$2.8\pm^{0.6}_{0.3}$	$2.9\pm^{0.1}_{0.7}$	$A = 3.6$
		(1.5–4.1)	(1.5–4.1)	(1.5–4.1)	(1.5–4.1)	(2.1–3.5)	(1.5–3.1)	
SMMJ 16403+46437	7	$2.2\pm^{0.8}_{0.6}$	$2.3\pm^{0.7}_{0.8}$	$2.6\pm^{0.4}_{1.1}$	$2.6\pm^{0.4}_{1.0}$	2.6 ± 0.5	2.5 ± 0.5	$A = 3.2$, 1.4 GHz high,
		(1.0–3.3)	(1.1–3.5)	(1.0–3.3)	(1.2–3.5)	(1.8–3.5)	(1.5–3.0)	AGN?
MMJ 154127+6615	8	$2.8\pm^{1.7}_{0.5}$	$3.6\pm^{0.9}_{1.4}$	$2.8\pm^{1.7}_{0.3}$	$3.7\pm^{0.8}_{1.2}$	2.7 ± 0.3	2.8 ± 0.3	$A = 1$
		(2.0–6.0)	(2.0–5.9)	(2.0–5.0)	(2.0–5.0)	(2.0–3.1)	(2.0–4.1)	

Table 2 – *continued*

Object	Ref.	$z_{\rm phot}^{\rm le1}$	$z_{\rm phot}^{\rm le1L13}$	$z_{\rm phot}^{\rm le2}$	$z_{\rm phot}^{\rm le2L13}$	$z_{\rm phot}^{\rm lde1}$	$z_{\rm phot}^{\rm lde2}$	Notes
MMJ 154127+6616	8	$2.8\pm^{1.7}_{0.3}$	$2.8\pm^{2.0}_{0.3}$	$2.8\pm^{1.8}_{0.3}$	$2.8\pm^{2.2}_{0.3}$	$3.0\pm^{0.5}_{0.4}$	$2.9\pm^{1.0}_{0.4}$	$A = 1$
		(2.0–6.0)	(2.0–6.0)	(2.5–5.0)	(2.1–5.0)	(2.2–3.5)	(2.6–5.3)	
MMJ 120546−0741.5	9	$4.7\pm^{1.3}_{1.9}$	$3.4\pm^{2.7}_{1.9}$	$3.8\pm^{2.1}_{0.3}$	$3.8\pm^{2.0}_{0.3}$	$3.0\pm^{0.2}_{0.5}$	3.5±1.0	
		(2.5–7.8)	(2.5–7.0)	(3.0–6.0)	(2.5–6.0)	(2.5–3.4)	(2.5–6.0)	
MMJ 120539−0745.4	9	$2.8\pm^{1.7}_{0.6}$	$2.8\pm^{1.7}_{0.8}$	$2.8\pm^{1.7}_{0.3}$	$2.5\pm^{1.7}_{0.5}$	2.5±0.3	$2.8\pm^{0.2}_{0.6}$	
		(2.0–6.3)	(2.0–6.0)	(2.0–4.9)	(2.0–5.3)	(2.0–3.3)	(2.0–3.7)	
N1−008	10	$0.0\pm^{0.5}_{0.0}$	$0.0\pm^{0.5}_{0.0}$	$0.0\pm^{0.4}_{0.0}$	$0.0\pm^{0.4}_{0.0}$	$0.0\pm^{0.4}_{0.0}$	$0.0\pm^{0.4}_{0.0}$	
		(0.0–0.5)	(0.0–0.5)	(0.0–0.5)	(0.0–0.5)	(0.0–0.5)	(0.0–0.5)	

data cannot reject the possibility that the sub-mm galaxies lie at a much higher redshift, $z \gg 3$. Examples of the power with which the 450-μm detections or upper limits can reject $z \lesssim 2$ can be seen in the SEDs of LH850.1 and HDF850.1 (Figs 3 and A1), respectively. On the other hand, the bright ISOPHOT detections at 170 μm (>120 mJy) make a strong case that the sources lie at $z \lesssim 2$, for example N1-40, N1-64 (Fig. A1) and N1-8 (Fig. A2), whilst the ISOPHOT non-detections are too shallow to offer any additional constraints on the SEDs of the majority of the sub-mm population (e.g. LH850.1, HDF850.1 in Figs 3 and A1).

It is also possible to obtain a bimodal redshift probability distribution for some galaxies (e.g. SMMJ 00266+1708 in Fig. A1, BCR33 in Fig. A2), an effect created by two or more template SEDs reproducing the same observed colours at very different redshifts.

The figures in Appendix A show the insensitivity of the 850-μm/1.4-GHz ratio to redshift when the sources are at $z \gtrsim 2$ (a point also made by CY99 and CY00). The redshift distributions in these cases are usually shallow, with long high-redshift tails (e.g. BCR11, BCR13, MMJ 154127+6615, in Fig. A2), although exceptions also occur (SMMJ 16403+4644 in Fig. A2). The distributions are even broader in the cases when only a sub-mm detection and a radio upper limit are available (Fig. A3). All these redshift distributions are narrower for those evolutionary models with a strong decline beyond $z \sim 2$–3, as can be seen from the measurements in Tables 2 and 3, especially for lde1, which essentially contains no sources at high z.

A quick browse through Appendix A illustrates the variety of template SEDs that reproduce the colours of an individual sub-mm galaxy, which lends support to the use of a template library in the derivation of the photometric redshifts. A few sub-mm sources, however, still cannot be reproduced at any redshift with the template SEDs available (e.g. LH850.12, SMMJ 16403+46437). A possible explanation for this problem is the contribution of AGN emission to the radio fluxes at a level not included in the SEDs of the template library, or a misidentification of a sub-mm galaxy with a nearby radio source (see also Section 4). A wider range of SEDs, including modest fractions of galaxies with an excess of radio emission, could partially solve this problem, but, on the other hand, it would also introduce an extra error term in the redshift computation for the rest of the sub-mm galaxies. Other sub-mm galaxies have only a small representation of analogues among the mock galaxies (e.g. N1-40, SMMJ 14009+0252), most probably because they are rare objects in the Universe, either by their intrinsically high luminosity or their low redshift. This latter point is illustrated by the rarity of mock galaxies in the corresponding C–C–z or C–f–z diagrams, assuming any of the evolutionary scenarios considered in this paper.

3.2.1 Accuracy of the photometric redshift method

Fig. 8 shows the comparison of photometric and published spectroscopic redshifts for eight galaxies: in order of increasing spectroscopic redshift, N1-40, CUDSS14.18, N1-64, SMMJ 02399−0134, HR10, SMMJ 14011+0252, SMMJ 02399−0136 and W-MM11.

The two galaxies that depart most from the $z_{\rm phot} = z_{\rm spec}$ line are SMMJ 02399−0134 and W-MM11. The first has a photometric redshift calculated only on the basis of its 1.4-GHz/850-μm colour (Fig. A2), and the latter on a 850-μm detection with a 450-μm upper limit (Fig. A3). These two objects illustrate the large confidence intervals that have to be considered when the redshifts are derived from a single colour. Specifically, SMMJ 02399−0134 illustrates the uncertainties attached to the large dispersion of 1.4-GHz/850-μm colours implied from a local sample of galaxies. The agreement between spectroscopic and photometric redshifts for the remaining six galaxies (with more than one colour available) is remarkably good. The asymmetry of the error bars is a reflection of the skewness of their respective P–z distributions (Figs A1 and A2). These sources illustrate the importance of obtaining the description of the whole redshift distribution instead of relying on measurements of the median, which departs significantly from the most probable redshift in skewed distributions.

A larger sample of spectroscopic redshifts is obviously essential to assess the statistical significance of the goodness of this technique, and the accuracy of the error bars we derive. For the sources with more than one measured colour, these errors are mainly the result of the scatter in the shapes of the template SEDs. A larger sample of spectroscopic redshifts would allow us to fine-tune the selection of SEDs and priors in order to trim the error bars if, for instance, the modes of the distributions do not populate the envelope of error bars implied from the analysis. The six best-constrained redshift distributions (shown in black in Fig. 8) do show a tendency to cluster more around the $z_{\rm spec} = z_{\rm phot}$ line than the collective extension of their error bars. However, fine-tuning the inputs of the Monte Carlo at this early stage of confirmation of the photometric redshifts is premature.

3.2.2 Notes on individual sources

LH850.1 Other redshift estimates are $2.95^{+1.49}_{-0.985}$ based on the 1.4-GHz/850-μm spectral index technique; and 2.72 ± 0.37 based on a χ^2 minimization with one template SED (YC02). Our own estimate $z = 2.6^{+0.4}_{-0.5}$ (le2) is consistent with these measurements.

LH850.12 No SED can reproduce the observed photometry of this source. Ivison et al. (2002) find evidence of variability at 1.4 GHz, and report associated X-ray emission. They conclude that LH850.12

Table 3. Sources detected at 850 μm or 1.2 mm at a $\geqslant 3.5\sigma$ level, and undetected at any other wavelength. The columns are identical to those described in Table 1. The reference codes are as follows: (1) Scott et al. (2002); (2) Eales et al. (2000); (3) Webb et al. (2003); (4) Smail et al. (1999); (5) Chapman et al. (2002a); (6) Dannerbauer et al. (2002); (7) Ivison et al. (2002).

Object	Ref.	$z^{\rm le1}_{\rm phot}$	$z^{\rm le1L13}_{\rm phot}$	$z^{\rm le2}_{\rm phot}$	$z^{\rm le2L13}_{\rm phot}$	$z^{\rm lde1}_{\rm phot}$	$z^{\rm lde2}_{\rm phot}$	Notes
LH850.2	1, 7	$5.9\pm^{1.3}_{2.4}$	$5.5\pm^{1.5}_{1.9}$	$5.8\pm^{0.2}_{1.7}$	$5.1\pm^{0.4}_{1.5}$	$3.5\pm^{0.0}_{0.5}$	$4.3\pm^{1.2}_{0.8}$	
		(3.5–9.0)	(3.3–8.5)	(3.3–6.0)	(3.3–6.0)	(2.7–3.5)	(3.2–6.0)	
LH850.4	1, 7	$5.5\pm^{2.0}_{1.8}$	$5.3\pm^{2.2}_{1.4}$	$4.7\pm^{1.3}_{0.5}$	$4.6\pm^{1.4}_{0.5}$	$3.5\pm^{0.0}_{0.6}$	$3.9\pm^{1.7}_{0.4}$	
		(3.0–8.8)	(3.0–8.5)	(3.5–6.0)	(3.3–6.0)	(2.6–3.5)	(3.0–6.0)	
LH850.5	1, 7	$5.3\pm^{2.2}_{1.3}$	$6.1\pm^{1.5}_{1.7}$	$4.7\pm^{1.3}_{0.5}$	$6.0\pm^{0.0}_{1.9}$	$3.5\pm^{0.0}_{0.6}$	4.5 ± 1.0	
		(3.3–9.0)	(3.0–8.5)	(3.4–6.0)	(3.4–6.0)	(2.6–3.5)	(3.0–6.0)	
LH850.13	1, 7	$4.9\pm^{2.6}_{1.4}$	$5.1\pm^{2.1}_{1.6}$	5.0 ± 1.0	5.0 ± 1.0	$3.5\pm^{0.0}_{0.6}$	4.6 ± 1.2	
		(3.0–8.8)	(3.0–8.4)	(3.0–6.0)	(3.3–6.0)	(2.6–3.5)	(2.7–6.0)	
N2850.3	1, 7	$4.8\pm^{2.8}_{0.8}$	$4.6\pm^{2.9}_{0.6}$	$5.8\pm^{0.2}_{1.4}$	4.8 ± 0.9	$3.5\pm^{0.0}_{0.5}$	4.3 ± 1.0	
		(3.5–9.0)	(3.5–8.8)	(3.6–6.0)	(3.6–6.0)	(2.7–3.5)	(3.2–6.0)	
N2850.5	1, 7	5.0 ± 2.0	$4.7\pm^{2.3}_{1.4}$	$5.0\pm^{0.7}_{1.5}$	$4.5\pm^{1.5}_{0.6}$	$3.5\pm^{0.0}_{0.7}$	$2.5\pm^{2.0}_{0.5}$	
		(2.5–8.6)	(2.7–8.5)	(2.9–6.0)	(2.9–6.0)	(2.5–3.5)	(3.0–6.0)	
N2850.6	1, 7	5.0 ± 2.0	$4.8\pm^{1.9}_{2.3}$	$4.8\pm^{0.8}_{1.3}$	4.8 ± 1.2	$3.5\pm^{0.0}_{0.8}$	$2.5\pm^{1.9}_{0.5}$	
		(2.5–8.7)	(2.5–8.3)	(3.0–6.0)	(2.5–6.0)	(2.5–3.5)	(2.0–5.6)	
N2850.8	1, 7	$4.0\pm^{2.7}_{1.5}$	$4.7\pm^{2.0}_{2.2}$	$4.5\pm^{1.0}_{1.5}$	4.8 ± 1.2	$3.0\pm^{0.5}_{0.3}$	$2.5\pm^{0.3}_{1.0}$	
		(2.1–8.5)	(2.0–8.4)	(2.6–6.0)	(2.6–6.0)	(2.3–3.5)	(2.5–6.0)	
N2850.9	1, 7	$5.2\pm^{2.0}_{1.7}$	$5.0\pm^{2.0}_{1.8}$	$5.9\pm^{0.1}_{1.8}$	5.0 ± 1.0	$3.5\pm^{0.0}_{0.6}$	$3.7\pm^{1.5}_{0.7}$	
		(3.0–9.0)	(2.8–8.5)	(3.2–6.0)	(3.1–6.0)	(2.6–3.5)	(2.5–6.0)	
N2850.10	1, 7	$4.7\pm^{2.3}_{1.9}$	$4.5\pm^{2.5}_{1.7}$	$4.7\pm^{0.8}_{1.6}$	4.8 ± 1.2	$3.5\pm^{0.0}_{0.8}$	$2.5\pm^{0.5}_{1.0}$	
		(2.1–8.5)	(2.1–8.5)	(2.6–6.0)	(2.6–6.0)	(2.3–3.5)	(1.5–4.8)	
N2850.11	1, 7	5.5 ± 1.9	$4.6^{2.9}_{0.9}$	5.0 ± 1.0	$4.8^{1.2}_{0.8}$	$3.5\pm^{0.0}_{0.7}$	4.1 ± 1.2	
		(3.0–8.9)	(3.0–8.7)	(3.2–6.0)	(3.2–6.0)	(2.6–3.5)	(2.6–6.0)	
CUDSS14.2	2	$5.2\pm^{2.4}_{1.7}$	$5.0\pm^{2.5}_{1.6}$	$4.7\pm^{0.8}_{1.0}$	$5.0\pm^{0.7}_{1.5}$	$3.5\pm^{0.0}_{0.7}$	$2.5\pm^{1.2}_{1.0}$	
		(2.5–8.7)	(2.5–8.8)	(2.9–6.0)	(2.8–6.0)	(2.5–3.5)	(1.5–5.1)	
CUDSS14.4	2	$5.0\pm^{2.6}_{1.5}$	$5.1\pm^{2.5}_{1.6}$	$4.6\pm^{1.4}_{0.8}$	$4.7\pm^{1.3}_{0.9}$	$3.5\pm^{0.0}_{0.8}$	$2.5\pm^{1.2}_{1.0}$	
		(2.5–8.8)	(2.5–8.8)	(2.9–6.0)	(2.8–6.0)	(2.4–3.5)	(1.5–5.2)	
CUDSS14.5	2	$4.8\pm^{2.6}_{1.3}$	$4.9\pm^{2.7}_{1.4}$	$4.8\pm^{1.2}_{0.8}$	$5.3\pm^{0.7}_{1.2}$	$3.5\pm^{0.0}_{0.8}$	$2.5\pm^{1.9}_{0.5}$	
		(2.8–9.0)	(2.8–9.0)	(3.0–6.0)	(3.0–6.0)	(2.5–3.5)	(2.0–5.7)	
CUDSS14.6	2	$4.7\pm^{2.8}_{1.5}$	$4.7\pm^{3.0}_{1.2}$	$5.2\pm^{0.8}_{1.3}$	$5.2\pm^{0.8}_{1.3}$	$3.5\pm^{0.0}_{0.8}$	$2.5\pm^{1.4}_{1.0}$	
		(2.5–8.8)	(2.5–8.8)	(2.9–6.0)	(2.9–6.0)	(2.5–3.5)	(1.5–5.3)	
CUDSS14.8	2	$4.7\pm^{2.6}_{1.7}$	$4.7\pm^{2.0}_{2.2}$	$4.5\pm^{1.3}_{1.0}$	$4.7\pm^{1.9}_{1.2}$	$3.5\pm^{0.0}_{0.8}$	$2.5\pm^{0.8}_{1.0}$	
		(2.5–9.0)	(2.5–9.0)	(2.6–6.0)	(2.6–6.0)	(2.3–3.5)	(1.5–5.0)	
CUDSS14.10	2	$4.7\pm^{2.6}_{1.7}$	$4.8\pm^{2.5}_{1.8}$	$3.9\pm^{2.0}_{0.4}$	4.3 ± 1.2	2.9 ± 0.5	$2.5\pm^{0.5}_{1.0}$	
		(2.5–9.0)	(2.5–9.0)	(2.6–6.0)	(2.6–6.0)	(2.3–3.5)	(1.5–4.8)	
CUDSS3.2	3	$4.5\pm^{1.8}_{2.2}$	$3.8\pm^{2.7}_{1.6}$	$3.5\pm^{1.7}_{1.0}$	3.9 ± 1.4	2.9 ± 0.5	$2.5\pm^{0.0}_{0.9}$	
		(2.0–8.5)	(1.9–8.5)	(2.0–5.8)	(2.2–6.0)	(2.2–3.5)	(1.0–4.0)	
CUDSS3.3	3	$3.8\pm^{2.5}_{1.5}$	$3.7\pm^{2.4}_{1.7}$	$4.0\pm^{1.2}_{1.5}$	$4.0\pm^{1.3}_{1.5}$	2.9 ± 0.4	$2.5\pm^{0.0}_{0.9}$	
		(2.0–8.4)	(2.0–8.4)	(2.2–6.0)	(2.0–5.8)	(2.1–3.5)	(1.0–4.0)	
CUDSS3.4	3	$3.2\pm^{2.9}_{1.2}$	$3.7\pm^{2.8}_{1.7}$	$4.3\pm^{0.9}_{1.2}$	3.9 ± 1.4	2.9 ± 0.4	$2.5\pm^{0.0}_{1.0}$	
		(2.0–8.5)	(2.0–8.3)	(2.3–6.0)	(2.2–6.0)	(2.2–3.5)	(1.0–4.0)	
CUDSS3.5	3	$3.7\pm^{2.6}_{1.7}$	$3.7\pm^{2.6}_{1.4}$	$3.8\pm^{1.5}_{1.3}$	3.9 ± 1.4	2.9 ± 0.5	$2.5\pm^{0.0}_{1.0}$	
		(1.8–8.5)	(1.8–8.5)	(2.0–5.9)	(2.0–5.8)	(2.1–3.5)	(1.0–3.9)	
CUDSS3.6	3	$3.7\pm^{2.6}_{1.7}$	$4.0\pm^{2.4}_{2.0}$	$3.7\pm^{1.5}_{1.2}$	3.9 ± 1.4	2.9 ± 0.4	$2.5\pm^{0.0}_{1.0}$	
		(2.0–8.7)	(2.0–8.8)	(2.0–5.8)	(2.0–5.8)	(2.2–3.5)	(1.0–3.9)	
CUDSS3.7	3	$3.7\pm^{2.6}_{1.2}$	$3.7\pm^{2.6}_{1.2}$	$4.0\pm^{1.5}_{1.2}$	3.7 ± 1.3	$2.8\pm^{0.5}_{0.3}$	$2.5\pm^{0.0}_{1.0}$	
		(2.0–8.4)	(2.0–8.1)	(2.3–6.0)	(2.0–5.7)	(2.0–3.5)	(1.4–4.5)	
CUDSS3.11	3	$3.8\pm^{3.0}_{1.3}$	$4.5\pm^{1.7}_{2.5}$	$3.8\pm^{1.7}_{1.0}$	$3.7\pm^{1.8}_{0.9}$	2.9 ± 0.4	$2.5\pm^{0.0}_{1.0}$	
		(1.9–8.5)	(2.0–8.5)	(2.3–6.0)	(2.0–5.7)	(2.2–3.5)	(1.0–4.1)	
CUDSS3.12	3	$3.7\pm^{2.6}_{1.7}$	$3.2\pm^{2.1}_{1.2}$	$3.5\pm^{1.8}_{1.0}$	3.9 ± 1.3	2.9 ± 0.5	$2.5\pm^{0.0}_{1.0}$	
		(1.9–8.5)	(1.9–8.5)	(2.0–5.8)	(2.0–5.8)	(2.2–3.5)	(1.0–3.9)	
CUDSS3.13	3	$4.0\pm^{2.3}_{2.0}$	$3.2\pm^{2.2}_{1.5}$	$3.5\pm^{1.8}_{1.0}$	3.9 ± 1.4	2.9 ± 0.5	$2.5\pm^{0.0}_{1.0}$	
		(1.8–8.5)	(1.7–8.5)	(2.0–5.8)	(2.1–6.0)	(2.1–3.5)	(1.0–4.0)	

Table 3 – *continued*

Object	Ref.	$z_{\rm phot}^{\rm le1}$	$z_{\rm phot}^{\rm le1L13}$	$z_{\rm phot}^{\rm le2}$	$z_{\rm phot}^{\rm le2L13}$	$z_{\rm phot}^{\rm lde1}$	$z_{\rm phot}^{\rm lde2}$	Notes
CUDSS3.16	3	$3.5\pm^{2.9}_{1.5}$	$3.2\pm^{2.2}_{1.2}$	$3.7\pm^{1.5}_{1.2}$	$3.5\pm^{1.9}_{1.0}$	2.9±0.4	$2.5\pm^{0.0}_{1.0}$	
		(1.6–8.5)	(1.6–8.5)	(2.1–6.0)	(2.0–5.9)	(2.2–3.5)	(1.0–3.8)	
SMMJ 02400−0134	4	$5.0\pm^{2.6}_{1.5}$	$5.2\pm^{2.3}_{1.7}$	$4.9\pm^{1.1}_{0.9}$	$5.2\pm^{0.8}_{1.2}$	$3.5\pm^{0.0}_{0.7}$	$4.0\pm^{0.7}_{2.0}$	$A > 1.9$ (2.5?)
		(3.0–9.1)	(3.0–9.1)	(3.1–6.0)	(3.1–6.0)	(2.5–3.5)	(2.0–5.5)	
SMMJ 04431+0210 (N4)	4	$4.5\pm^{2.5}_{1.6}$	$4.6\pm^{2.2}_{1.6}$	$4.5\pm^{1.4}_{1.0}$	$4.2\pm^{1.6}_{0.7}$	$3.5\pm^{0.0}_{0.7}$	2.4±1.0	$A > 1.$
		(2.5–8.8)	(2.5–8.7)	(2.7–6.0)	(2.7–6.0)	(2.5–3.5)	(1.5–4.9)	
SMMJ 04541−0302	5	$4.7\pm^{2.0}_{2.2}$	$4.0\pm^{2.6}_{1.5}$	4.7±1.2	$4.7\pm^{0.8}_{1.6}$	$3.0\pm^{0.5}_{0.3}$	$2.5\pm^{0.6}_{1.0}$	$A = 2.6$
		(2.2–8.5)	(2.3–8.5)	(2.6–6.0)	(2.6–6.0)	(2.4–3.5)	(1.5–4.7)	
SMMJ 04542−0301	5	4.7±2.2	$4.3\pm^{2.7}_{1.5}$	$4.2\pm^{1.7}_{0.7}$	$4.5\pm^{1.4}_{1.0}$	$3.3\pm^{0.2}_{0.6}$	$2.5\pm^{0.9}_{1.0}$	$A = 4.5$
		(2.5–8.9)	(2.1–8.5)	(2.7–6.0)	(2.6–6.0)	(2.4–3.5)	(1.5–4.9)	
SMMJ 04543+0256	5	$3.9\pm^{2.7}_{1.4}$	$3.8\pm^{2.7}_{1.6}$	$4.0\pm^{1.5}_{1.1}$	$4.0\pm^{1.5}_{1.1}$	2.9±0.4	$2.5\pm^{0.0}_{1.0}$	$A = 3.1$
		(2.0–8.4)	(2.0–8.5)	(2.4–6.0)	(2.0–6.0)	(2.0–3.5)	(1.5–4.5)	
SMMJ 04543+0257	5	$4.7\pm^{2.2}_{1.7}$	$4.5\pm^{2.1}_{1.5}$	$4.2\pm^{1.3}_{1.1}$	$4.5\pm^{1.0}_{1.4}$	$3.5\pm^{0.0}_{0.8}$	$2.5\pm^{0.7}_{1.0}$	$A = 3.4$
		(2.0–8.2)	(2.5–8.3)	(2.6–6.0)	(2.6–6.0)	(2.3–3.5)	(1.5–4.8)	
SMMJ 10237+0412	5	$4.0\pm^{2.9}_{1.5}$	$3.9\pm^{3.0}_{1.4}$	$4.5\pm^{0.7}_{2.0}$	$4.7\pm^{0.8}_{1.8}$	2.9±0.4	$2.5\pm^{0.0}_{1.0}$	$A = 3.5$
		(2.0–8.7)	(2.0–8.7)	(2.0–6.0)	(2.6–6.0)	(2.2–3.5)	(1.0–4.1)	
SMMJ 14573+2220	5	$4.0\pm^{2.7}_{1.5}$	$4.2\pm^{2.6}_{1.7}$	$4.0\pm^{1.6}_{1.0}$	$4.2\pm^{1.8}_{0.8}$	2.9±0.4	$2.5\pm^{0.1}_{1.0}$	$A = 2.8$
		(2.0–8.5)	(2.0–8.6)	(2.0–6.0)	(2.5–6.0)	(2.2–3.5)	(1.5–4.7)	
SMMJ 17223+3207	5	$4.0\pm^{2.5}_{1.5}$	$4.2\pm^{2.6}_{1.7}$	$3.9\pm^{1.6}_{1.0}$	$4.0\pm^{1.1}_{1.5}$	$3.0\pm^{0.3}_{0.5}$	$2.5\pm^{0.1}_{1.1}$	$A = 2.8$
		(2.0–8.4)	(2.0–8.4)	(2.4–6.0)	(2.5–6.0)	(2.2–3.5)	(1.5–4.6)	
SMMJ 22471−0206	4	$4.8\pm^{2.4}_{1.8}$	$4.8\pm^{2.3}_{1.8}$	$4.7\pm^{1.3}_{0.9}$	4.9±1.1	$3.4\pm^{0.1}_{0.6}$	$2.9\pm^{1.3}_{1.0}$	$A > 1.9$ (2.5?)
		(2.5–8.8)	(2.5–8.8)	(2.8–6.0)	(2.8–6.0)	(2.5–3.5)	(1.5–5.2)	
MMJ 120517−0743.1	6	$7.0\pm^{1.5}_{2.4}$	$7.1\pm^{1.4}_{2.6}$	$6.0\pm^{0.0}_{1.6}$	$6.0\pm^{0.0}_{1.6}$	$3.5\pm^{0.0}_{0.4}$	$4.4\pm^{1.4}_{0.4}$	
		(4.3–10.)	(4.3–10.)	(3.6–6.0)	(3.5–6.0)	(2.7–3.5)	(3.5–6.0)	
W-MM11	5	$4.2\pm^{2.0}_{2.2}$	$3.4\pm^{2.9}_{1.5}$	$3.7\pm^{1.6}_{1.2}$	$3.9\pm^{1.6}_{1.2}$	2.9±0.4	$2.5\pm^{0.0}_{0.9}$	$z_{\rm spec} = 2.98$
		(2.0–8.7)	(2.0–8.6)	(2.0–5.8)	(2.2–6.0)	(2.0–3.5)	(1.0–4.0)	

might be a radio-loud quasi-stellar object (QSO). This kind of object is actually not represented among our SEDs, and thus the redshift we derive is unreliable. Note that there are no counterpart mock galaxies in the vicinity of the error box of its *C*–*C*–*z* diagram in Fig. A1.

HDF850.1 Other redshift estimates are >2.6, based on the 1.4-GHz/850-μm spectral index technique; and 4.11 ± 0.51 based on a χ^2 minimization with one template SED (YC02). Our own estimate $z = 4.1^{+0.6}_{-0.5}$ (le2) is in good agreement with these measurements, and is unaffected by the inclusion or exclusion of the possible lensing amplification experienced by this source ($A \approx 3$, Dunlop et al. 2003).

CUDSS14.1 Other published redshift estimates are $2.01^{+1.10}_{-0.71}$, based on the 1.4-GHz/850-μm spectral index technique; and 2.06 ± 0.31 based on a χ^2 minimization with one template SED (YC02). Both these estimates are in the low-redshift tail of our redshift distribution, which at a 68 per cent significance level places this object at $z = 3.8^{+0.7}_{-0.8}$ (le2).

CUDSS14.18 The inclusion of the 450- and 850-μm fluxes as detections at 2.3 and 2.8σ (instead of upper limits) gives a similar distribution to the one shown in Fig. A2. Our redshift estimate places this object at $z = 0.7^{+1.3}_{-0.2}$ with a 68 per cent confidence level (le2), in good agreement with its true spectroscopic redshift, $z_{\rm spec}$ = 0.66. Other redshift estimates are $1.12^{+0.53}_{-0.45}$, based on the 1.4-GHz/850-μm spectral index technique; and 1.11 ± 0.21 based on a χ^2 minimization with one template SED (YC02).

SMMJ 00266+1708 Other redshift estimates are $3.49^{+2.03}_{-1.23}$ based on the 1.4-GHz/850-μm spectral index technique; and 3.50 ± 0.45 based on a χ^2 minimization with one template SED (YC02). Our estimate $z = 2.7^{+2.3}_{-0.2}$ (le2) is consistent with these measurements. The redshift distribution is bimodal, because of the range of SEDs used in the redshift estimation technique.

SMMJ 02399−0136 The complete SED reported in Frayer et al. (2000) and Ivison et al. (1998) is inconsistent with the SEDs of our template library at any redshift. This is reported to be an AGN (Smail et al. 1999). One possible explanation for the failure to detect SMMJ 02399−0136 at 3.4 cm is a high-frequency break (between 5.5 and 0.9 cm) in the synchrotron spectrum. Such sharp spectral features are not taken into account in the fitting of the radio spectrum. We note however that excluding the 3.4-cm upper limit from the modelling of the multiwavelength data provides a redshift estimate $z = 2.8^{+1.3}_{-0.3}$ (le2) that is in good agreement with the true redshift of SMMJ 02399−0136: $z = 2.80$. Other redshift estimates are $1.65^{+0.80}_{-0.53}$ based on the 1.4-GHz/850-μm spectral index technique; and 2.83 ± 0.38 based on a χ^2 minimization with one template SED (YC02).

SMMJ 09429+4658 (H5) Other redshift estimates are ⩾3.6 based on the 1.4-GHz/850-μm spectral index technique; and 3.86 ± 0.49 based on a χ^2 minimization with one template SED (YC02). Our estimates actually place this source at a slightly lower redshift $z = 2.4^{+1.5}_{-0.4}$ (le2). Given the sub-mm detection, the low flux density at 1.4 GHz excludes almost all of the template SEDs in our library.

SMMJ 14009+0252 Other redshift estimates are $1.27^{+1.59}_{-0.54}$ based on the 1.4-GHz/850-μm spectral index technique; and 1.30 ± 0.23

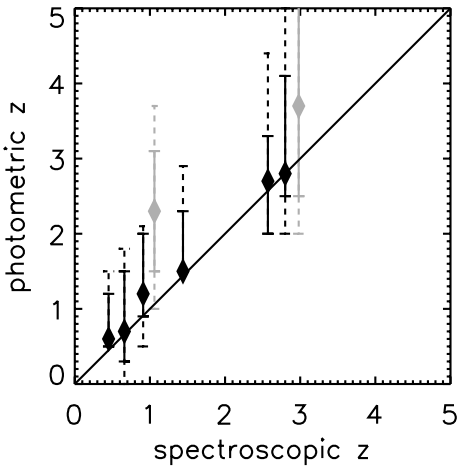

Figure 8. Comparison of the photometric redshift estimates and the true redshifts of sub-mm sources with published optical/IR spectroscopy. The diamonds represent the modes of the redshift distributions for le2. The solid and dashed error bars represent 68 per cent and 90 per cent confidence intervals, respectively. Sources represented in black (in increasing redshift: N1-40, CUDSS14.18, N1-64, HR10, SMMJ 14011+0252 and SMMJ 02399−0136) have photometric redshifts derived from a combination of colours, and are the most precise. Sources represented in grey (in increasing redshift: SMMJ 02399−0134 and W-MM11) have photometric redshifts derived from only one colour (or limit), and have shallow probability distributions, still compatible with their spectroscopic redshifts. Note that the asymmetry of the error bars is a reflection of the asymmetry of the redshift probability distributions, which in cases (CUDSS14.18 and HR10) are significantly skewed.

based on a χ^2 minimization with one template SED (YC02). However, large discrepancies ($\sim 3\sigma$) exist between the template SED of YC02 and the observed 450-μm and 1.4-GHz fluxes, suggesting the fit will have a high reduced χ^2, and that their errors (inferred for good matches) might be underestimated. The flattening of the spectrum at 450 μm, relative to the Rayleigh–Jeans tail defined by the 850-μm and 1.35-mm fluxes, supports a higher redshift estimate. Our own fit indicates that this object has a redshift $z \sim 4.1 \pm 0.8$ (le2). The discrepancies between different redshift estimators might be attributed to the possible AGN nature of this object (Ivison et al. 2000).

SMMJ 14011+0252 Other redshift estimates are $2.53^{+1.24}_{-0.82}$ based on the 1.4-GHz/850-μm spectral index technique; and 2.73 ± 0.37 based on a χ^2 minimization with one template SED (YC02). Our own estimate is $z = 2.7^{+0.6}_{-0.7}$ (le2), in good agreement with these estimates, and with the spectroscopic redshift of the optical counterpart $z_{\rm spec} = 2.57$.

HR10 Other redshift estimates are $1.49^{+0.75}_{-0.53}$ based on the 1.4-GHz/850-μm spectral index technique; and 1.75 ± 0.28 based on a χ^2 minimization with one template SED (YC02). Our own estimate $z = 1.5^{+0.9}_{-0.0}$ (le2) is in good agreement with their measurements, and with the true spectroscopic redshift of this source $z_{\rm spec} = 1.44$.

SMMJ 02399−0134 Other redshift estimates are $1.17^{+0.53}_{-0.45}$ based on the 1.4-GHz/850-μm spectral index technique; and 0.93 ± 0.19 based on a χ^2 minimization with one template SED (YC02). The spectroscopic redshift of this source ($z_{\rm spec} = 1.06$) is inconsistent with our best estimate of the redshift, which within a 68 per cent confidence interval places it at $z = 2.3 \pm 0.8$ (le2). Redshifts in the range $1.0 \leqslant z \leqslant 1.5$ have a 10 per cent integrated probability.

SMMJ 16403+46437 The detection at 1.4 GHz (593 μJy) is high when compared with the 850 μm level, and there is no acceptable correspondence with any of the SEDs in our template library. This, plausibly, might be a misidentification or a radio-quiet AGN, with enhanced radio luminosity compared to the rest-frame FIR luminosity.

SMMJ 16403+46440 Treating the 1.35-mm observation as a detection (2.2σ) provides no additional constraint and gives a similar redshift distribution to the one derived from the 450-μm/850-μm colour and the 1.4-GHz and 1.35-mm upper limits, shown in Fig. A2.

3.3 Cumulative redshift distribution of the submillimetre galaxy population

It is straightforward to calculate the cumulative redshift distribution for the sub-mm galaxy population as the co-addition of the individual probability distributions. It should be noted that the calculation carried out in this paper has the advantage of including the whole redshift probability distribution of each individual galaxy, and not just the mean values of the distributions. We have included in this calculation of the cumulative distribution only those sub-mm sources identified in wide-area blank-field surveys (UK 8-mJy survey and the CUDSS) at a $\geqslant 3.5\sigma$ level: 50 sources. We do not include sub-mm galaxies identified in surveys carried out towards lensing clusters, or targeted observations of other populations of galaxies (radio, *ISO*, Lyman-break galaxies or extremely red objects), or catalogues that have not been fully published (MAMBO surveys), since they can distort and bias the characteristic redshift distribution of the sub-mm galaxy population.

Half of the sources in complete flux-limited sub-mm samples, such as the UK 8-mJy and CUDSS surveys, have a single 850-μm detection with one, or more, additional upper limits at other wavelengths: 28/50 sources detected ($>3.5\sigma$) at 850 μm belong to this category. Since the redshift distributions of these sources are the most dependent on the priors used, the interpretation of the combined redshift distributions should be based on the range of results given by the different evolutionary models.

Fig. 9 shows the cumulative distribution and the combined redshift distribution of the 14 galaxies in the UK 8-mJy survey with redshift distributions derived from SEDs which contain at least two-band detections (objects in Tables 1 and 2). This figure indicates that 65–90 per cent of the sub-mm galaxies could have redshifts in the range $2 \lesssim z \lesssim 4$. The results are consistent with the expectation that sub-mm galaxies detected in the SCUBA (and also MAMBO) surveys represent a high-z population (Dunlop 2001; Blain et al. 2002).

The sources in the CUDSS sample with one or more measured colours (nine sources) appear to have a significantly different lower-redshift distribution, with 40 per cent of the galaxies at $z \lesssim 2$ and approximately 50 per cent of the galaxies at $2 \lesssim z \lesssim 4$. The high-redshift tail of the CUDSS sample is similar to that shown by the 8-mJy survey with $\sim$10 per cent probability at $z > 4$. The two galaxies responsible for the low-redshift difference are CUDSS3.1 and 3.9, both with relatively high 450-μm flux densities $S_{450\,\mu{\rm m}} \geqslant 77$ mJy, compared with the 30–40 mJy detection levels for the UK 8-mJy survey sources. Taking the data for the CUDSS sample at face value suggests that it includes an overdensity of low-z galaxies at $z \lesssim 2$, compared to the galaxies in the UK 8-mJy survey, and vice versa. This discrepancy, however, could also be explained by

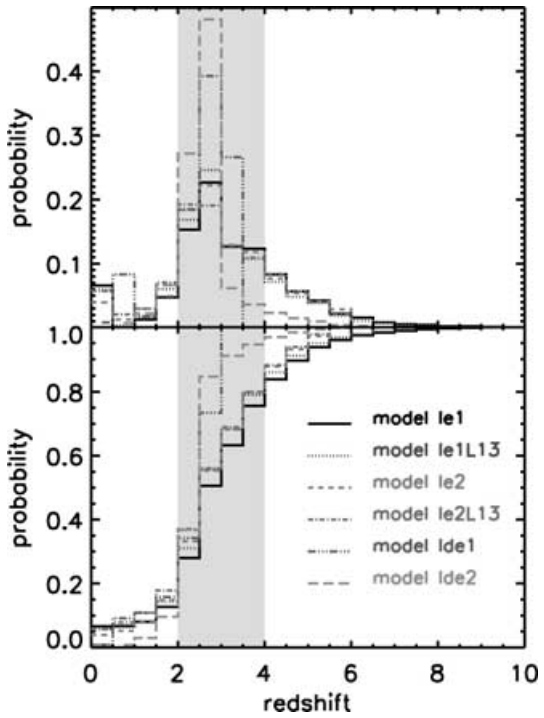

Figure 9. Combined redshift distribution for the population of sub-mm galaxies in the 8-mJy SCUBA survey with one or more measured colours (the 14 galaxies contained in Tables 1 and 2). The different lines represent different evolutionary models assumed for the sub-mm galaxy population (Section 2). *Upper panel:* Discrete bin probabilities. *Lower panel:* Cumulative distribution. This figure is available in colour in the online version of the journal on *Synergy*.

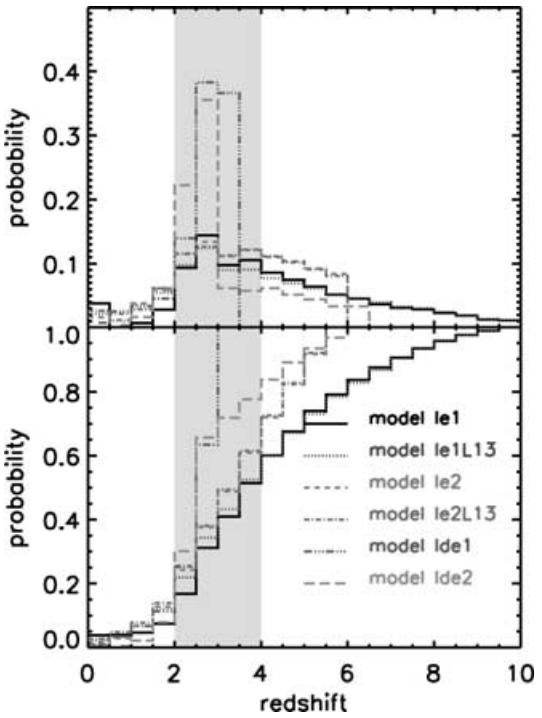

Figure 10. Combined redshift distribution for the population of all 50 sub-mm galaxies detected in wide-area surveys at 850 μm ($>3.5\sigma$) and listed in Tables 1, 2 and 3. The different lines represent different evolutionary models assumed for the sub-mm galaxy population (see text). Beware that the extended tail towards high redshifts is due to sources that are just detected at 850 μm. The upper limits at other wavelengths do not usually help to constrain their redshifts between $2 \leqslant z \leqslant 10$, and hence their probability distributions are very flat in those regimes. *Upper panel:* Discrete bin probabilities. *Lower panel:* Cumulative distribution. This figure is available in colour in the online version of the journal on *Synergy*.

a difference in the flux calibration of the 450-μm data in the two surveys.

Fig. 10 shows the cumulative redshift distributions of the sub-mm galaxy population for the 50 galaxies in the 8-mJy and CUDSS surveys detected at a $\geqslant 3.5\sigma$ level. This extended sample includes the 27 sub-mm galaxies with a single detection at 850 μm and one, or more, upper limits at other wavelengths (Table 3). The combined redshift distributions, for the different evolutionary models under consideration, imply that the majority of the sub-mm galaxies, approximately 50–90 per cent, lie between $z = 2$ and 4. The remainder of the galaxies, ∼10 per cent, lie at $z < 2$. Fig. 10 also shows that $\lesssim$50 per cent of the galaxies have colours that are consistent with $z > 4$. The distribution of the high-redshift tail is very sensitive to the choice of evolutionary model, since the individual redshift distributions for the 27 sources with only a single detection are necessarily very flat over the redshift range $z \gtrsim 2$ (see Fig. A3). For these galaxies, the constraint on their redshift distributions comes mainly from the flux detected at 850 μm and the ability to reproduce it with the evolution of the 60-μm local luminosity function. More extensive photometry, especially including shorter sub-mm wavelengths, is crucial to better constrain these flat distributions, as illustrated by Fig. 7 (see also fig. 6 in Paper I).

4 THE LIKELIHOOD OF MISIDENTIFYING THE RADIO COUNTERPARTS OF HIGH-REDSHIFT SUBMILLIMETRE GALAXIES

The strength of the correlation between the FIR and radio luminosities in starburst galaxies (Helou, Soifer & Rowan-Robinson 1985; Condon 1992) has supported the expectation that *all* high-z star-forming sub-mm galaxies should also have a detectable radio counterpart, provided the radio observations are deep enough.

Although originally encouraged by this assumption, some of the deepest VLA searches for radio emission associated with SCUBA and MAMBO sources have met with varying degrees of success.

The deep VLA surveys of the Lockman Hole and ELAIS N2 fields (Ivison et al. 2002) have a 1σ noise limit $\geqslant$5–9 μJy at 1.4 GHz. These surveys have identified 11/16 and 8/14 sub-mm sources at 1.4 GHz, respectively, with peak radio fluxes above 4σ and integrated fluxes above 3σ, after rejecting five and one sub-mm sources from the parent samples, respectively, because of their high sub-mm noise levels. From these, there are 9/16 and 5/14 sources in the Lockman Hole and ELAIS N2 surveys, respectively, with a final S/N > 3 when one considers the additional errors due to calibration and fitting a Gaussian to the peak of the radio emission. If one limits the analysis to sources $\geqslant$8 mJy at 850 μm, then 4/10 and 4/8 sources have been simultaneously detected with S/N > 3 at 850 μm and 1.4 GHz. This is in clear contrast to the claims of previous authors (Fox et al. 2002) that bright sub-mm sources (>8 mJy at 850 μm) should be detected at flux densities of ∼100 μJy at 1.4 GHz.

In order to understand the properties of the radio associations, we have calculated the probability of detection at 1.4 GHz for a mock 8-mJy survey, following the same methodology as in Paper I, but using the extended library of SEDs (Section 2). The intrinsic 850-μm fluxes of the galaxies are convolved with $1\sigma \sim 2.6$ mJy

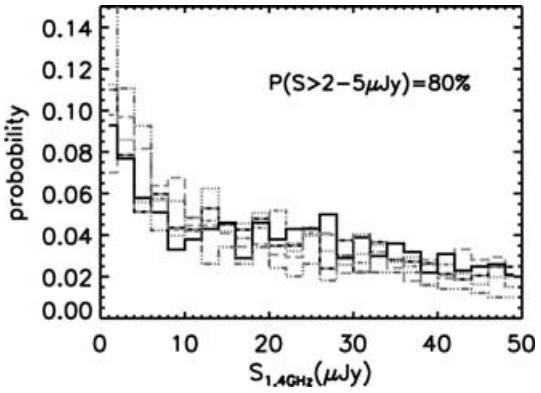

Figure 11. Distribution of intrinsic fluxes at 1.4 GHz corresponding to a population of galaxies discovered at 850 μm, at a level $\geqslant$8 mJy. Depending on the evolutionary model adopted, 80 per cent of the sources would have a flux in excess of 2–5 Jy, and hence, in order to conduct a parallel 1.4-GHz imaging follow-up programme with 80 per cent completeness, the 1σ depth of the images should be 1–2 Jy. This figure is available in colour in the online version of the journal on *Synergy*.

measurement errors, and 9 per cent calibration uncertainty. Fig. 11 shows the distribution of intrinsic 1.4-GHz fluxes for the detected sources (including errors) above the 8-mJy threshold at 850 μm.

We conclude that future surveys at 1.4 GHz must reach a 3σ sensitivity of 2–5 μJy if radio observations are to provide counterparts to 80 per cent of the high-z sub-mm galaxies with 850-μm flux densities $\geqslant$8 mJy, according to the redshift distributions assumed in the alternative evolutionary models. Thus, current radio observations have insufficient sensitivity to detect the bulk of the sub-mm population with adequate S/N, and we must wait for the next generation of new and upgraded facilities (e.g. e-VLA, e-MERLIN, SKA).

In the case of the UK 8-mJy survey, Fig. 10 shows that 40–50 per cent (Lockman Hole) and 50–60 per cent (ELAIS N2) of the sources should have an intrinsic 1.4-GHz flux lower than the 3σ threshold, in the absence of any radio-loud AGN emission. These levels agree well with the number of radio counterparts to $\geqslant$8-mJy sources (Scott et al. 2002; Ivison et al. 2002), bearing in mind the actual variation in sensitivity across the SCUBA wide-area survey fields.

This potential for misidentifying the correct radio sources associated with blank-field sub-mm galaxies will inevitably lead to incorrect estimates of photometric redshifts if they are derived in part from the 1.4-GHz fluxes. In the calculation of the cumulative redshift distribution (Section 3.3) we have treated all of the published associations of 1.4-GHz and 850-μm sources as the correct radio counterparts to the sub-mm galaxies.

Despite the rapid acceptance of the radio–sub-mm flux density ratio, $\alpha_{345}^{1.4}$ (CY99, CY00), as the preferred method with which to estimate the redshift distribution of the sub-mm galaxy population, this diagnostic ratio loses its power to discriminate between photometric redshifts at $z > 2$ (CY99, CY00). We have already demonstrated in Paper I (fig. 11) the detrimental effect of the large dispersion in radio–sub-mm colours of the local template galaxies on the accuracy of the derived photometric redshifts of the sub-mm blank field sources. Furthermore, the existing radio interferometers will remain limited in their ability to map the large areas $\sim$1–40 deg^2 that will be surveyed by the next generation of sub-mm and FIR experiments (e.g. BLAST, *Herschel*, *SIRTF*) down to the necessary sensitivity levels (3$\sigma \sim$ 2–5 μJy at 1.4 GHz), making the use of $\alpha_{1.4}^{345}$ an impracticable measure of redshift for the majority of the population. Deep interferometric radio observations, however, remain a practicable way to pinpoint the source of the sub-mm emission with sufficient positional accuracy to investigate galaxy morphologies and exploit optical/IR spectroscopic line diagnostics.

This limitation of the radio–sub-mm technique prompted the design and construction of the Balloon-borne Large Aperture Submillimetre Telescope (BLAST) (Devlin et al. 2001). The primary scientific goal of BLAST is to break the current 'redshift deadlock' by providing photometric redshifts with sufficient accuracy, without the prior necessity for secure optical, IR or radio counterparts. BLAST will use rest-frame sub-mm and FIR colours to derive redshifts with an accuracy $\Delta z \sim \pm 0.5$ for $>$1000 galaxies in the redshift range $0 < z < 6$ detected in wide-area ($>$0.5–10 deg^2) surveys at 250, 350 and 500 μm (Hughes et al. 2002).

This redshift accuracy is sufficient to guide the choice of possible front-end spectrographs, and their receiver tunings, on large single-dish ground-based mm and cm telescopes [e.g. the 100-m Green Bank Telescope (GBT) and the 50-m Large Millimetre Telescope (LMT)] in the effort to detect redshifted CO emission lines. We conclude this paper with the description of one application of this technique.

5 BROAD-BAND MILLIMETRE–CENTIMETRE SPECTROSCOPY

Until recently the brightest sub-mm source in the *Hubble Deep Field*, HDF850.1 (Hughes et al. 1998), has avoided the detection of its X-ray, optical, IR or radio counterpart, despite an accurate interferometric position at 236 GHz (Downes et al. 1999) and the unprecedented depth of the multiwavelength HDF surveys (Williams et al. 1996; Thompson et al. 1999; Richards 1999; Hornschemeier et al. 2000). It is only after the accurate subtraction of the elliptical galaxy, 3-586, at $z \sim 1$, however, that a faint lensed IR counterpart ($K = 23.5$, $H - K = 1.5$, $I - K > 5.1$) to HDF850.1 has been discovered (Dunlop et al. 2003).

This IR detection now gives greater confidence to the likelihood that the coincident radio emission, with a flux density of 16 ± 4 μJy at 1.4 GHz, from the combined data of MERLIN and the VLA, is genuinely associated with the sub-mm source (Dunlop et al. 2003). Furthermore, this strengthens the suggestion that a marginal 3.3σ detection at 8.4 GHz (VLA 3651+1226; Richards, private communication) that may also be associated with HDF850.1.

The redshift probability distribution for HDF850.1, based on the multiwavelength 170-μm–1.4-GHz data, indicates that z is between 3.3 and 5.4 with an 86 to 90 per cent confidence depending on the adopted prior (Fig. 12). This high photometric redshift supports the earlier decision to reject the $z \sim 1$ elliptical galaxy 3-586, as the optical counterpart. Unfortunately the IR counterpart, HDF850.1K, is too faint to attempt IR spectroscopy with even the 10-m class of telescopes.

The most efficient means to determine the spectroscopic redshifts of optically obscured sub-mm galaxies is the detection of millimetre and centimetre wavelength molecular lines using large single-dish telescopes (e.g. GBT or LMT) with broad-band receivers (Townsend et al. 2001; Carilli & Blain 2002). In this way, it is possible to eliminate the necessity for an optical/IR counterpart, or a position accurate to $<$3 arcsec. Given the predicted accuracy of the photometric redshift for HDF850.1, and taking all of the uncertainties discussed in Section 2 into account, we demonstrate in Fig. 12 that the $J = 1$–0 CO line in HDF850.1 has an 86–90 per cent probability of detection in the K-band receiver (18.0–26.5 GHz) on the GBT. Observations to conduct searches for CO emission in high-z sub-mm galaxies,

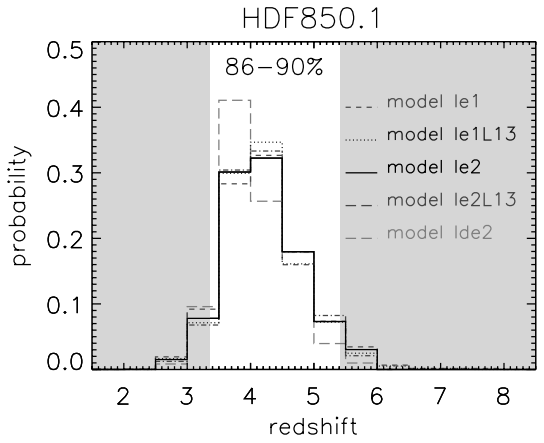

Figure 12. Redshift probability distributions for HDF850.1. The different line types and colours correspond to the different evolutionary models considered. Model led1 is not plotted, since it excludes sources at $z > 3.5$ due to the strong prior decline of the density and luminosity of sources. The unshaded area corresponds to the redshift range where the ^{12}CO ($J = 1$–0) line lies in the observable K-band window (18.5–26.0 GHz), accessible with the 100-m GBT. There is an 86–90 per cent probability of detecting the $J = 1$–0 CO line in this GBT window. This figure is available in colour in the online version of the journal on *Synergy*.

guided only by their photometric redshifts, are currently under way on the GBT.

6 CONCLUSIONS

We have derived meaningful photometric redshift probability distributions for individual sub-mm galaxies using Monte Carlo simulations that take into account a range of measurement errors and model-dependent uncertainties. From the individual redshift probability distributions, we have measured the cumulative redshift distribution for the sub-mm population of galaxies identified in blank-field surveys. We find that the multiwavelength FIR–radio data for 50 sub-mm galaxies detected ($>3.5\sigma$) at 850 μm are consistent with ∼50–90 per cent of the population lying at redshifts $z = 2$–4, with only a small fraction, ∼10 per cent, of the population at $z < 2$. We also show that up to 50 per cent of the galaxies have colours that are consistent with $z > 4$. The possibility that the sub-mm galaxy population contains a significant fraction undergoing a major burst of star formation at such early epochs has important consequences for models of galaxy formation. This suggestion is still highly dependent on the prior assumption of the evolutionary model for the sub-mm population which affects most strongly those sub-mm sources detected only at 850 μm.

Shorter-wavelength sub-mm data (250–500 μm) from a future balloon-borne experiment, BLAST, will provide powerful additional constraints ($\Delta z \sim \pm 0.5$) on the redshift distribution of all the SCUBA and MAMBO galaxies at $z > 2$. A photometric redshift accuracy of ± 0.5 for an individual galaxy will be sufficient to provide robust statistical measurements of the redshift distribution of the entire population, the global history of dust-obscured star formation and the clustering properties of sub-mm galaxies.

We have argued that the large dispersion in the radio to sub-mm SEDs (or 850-μm/1.4-GHz colour) of the template galaxies naturally translates into an imprecise measure of the photometric redshift, and that radio observations cannot be used efficiently to measure the individual redshifts of thousands of galaxies detected in future wide-area sub-mm surveys. The sub-mm/radio spectral index is still able to discriminate between the $z < 2$ and $z > 2$ regime.

We have an on-going programme to conduct centimetre wavelength observations of CO $J = 1$–0 molecular line transitions in high-z sub-mm galaxies on the 100-m GBT. The observations, however, first require an accurate photometric redshift probability distribution to guide the choice of receiver and tuning parameters. We illustrate the power of our photometric redshift technique with the example of HDF850.1, one of the best-studied sub-mm galaxies (Hughes et al. 1998; Downes et al. 1999; Dunlop et al. 2003).

Within the next few years, the combination of ground-based, balloon-borne and satellite experiments will provide accurately calibrated rest-frame sub-mm–FIR data for a significant population of sub-mm galaxies. The centimetre and millimetre wavelength spectroscopic redshift confirmation of their photometric redshifts will calibrate the method outlined in this paper. Thus we can finally look forward to breaking the 'redshift deadlock' that currently prevents an accurate understanding of the nature of the sub-mm galaxy population and their evolutionary history.

ACKNOWLEDGMENTS

This work has been partly supported by CONACYT grants 32180-E and 32143-E. We thank the anonymous referee for critical comments on and careful reading of the manuscript.

REFERENCES

Barger A. J., Cowie L. L., Richards E. A., 2000, AJ, 119, 2092
Bertoldi F. et al., 2000, A&A, 360, 92
Blain A. W., Smail I., Ivison R., Kneib J.-P., Frayer D. T., 2002, Phys. Rep., 369, 111
Borys C., Chapman S. C., Halpern M., Scott D., 2002, MNRAS, 330, 63
Carilli C. L., Blain A. W., 2002, ApJ, 569, 605
Carilli C. L., Yun M. S., 1999, ApJ, 513, L13 (CY99)
Carilli C. L., Yun M. S., 2000, ApJ, 530, 618 (CY00)
Chapman S. C. et al., 2000, MNRAS, 319, 318
Chapman S. C., Scott D., Borys C., Fahlman G. G., 2002a, MNRAS, 330, 92
Chapman S. C., Smail I., Ivison R. J., Helou G., Dale D. A., Lagache G., 2002, ApJ, 573, 66
Condon J. J., 1992, ARA&A, 30, 575
Cowie L., Barger A. J., Kneib J., 2002, AJ, 123, 2197
Dannerbauer H., Lehnert M. D., Lutz D., Tacconi L., Bertoldi F., Carilli C., Genzel R., Menten K., 2002, ApJ, 573, 473
Devlin M. et al., 2001, in Lowenthal J., Hughes D. H., eds, Deep Millimetre Surveys, Implications for Galaxy Formation and Evolution. World Scientific, Singapore, p. 59 (astro-ph/0012327)
Dey A., Graham J. R., Ivison R. J., Smail I., Wright G. S., Liu M. C., 1999, ApJ, 519, 610
Downes D. et al., 1999, A&A, 347, 809
Dunlop J. S., 2001, New Astron. Rev., 45, 609
Dunlop J. S. et al., 2003, MNRAS, (astro-ph/0205480)
Dunne L., Eales S. A., Edmunds M., Ivison R., Alexander P., Clements D. L., 2000, MNRAS, 315, 115
Eales S. A., Lilly S., Gear W., Dunne L., Bond J. R., Hammer F., Le Fèvre O., Crampton D., 1999, ApJ, 515, 518
Eales S. A., Lilly S., Webb T., Dunne L., Gear W., Clements D., Yun M., 2000, AJ, 120, 2244
Fardal M. A., Katz N., Weinberg D. H., Davé R., Hernquist L., 2002, ApJ, submitted (astro-ph/0107290)
Fox M. J. et al., 2002, MNRAS, 331, 839
Frayer D. T., Smail I., Ivison R. J., Scoville N. Z., 2000, AJ, 120, 1668

Gear W. K., Lilly S. J., Stevens J. A., Clements D. L., Webb T. M., Eales S. A., Dunne L., 2000, MNRAS, 316, 51
Helou G., Soifer B. T., Rowan-Robinson M., 1985, ApJ, 298, L7
Hornschemeier A. et al., 2000, ApJ, 541, 49
Hughes D. H., Robson E. I., Dunlop J. S., Gear W. K., 1993, MNRAS, 263, 607
Hughes D. H. et al., 1998, Nat, 394, 241
Hughes D. H. et al., 2002, MNRAS, 335, 871 (Paper I)
Ivison R. I., Smail I., Le Borgne J.-F., Blain A. W., Kneib J.-P., Bezecourt J., Kerr T. H., Davies J. K., 1998, MNRAS, 298, 583
Ivison R. J., Smail I., Barger A. J., Kneib J.-P., Blain A. W., Owen F. N., Kerr T. H., Cowie L. L., 2000, MNRAS, 315, 209
Ivison R. J. et al., 2002, MNRAS, 337, 1
Klaas U. et al., 2001, A&A, 379, 823
Lilly S. J. et al., 1999, ApJ, 518, 641
Lutz D. et al., 2001, A&A, 378, 70
Richards E. A., 1999, ApJ, 513, L9
Richards E. A., 2000, ApJ, 533, 611
Richards E. A., Kellerman K. I., Fomalont E. B., Windhorst R. A., Partridge R. B., 1998, ApJ, 116, 1039
Saunders D. B., Rowan-Robinson M., Lawrence A., Efstathiou G., Kaiser N., Ellis R. S., Frenk C. S., 1990, MNRAS, 242, 318
Scott D. et al., 2000, A&A, 357, 5
Scott S. et al., 2002, MNRAS, 331, 817
Smail I., Ivison R. J., Blain A. W., 1997, MNRAS, 490, L5
Smail I., Ivison R. J., Kneib J.-P., Cowie L. L., Blain A. W., Barger A. J., Owen F. N., Morrison G., 1999, MNRAS, 308, 1061
Smail I., Ivison R. J., Blain A. W., Kneib J.-P., 2002, MNRAS, 331, 495
Thompson R. I., Storrie-Lombardi L. J., Weymann R. J., Rieke M. J., Schneider G., Stobie E., Lytle D., 1999, AJ, 117, 17
Townsend R. H. D., Ivison R. J., Smail I., Blain A. W., Frayer D. T., 2001, MNRAS, 328, L17
Webb T. M. et al., 2003, ApJ, 582, 6
Williams R. E. et al., 1996, AJ, 112, 1335
Yun M. S., Carilli C. L., 2002, ApJ, 568, 88 (YC02)

APPENDIX A: REDSHIFT ESTIMATES FOR INDIVIDUAL SUBMILLIMETRE GALAXIES

A catalogue of redshift probability distributions and SEDs for the galaxies detected in more than two bands (Tables 1 and 2) is included (Figs A1 and A2). We also include the corresponding colour–colour–redshift (Fig. A1) or colour–flux–redshift (Fig. A2) plots from which they have been derived. All estimates are derived for model le2.

For galaxies detected in just one band (Table 3), we present a selection of the results derived for six out of the 46 galaxies included in Table 3 (Fig. A3). The general uniformity of their redshift distributions is a fair representation of those galaxies not included in this Appendix.

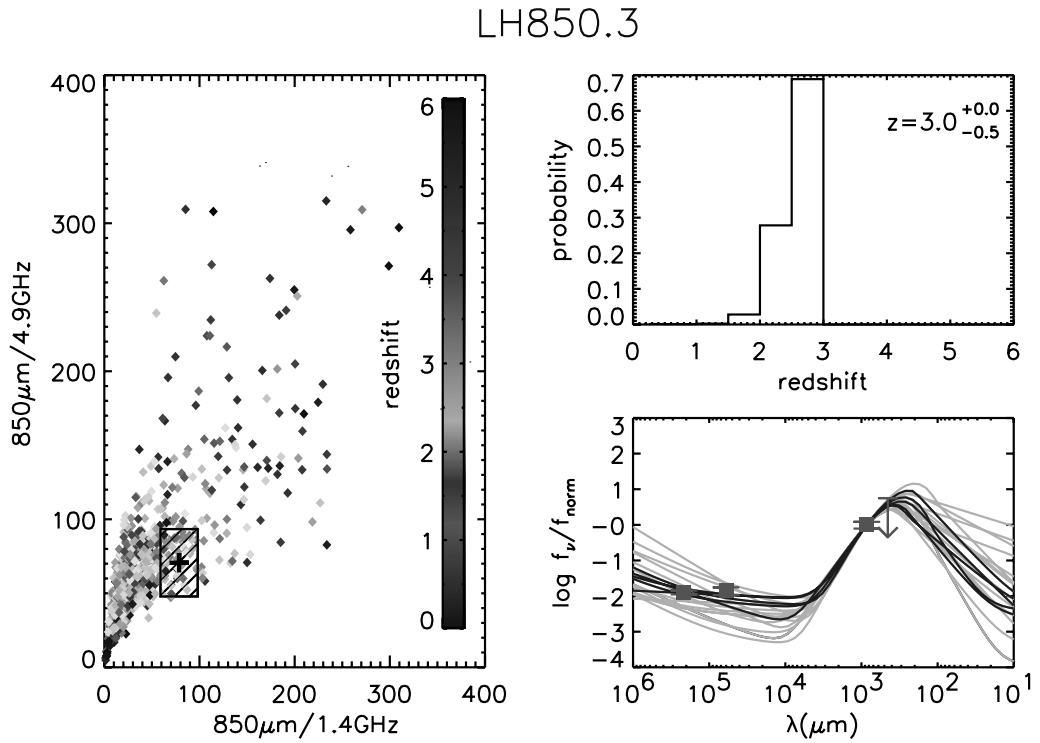

Figure A1. Colour–colour plots, redshift probability distributions and SEDs of all sub-mm sources in our catalogue detected in more than three bands. *Left panels:* Colour–colour plots used for redshift determination. The flux ratios of the mock galaxies in our simulated catalogues are represented as diamonds, and their redshifts are coded in colour (available in the electronic version), according to the scale shown to the right. The cross and dashed box represent the measured colours (and its error box at 1σ) of the sub-mm galaxy considered. *Top right panels:* Redshift probability distributions. Within the panels, the mode of the distribution and the 68 per cent confidence level interval are indicated. *Bottom right panels:* The observed SEDs of the sub-mm galaxies, normalized to one of the observed fluxes are shown as squares and arrows. The template SEDs (lines) are redshifted to the mode of the redshift probability distribution of the sub-mm galaxy. The arrows indicate 3σ upper limits. The squares denote detection at a level $>3\sigma$, with 1σ error bars. The dark lines (blue in the electronic version) represent the template SEDs, which are compatible with the colours of the sub-mm galaxies at a 3σ level. This figure is available in colour in the online version of the journal on *Synergy*.

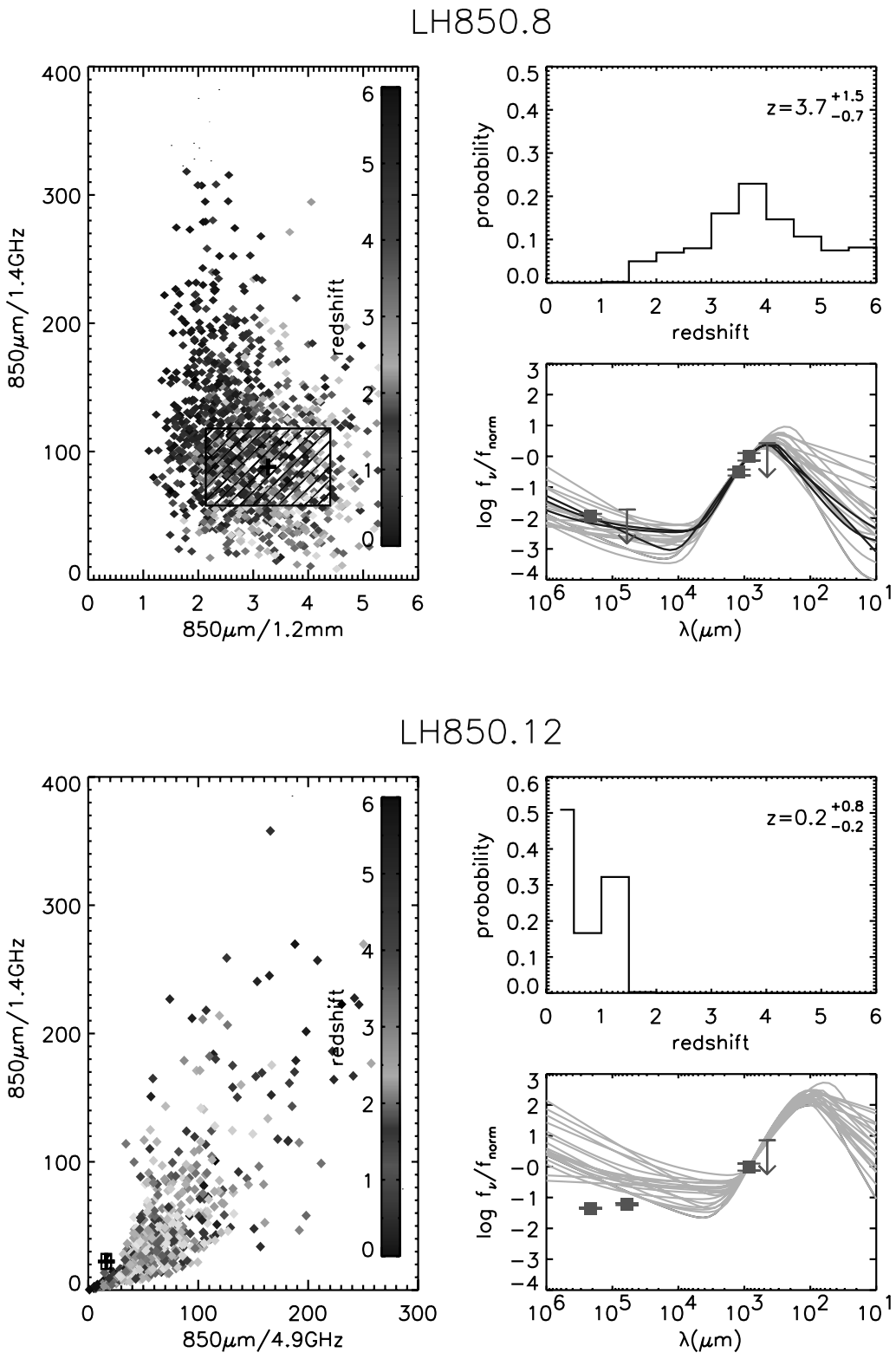

Figure A1 – *continued*

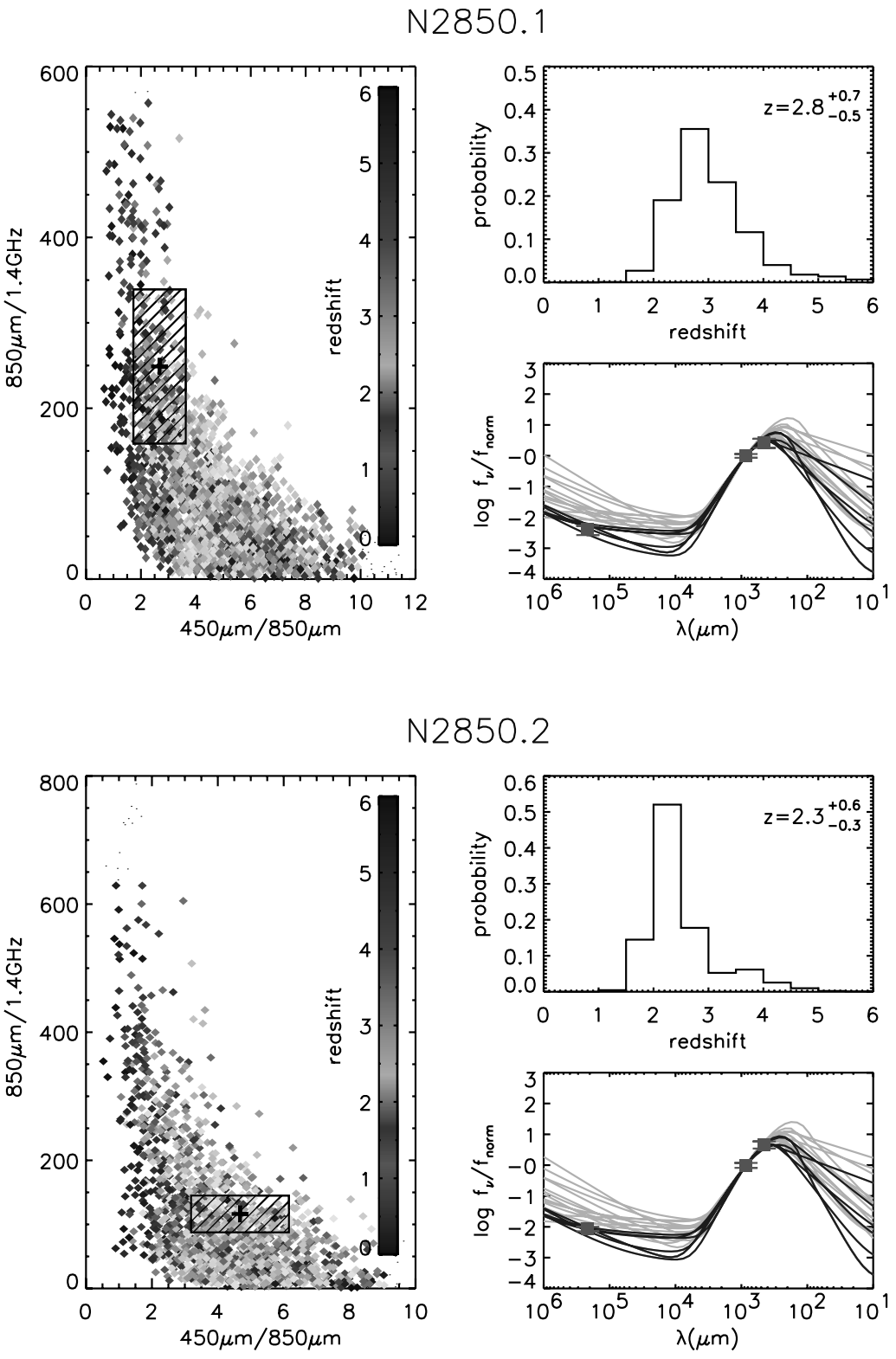

Figure A1 – *continued*

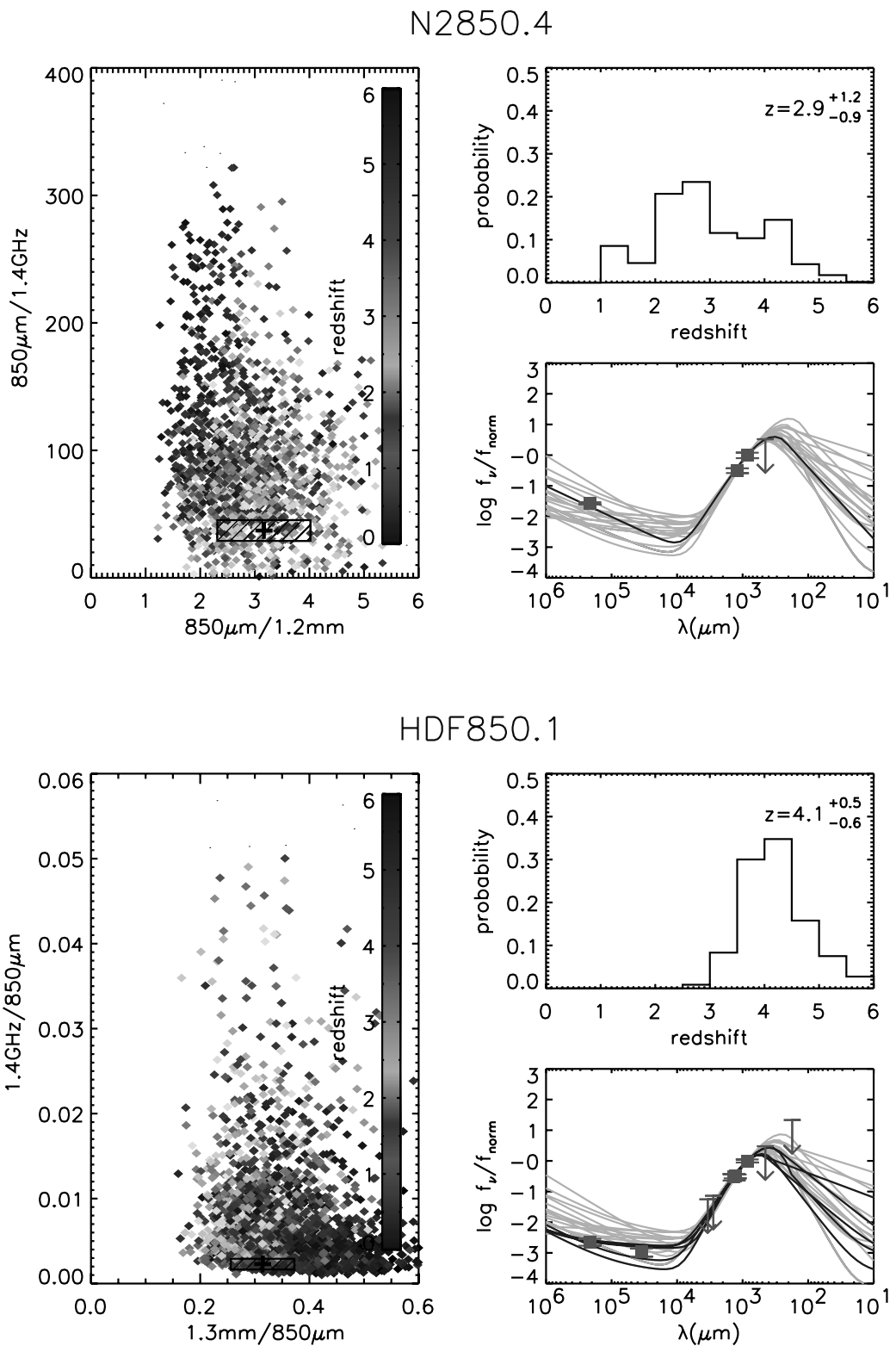

Figure A1 – *continued*

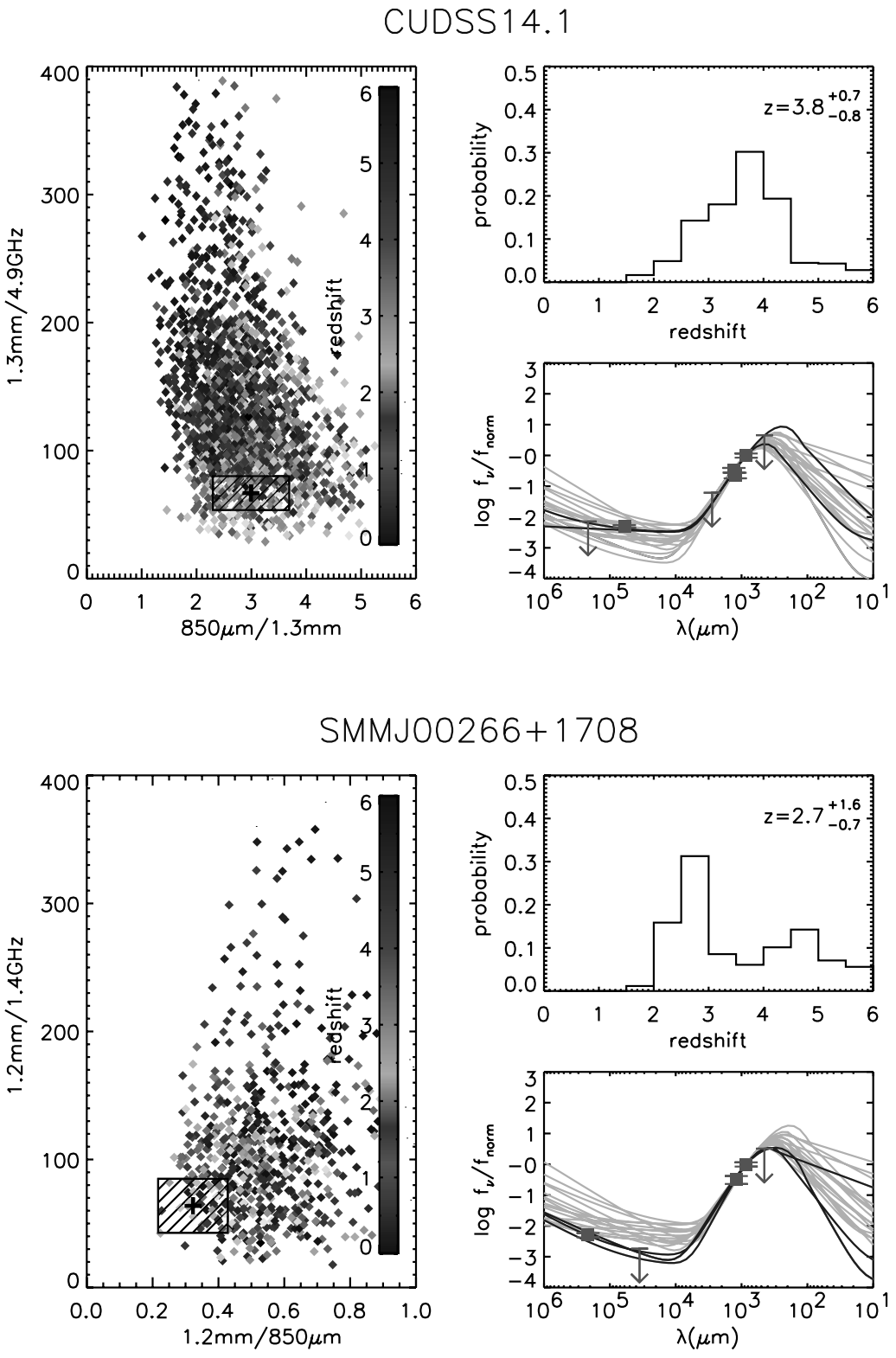

Figure A1 – *continued*

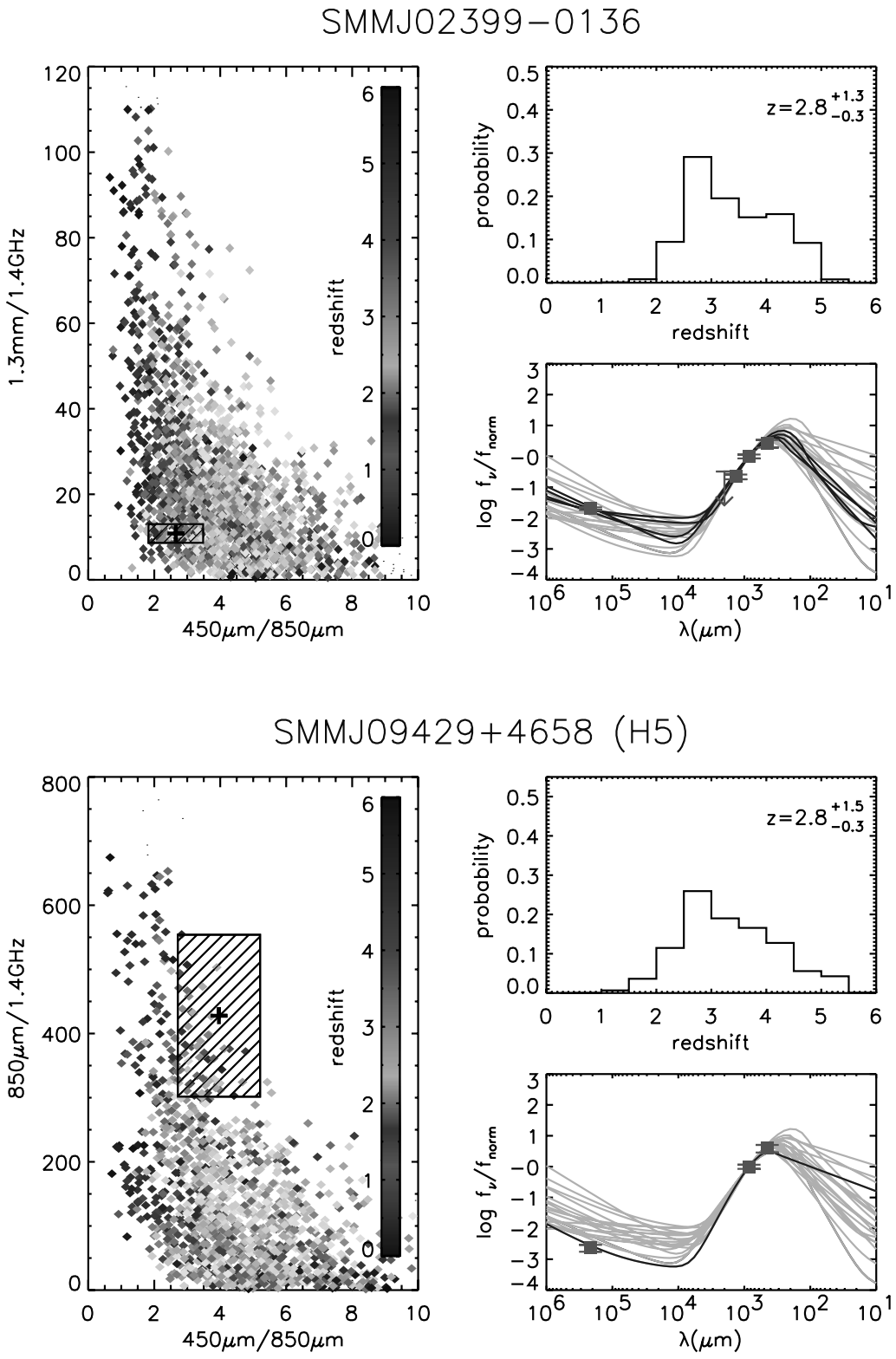

Figure A1 – *continued*

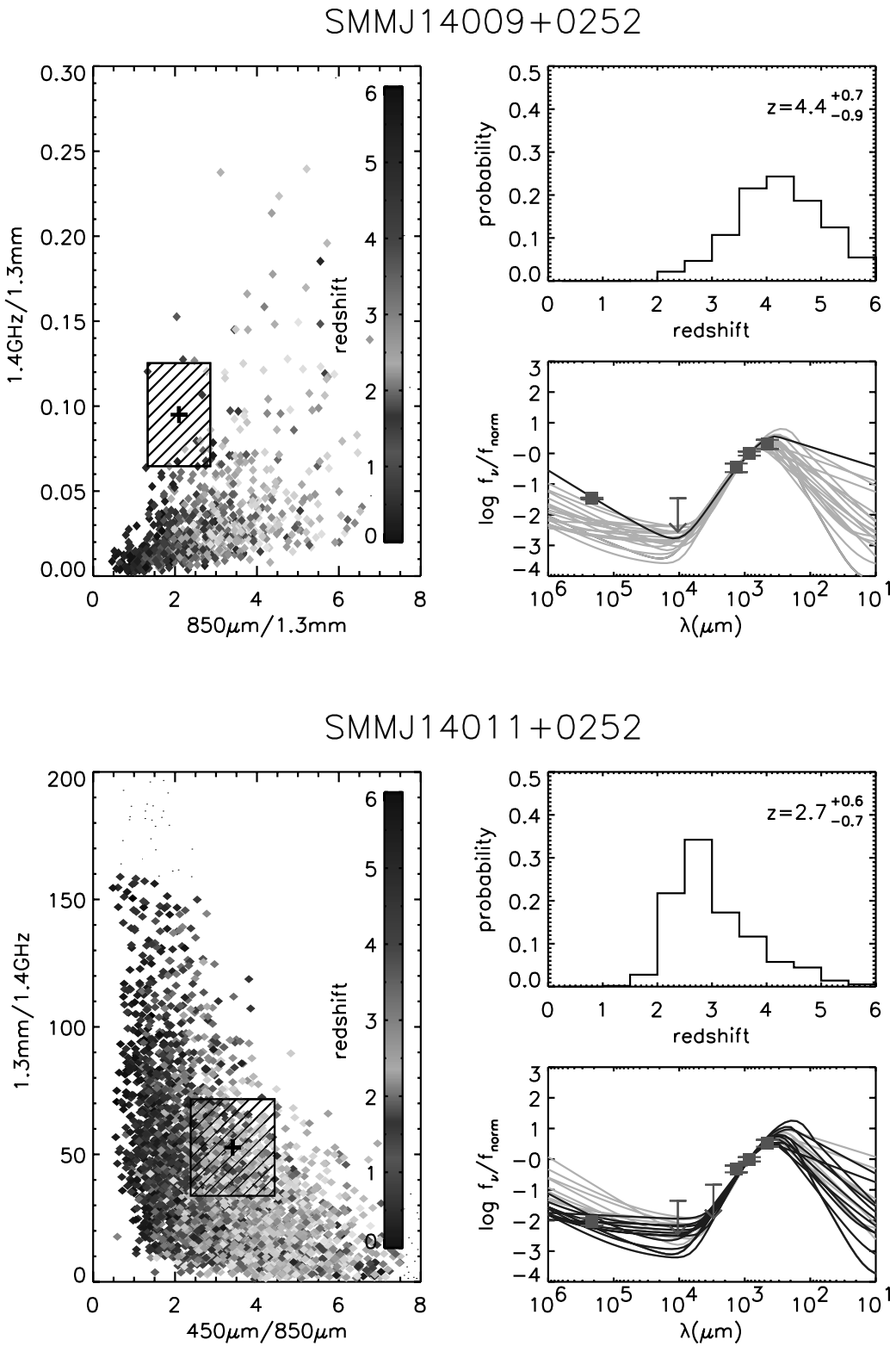

Figure A1 – *continued*

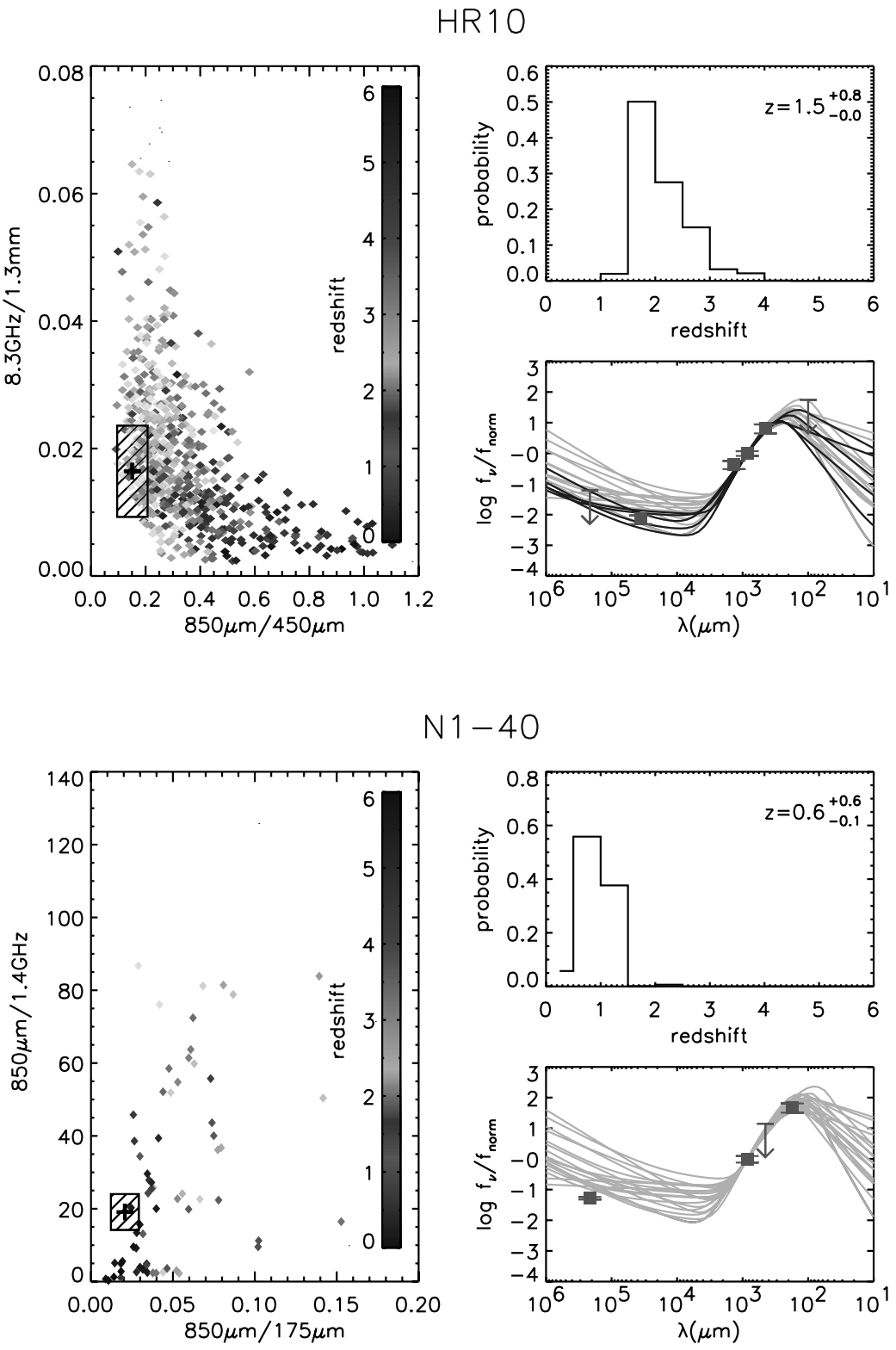

Figure A1 – *continued*

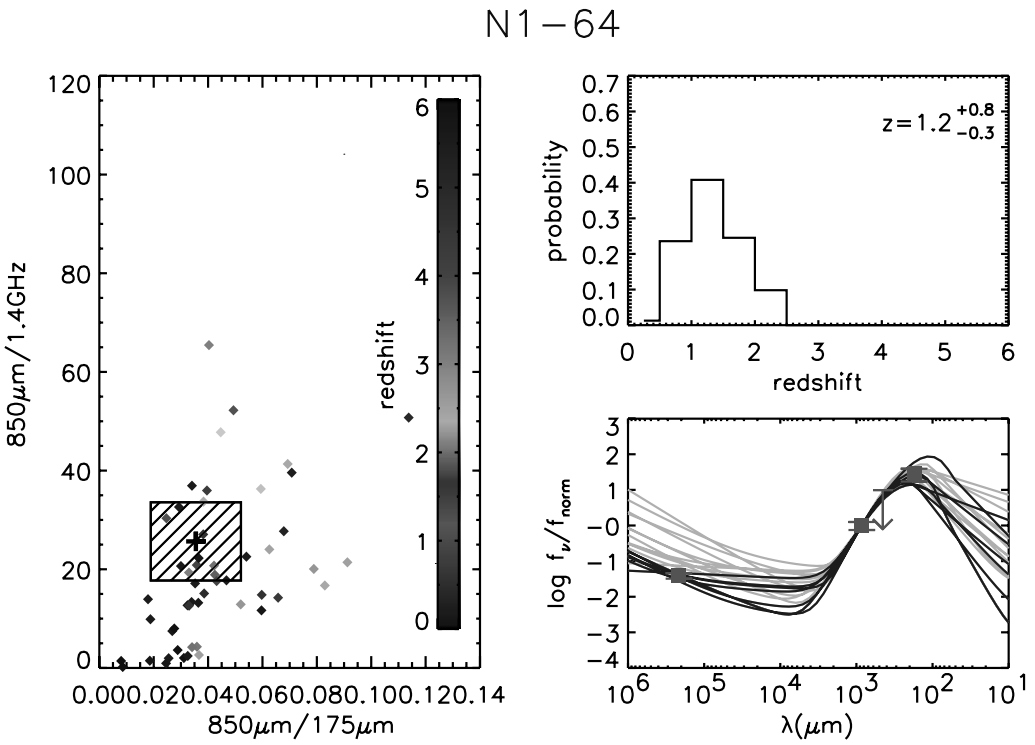

Figure A1 – *continued*

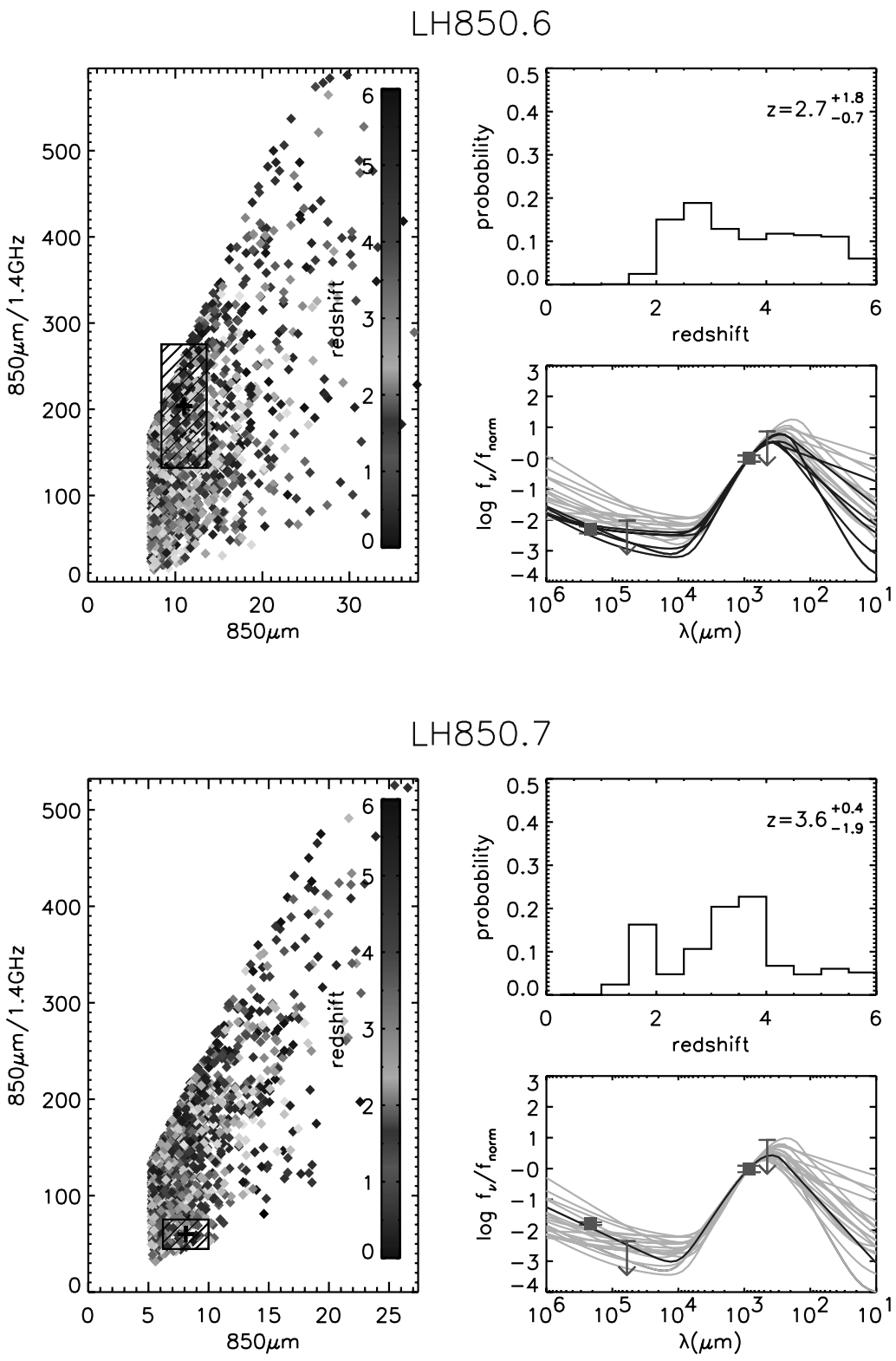

Figure A2. Colour–flux–redshift plots, redshift distributions and the comparison of template SEDs and observed data for sub-mm sources detected in at least two bands at a $>3\sigma$ level. The description of the plots is as in Fig. A1. This figure is available in colour in the online version of the journal on *Synergy*.

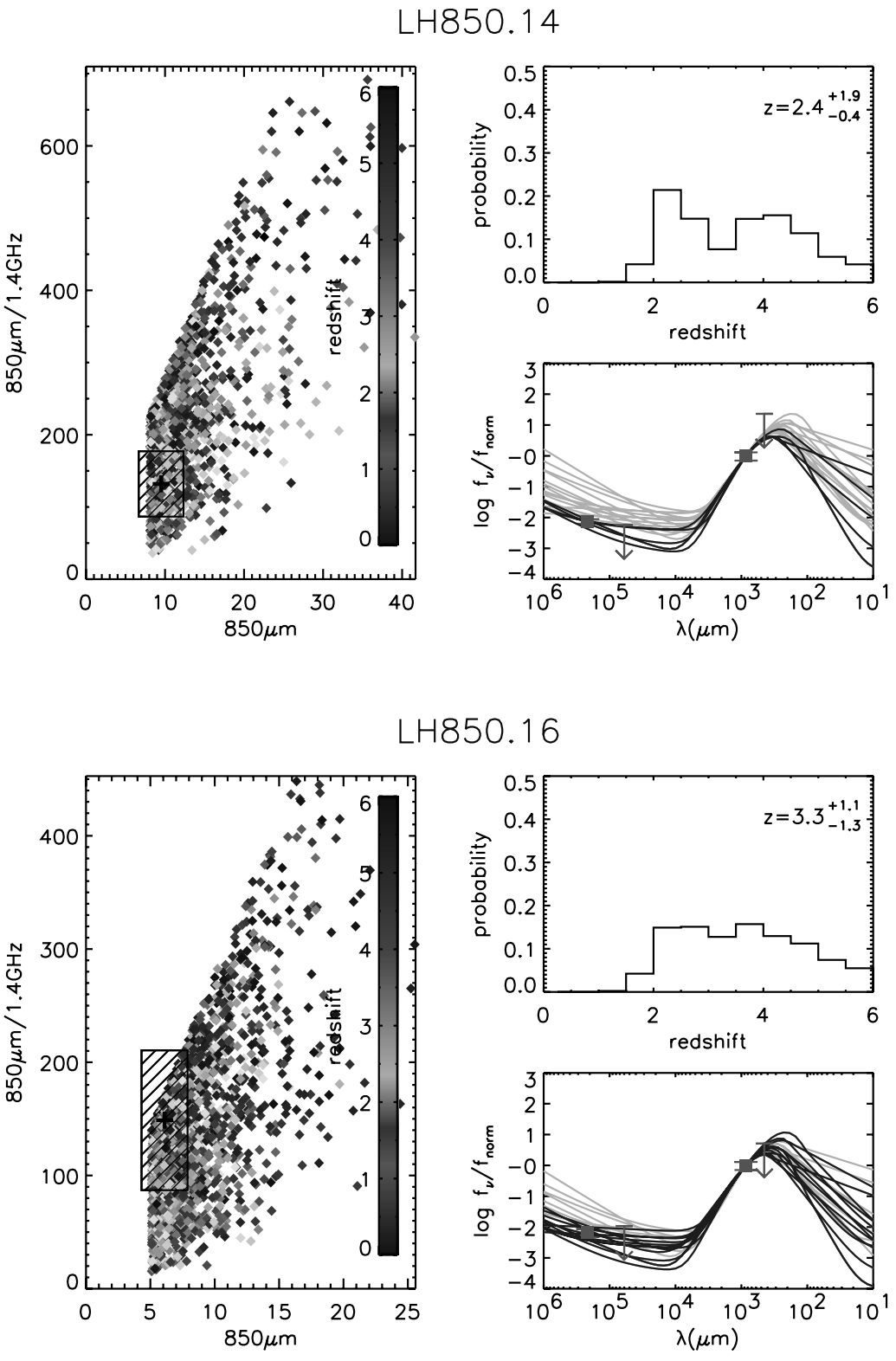

Figure A2 – *continued*

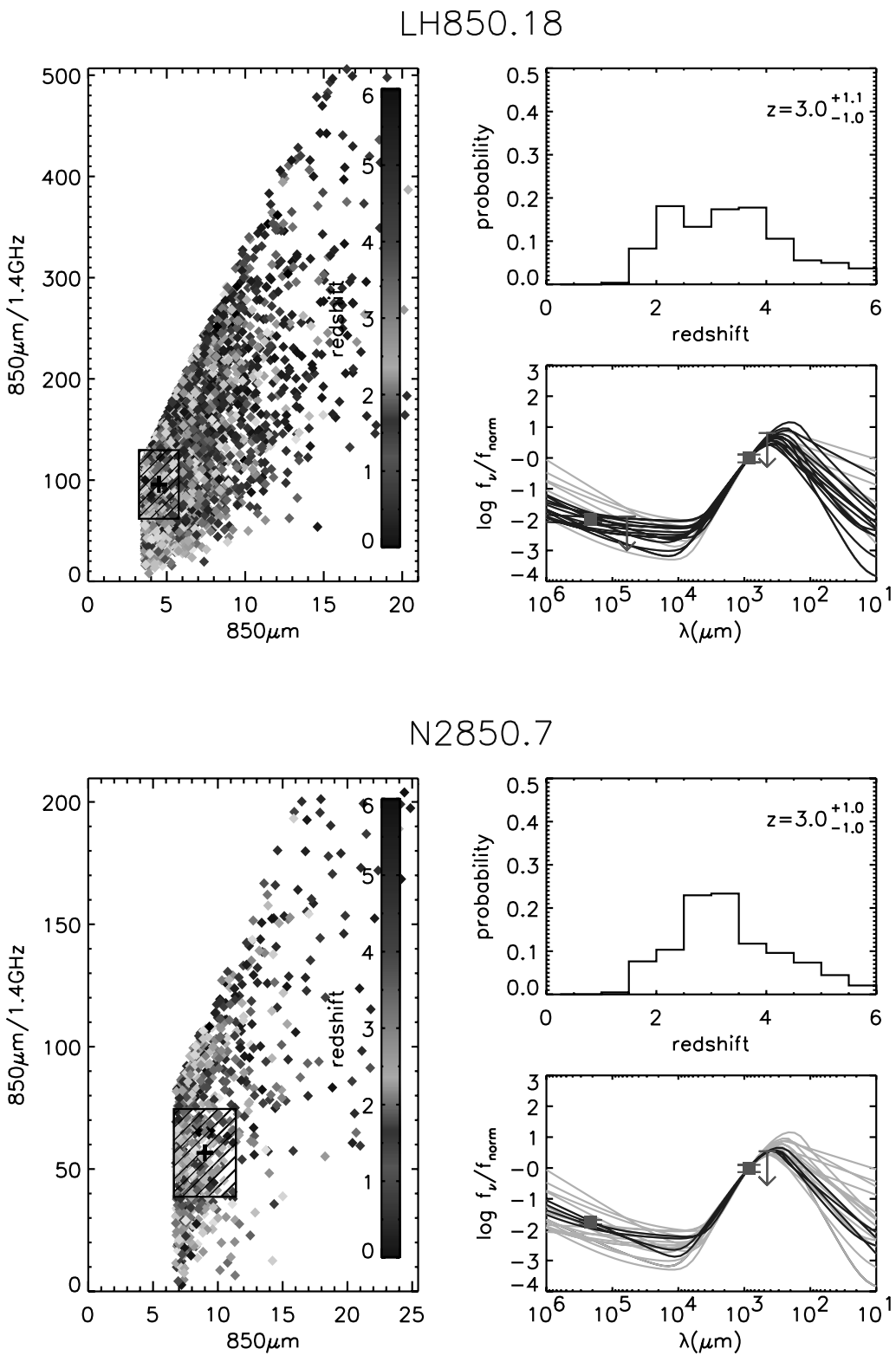

Figure A2 – *continued*

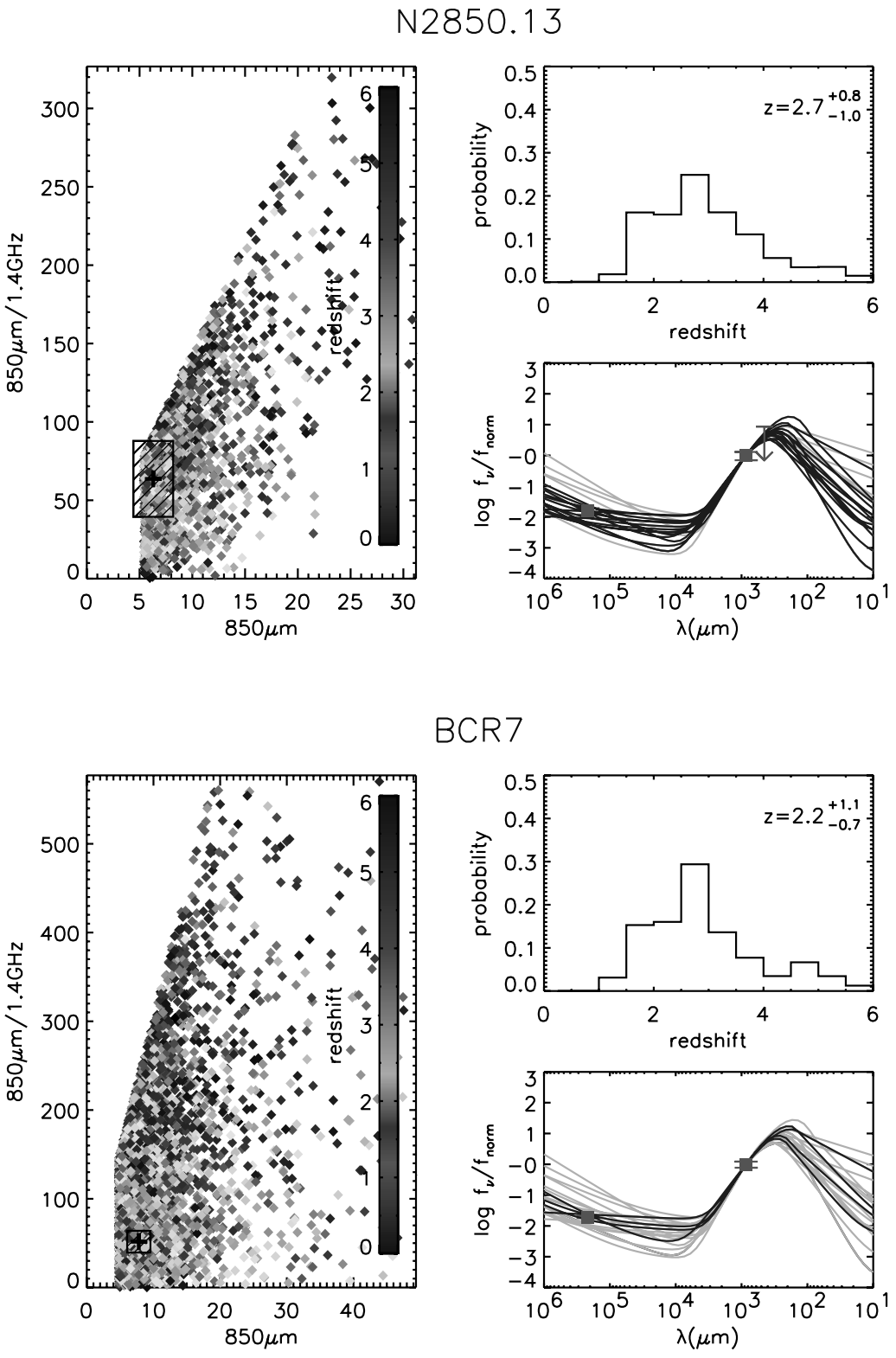

Figure A2 – *continued*

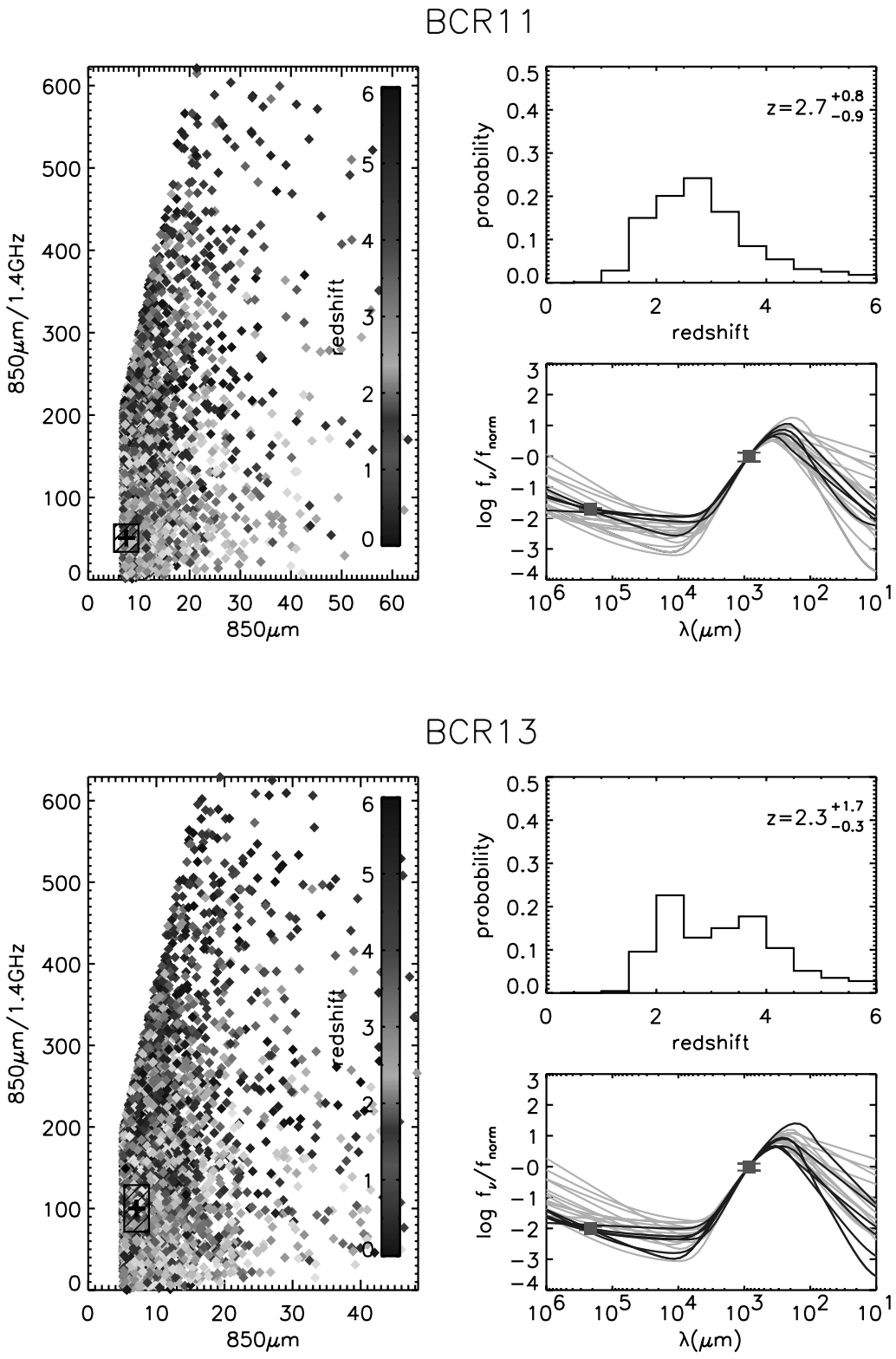

Figure A2 – *continued*

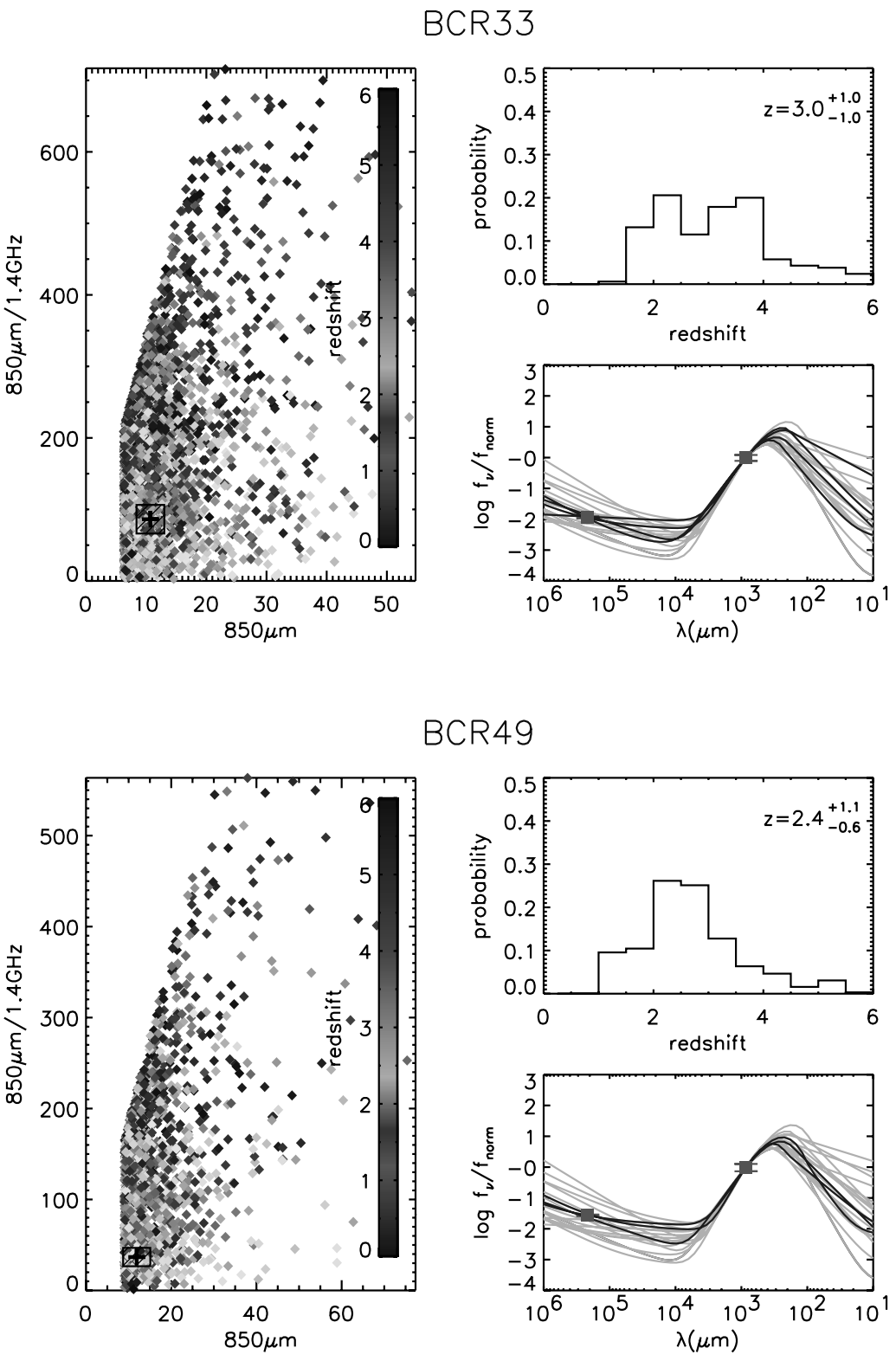

Figure A2 – *continued*

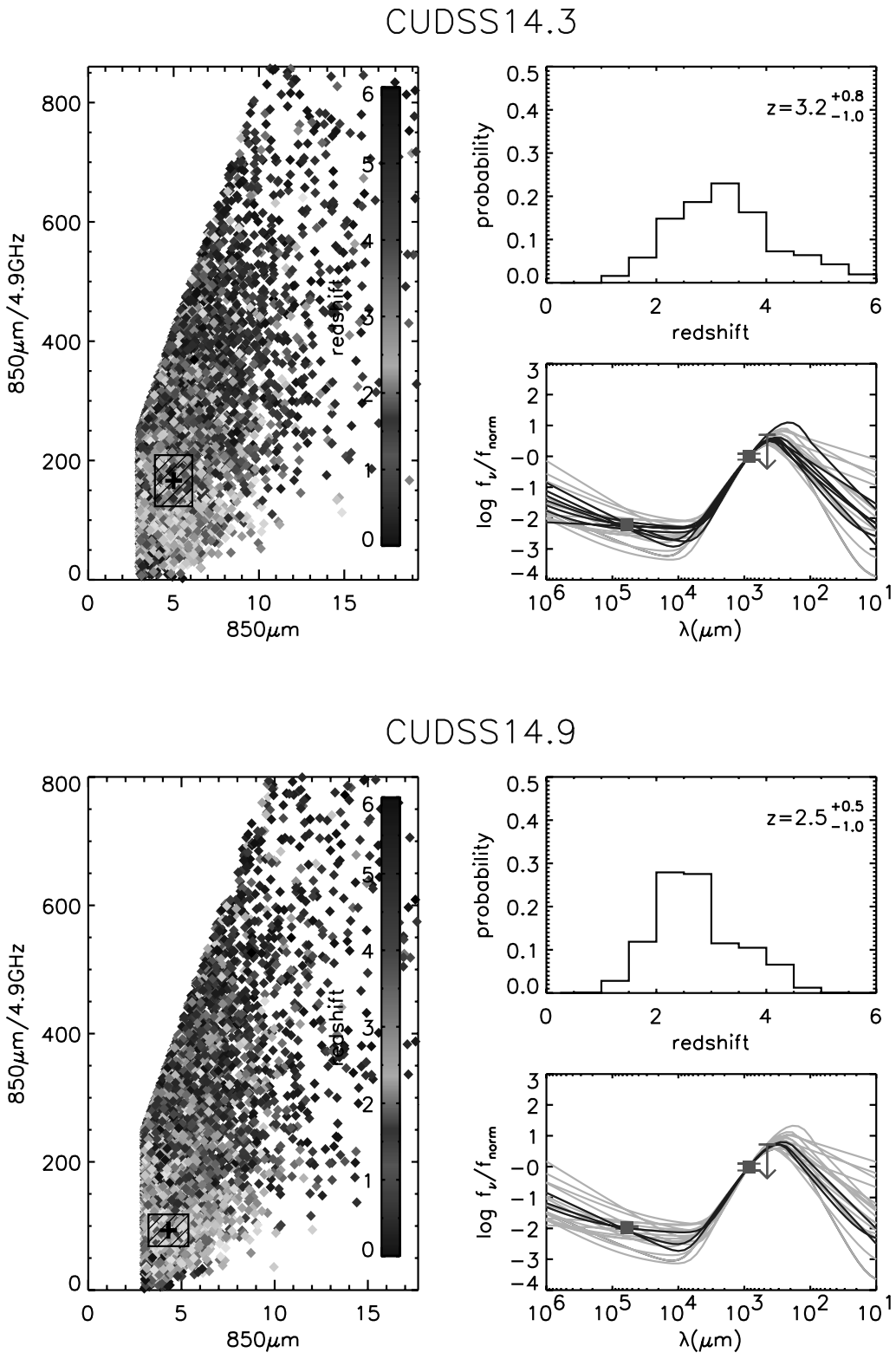

Figure A2 – *continued*

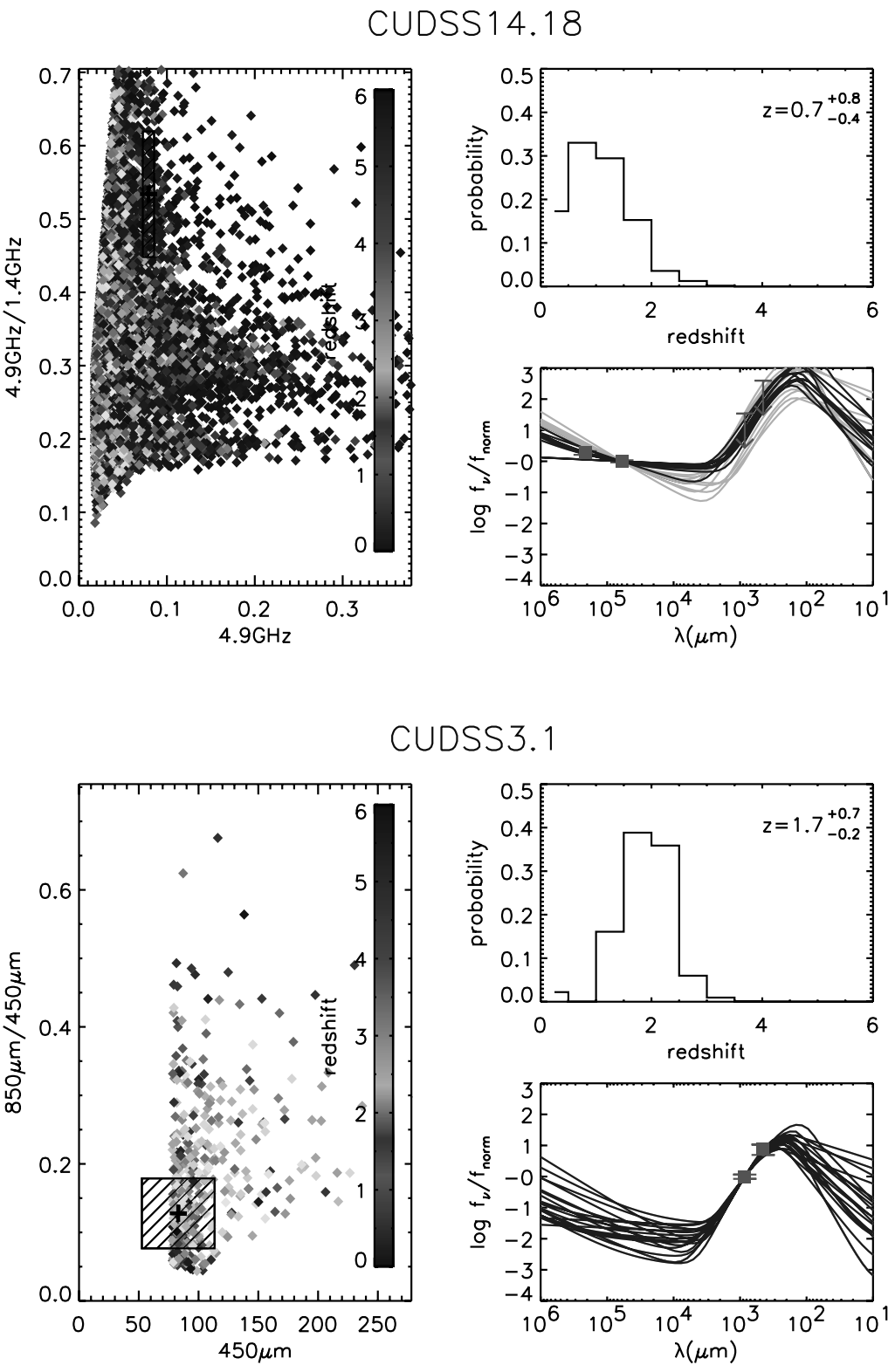

Figure A2 – *continued*

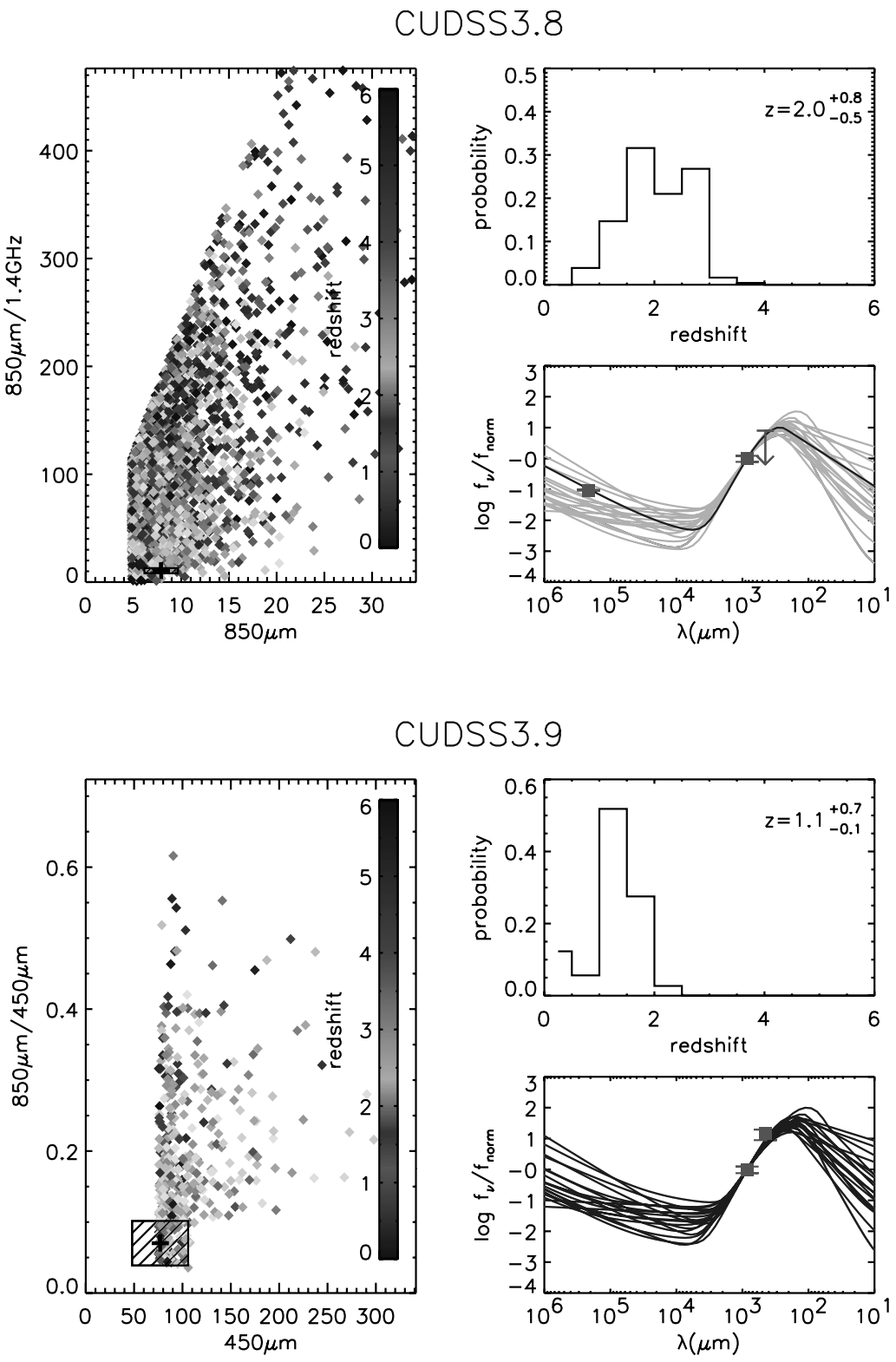

Figure A2 – *continued*

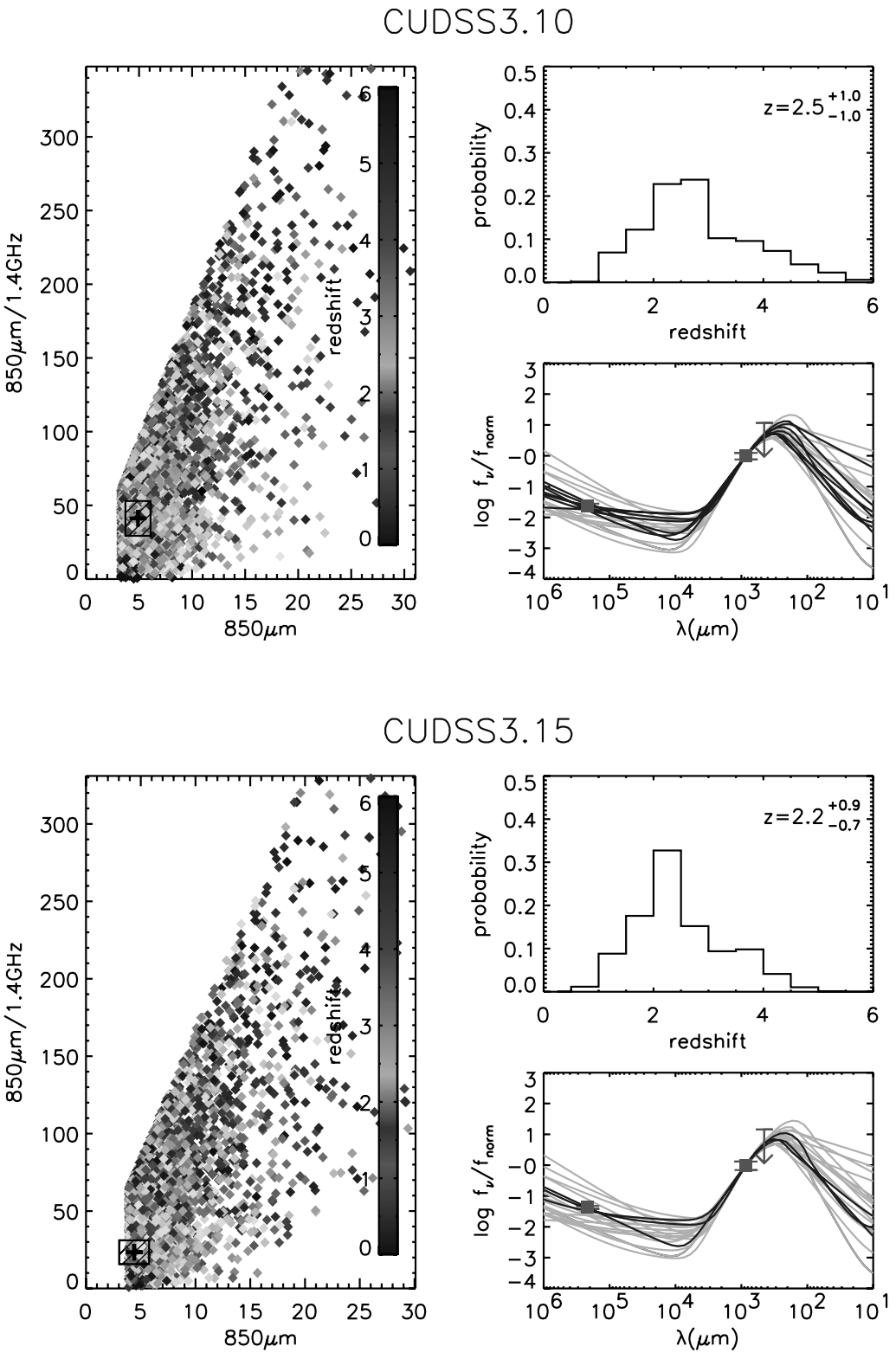

Figure A2 – *continued*

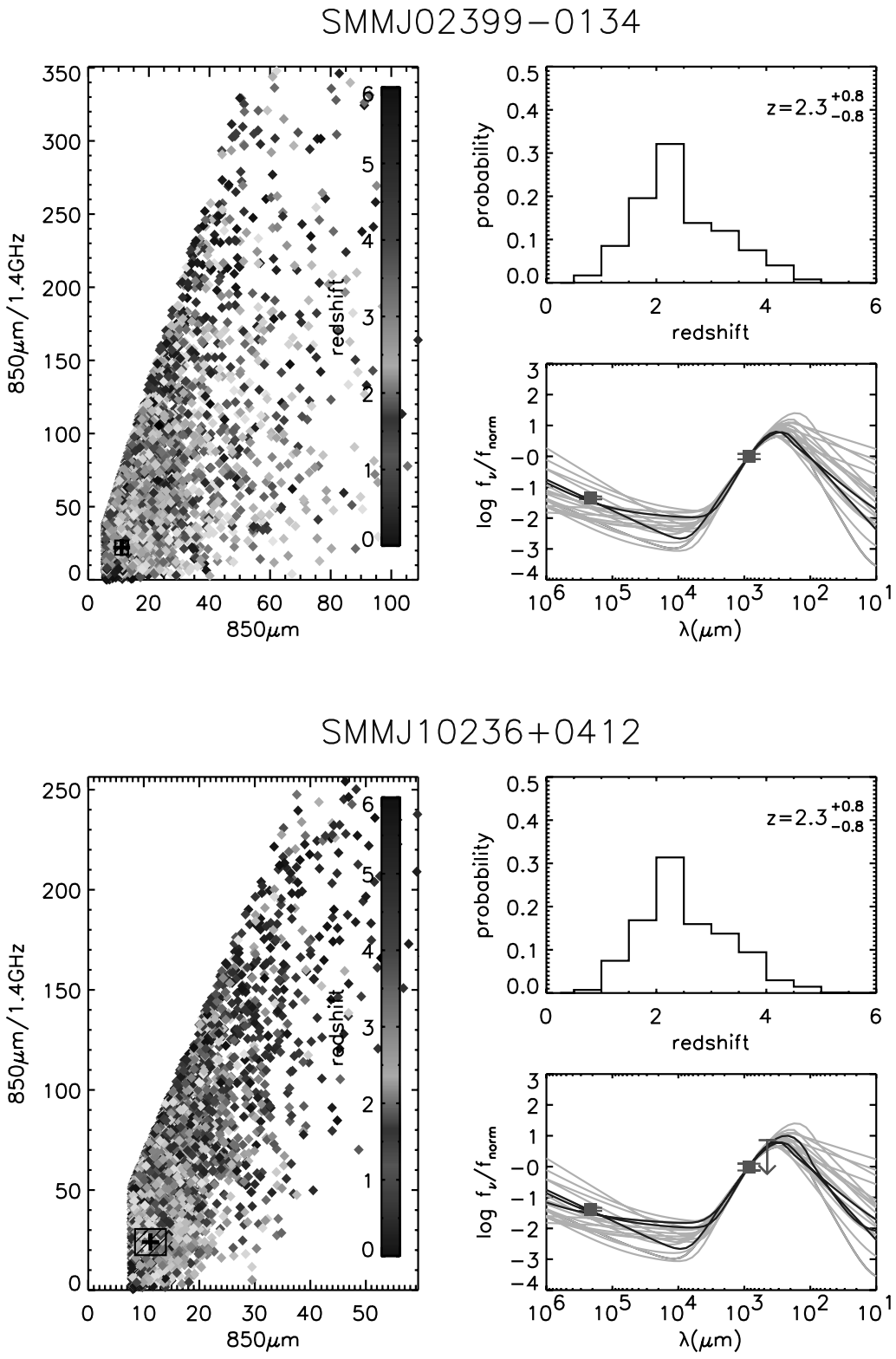

Figure A2 – *continued*

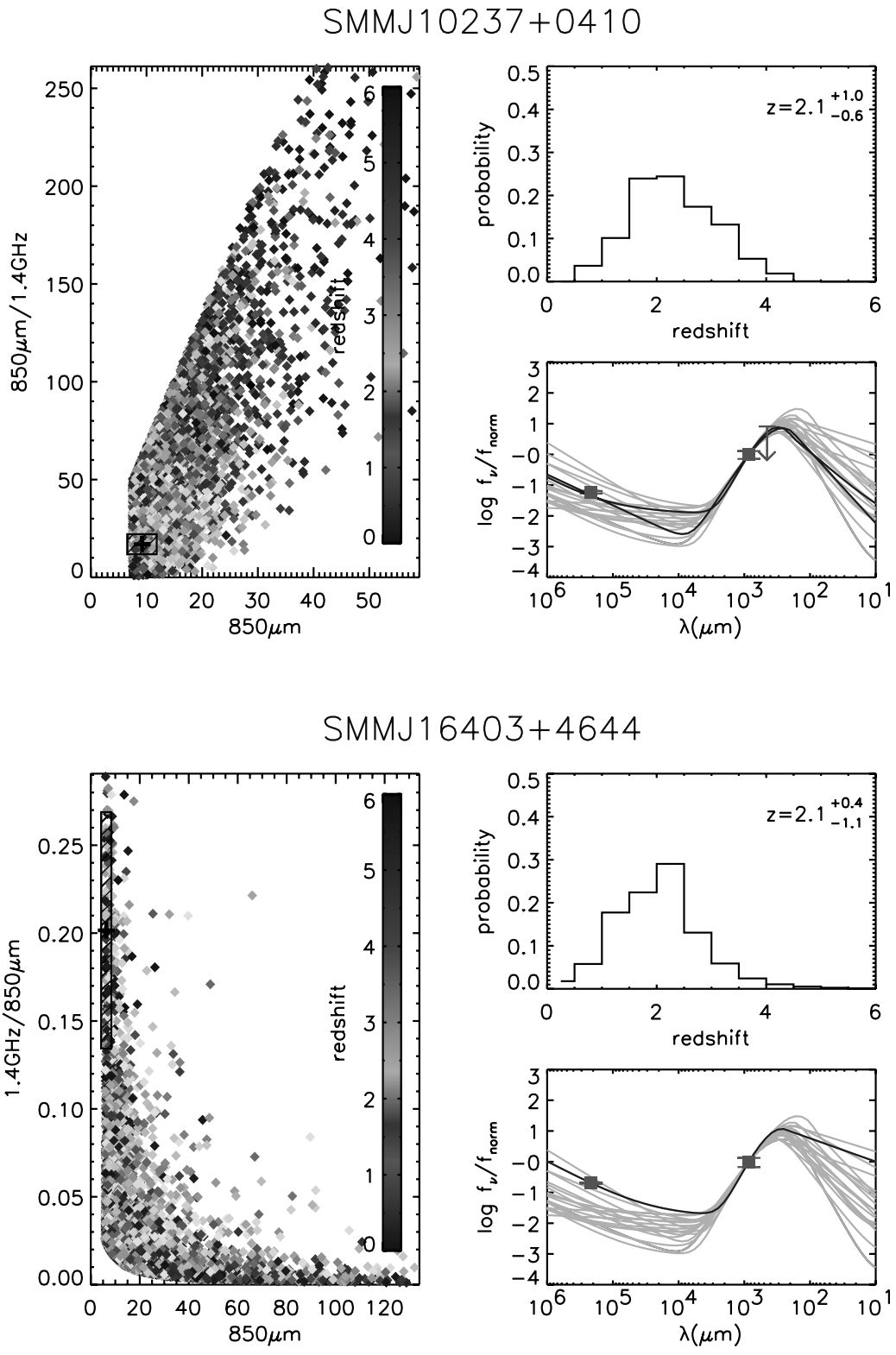

Figure A2 – *continued*

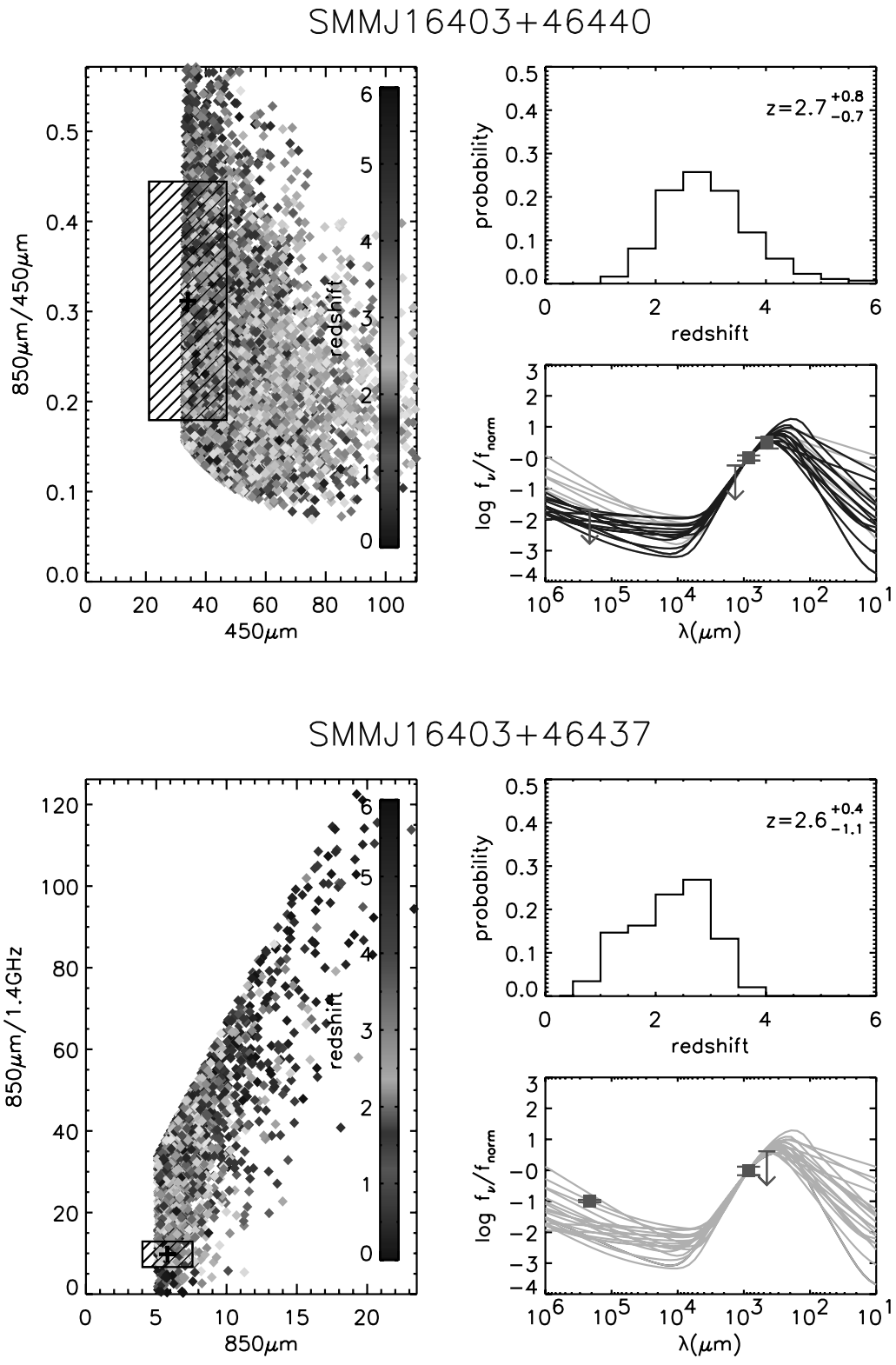

Figure A2 – *continued*

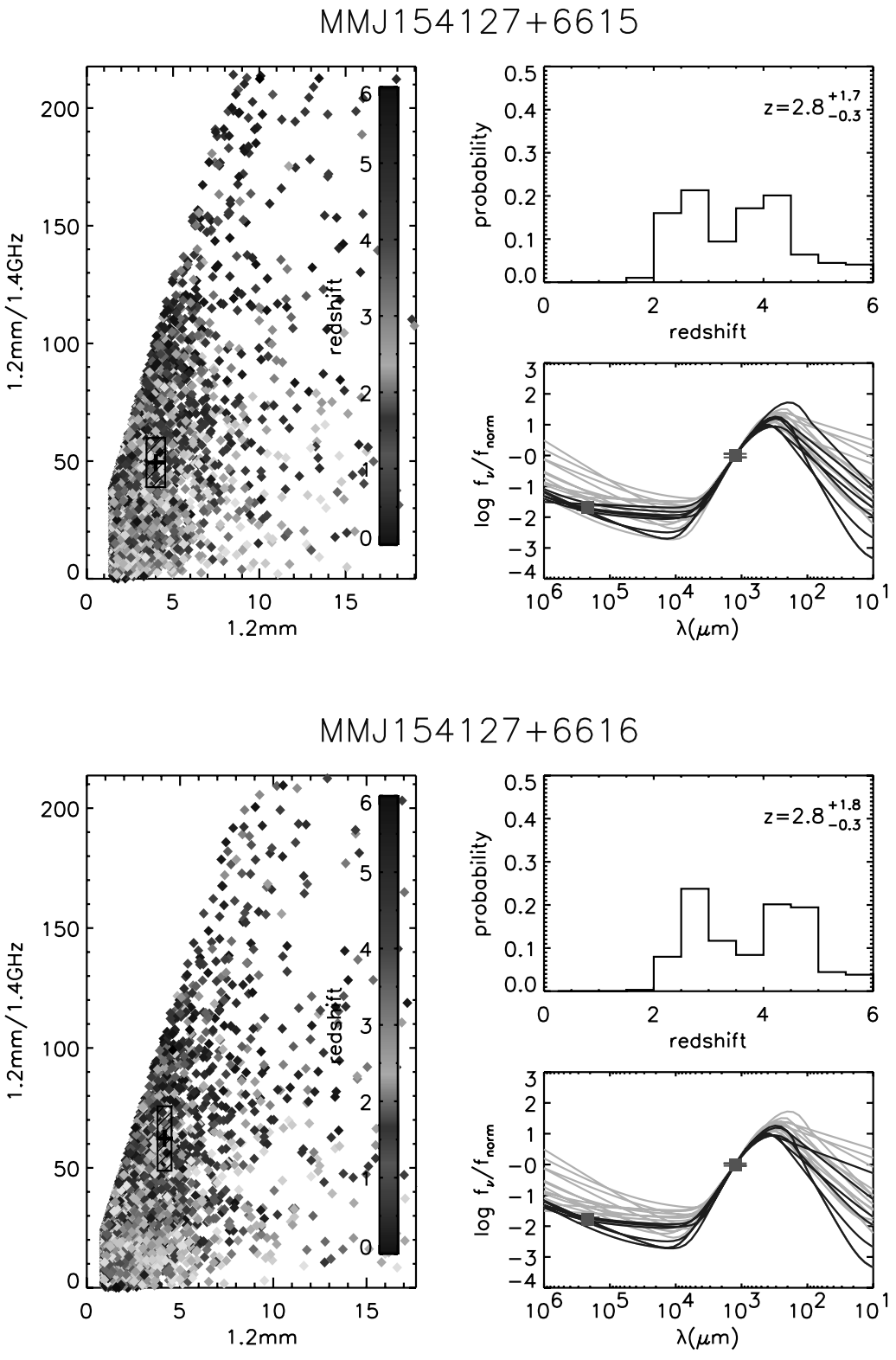

Figure A2 – *continued*

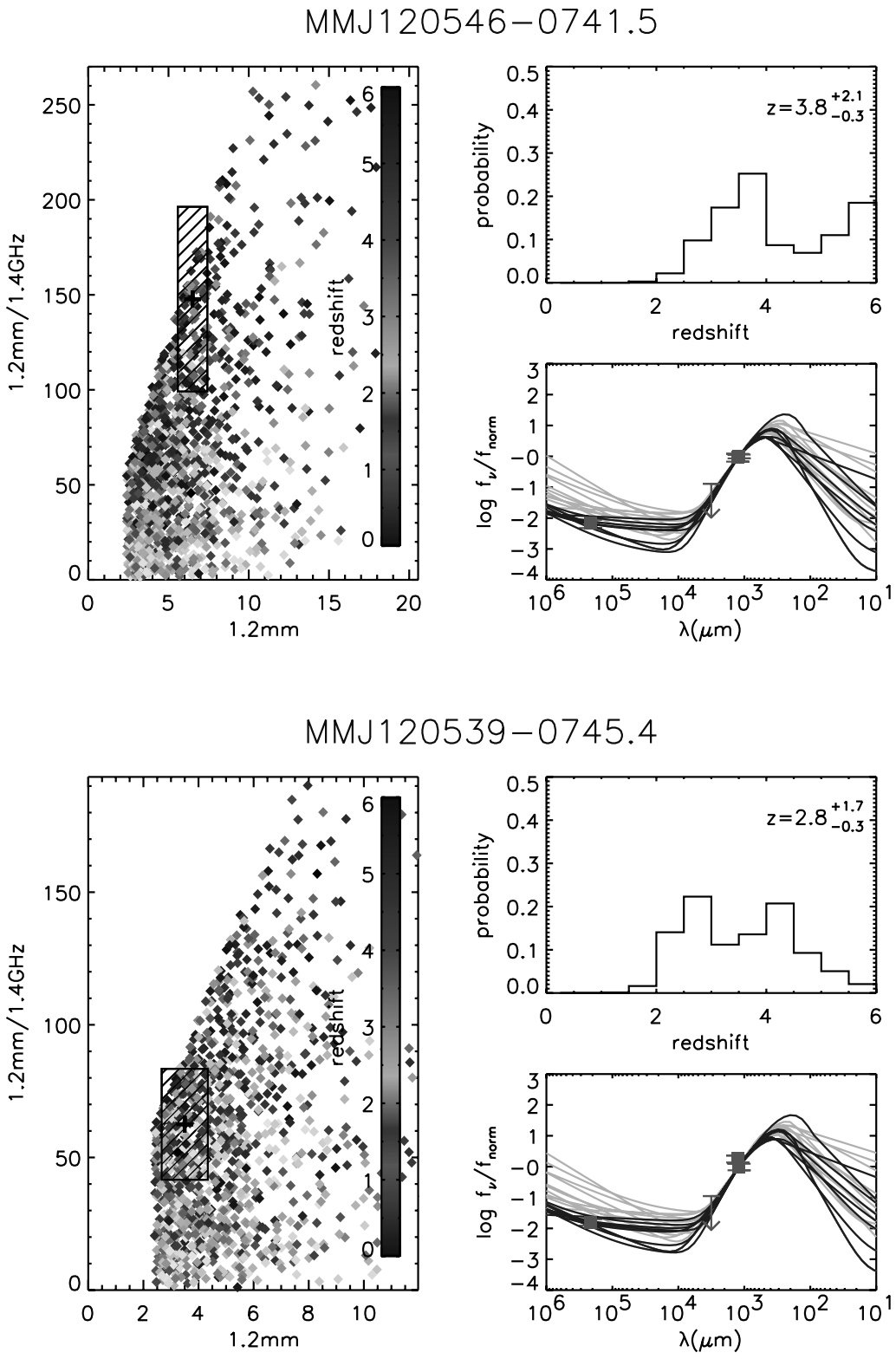

Figure A2 – *continued*

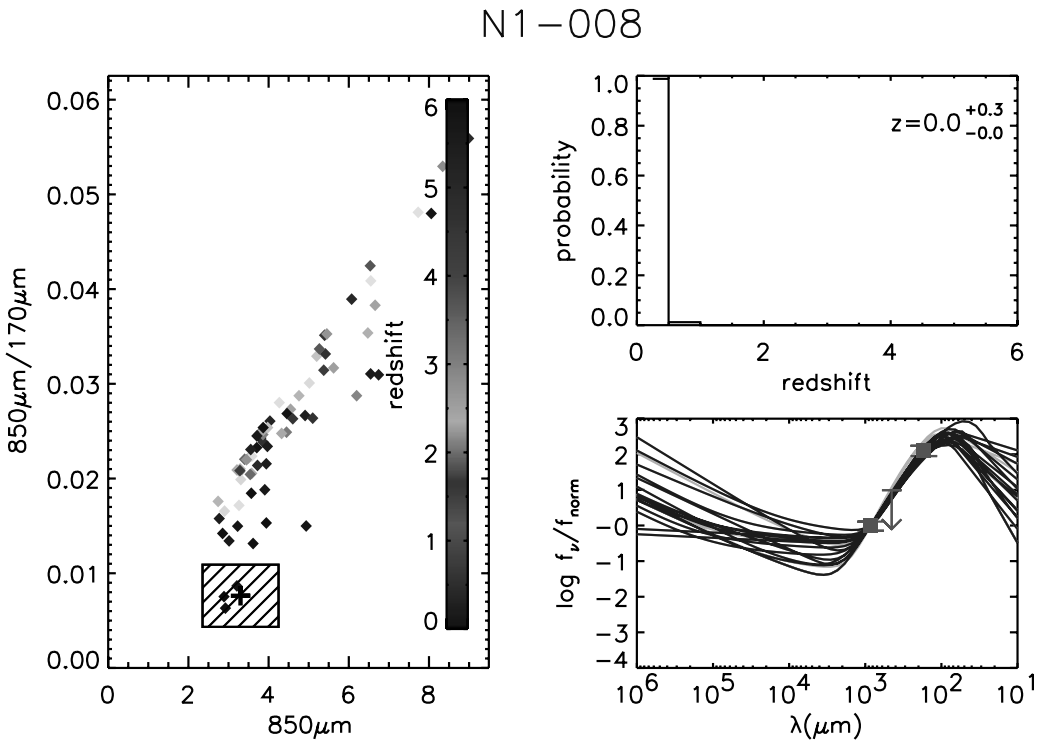

Figure A2 – *continued*

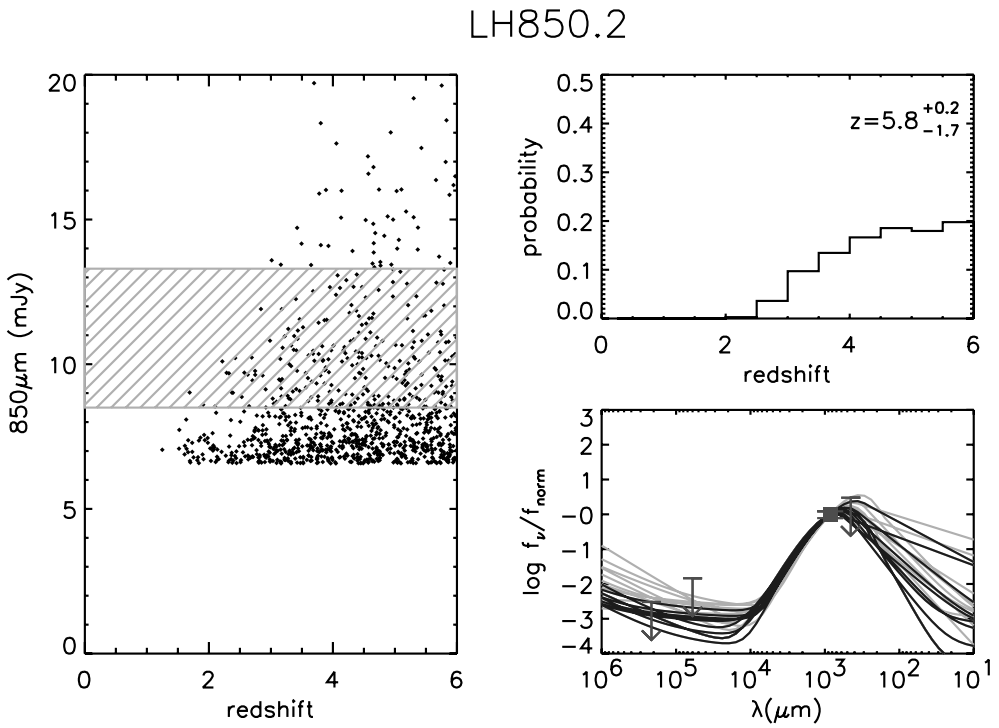

Figure A3. Selection of flux–redshift plots, redshift distributions and comparison of the template SEDs and observed data for sub-mm sources detected in one band at a $>3\sigma$ level. The slanted box in the flux–redshift plot marks the 1σ error box of the sub-mm galaxy. For the sake of clarity, just 1000 galaxies from the mock catalogue that fulfil the observational requirements of the sub-mm galaxies are represented (as dots). The rest of the elements in the panels are as in Fig. A1, except for the template SEDs, which are compatible with the colours of the sub-mm galaxies at a 3σ level, which are represented in dark grey here. This figure is available in colour in the online version of the journal on *Synergy*.

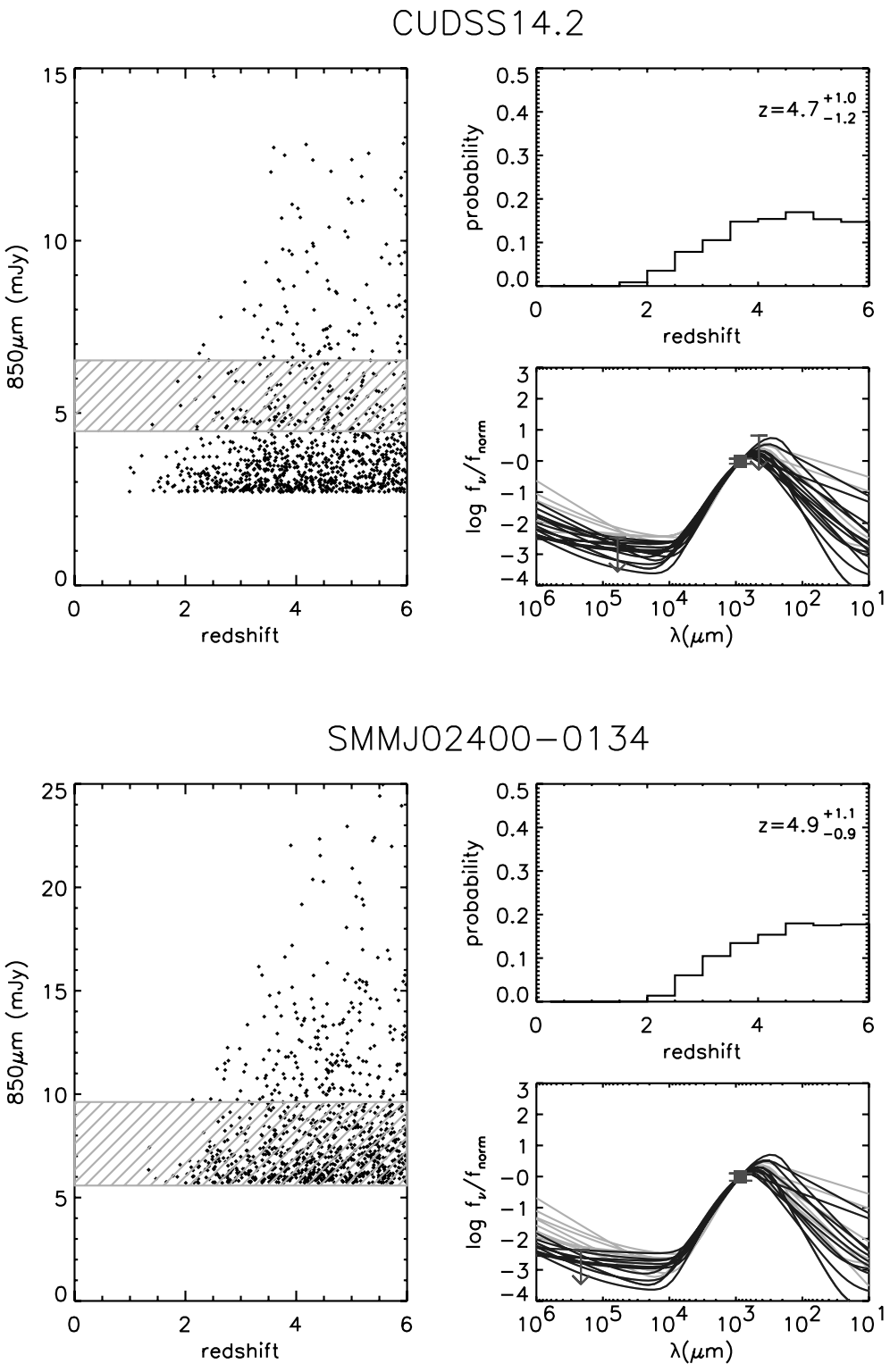

Figure A3 – *continued*

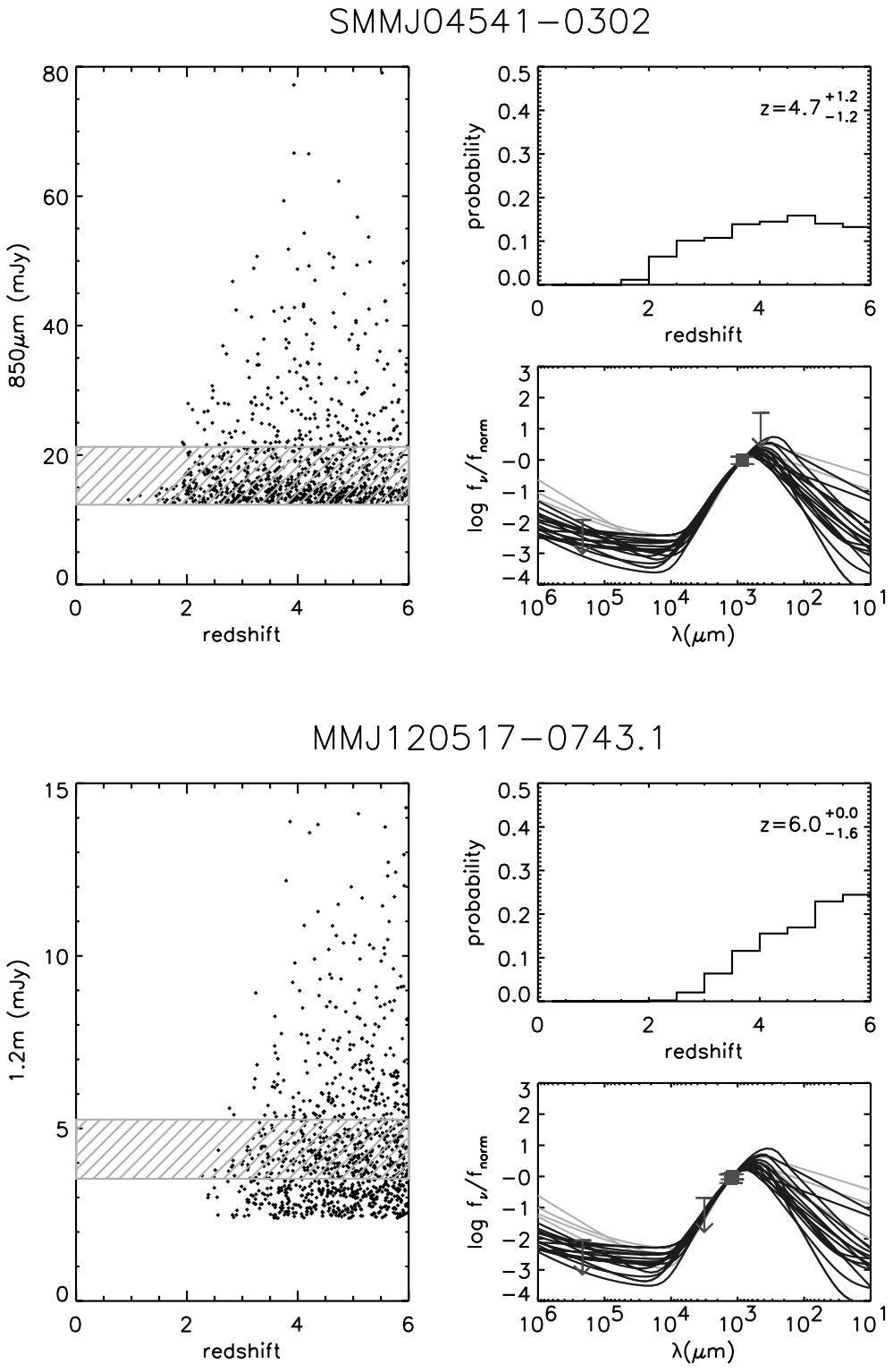

Figure A3 – *continued*

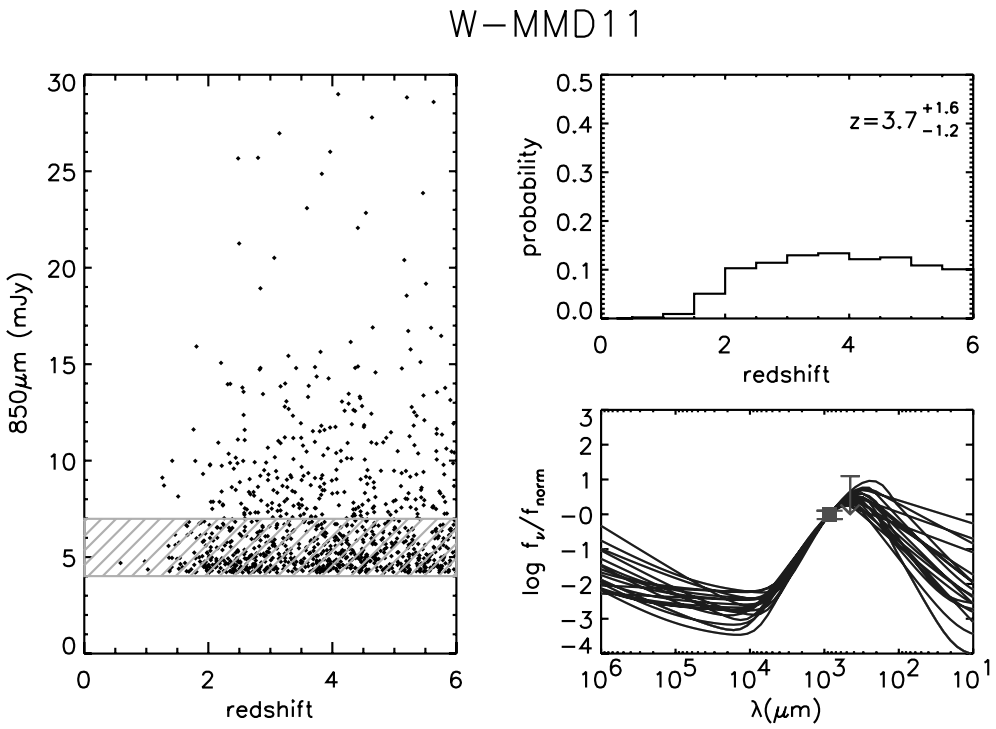

Figure A3 – *continued*

This paper has been typeset from a TEX/LATEX file prepared by the author.